UNIVERSITY OF OKLAHOMA

GRADUATE COLLEGE

NONLINEAR EQUALIZATION AND DIGITAL PRE-DISTORTION TECHNIQUES FOR FUTURE RADAR AND COMMUNICATIONS DIGITAL ARRAY SYSTEMS

A DISSERTATION

SUBMITTED TO THE GRADUATE FACULTY

in partial fulfillment of the requirements for the

Degree of

DOCTOR OF PHILOSOPHY

By

NICHOLAS LOUIS PECCARELLI

Norman, Oklahoma

2020

NONLINEAR EQUALIZATION AND DIGITAL PRE-DISTORTION TECHNIQUES FOR FUTURE RADAR AND COMMUNICATIONS DIGITAL ARRAY SYSTEMS

A DISSERTATION APPROVED FOR THE
SCHOOL OF ELECTRICAL AND COMPUTER ENGINEERING

BY THE COMMITTEE CONSISTING OF

Dr. Caleb Fulton, Chair

Dr. Nathan Goodman

Dr. Hjalti Sigmarsson

Dr. Jay McDaniel

Dr. Alexander Grigo

Dedicated to my grandfather, Louis Peccarelli, who taught me that knowledge is irreplaceable.

Acknowledgements

This work was supported by the Defense Advanced Research Projects Agency (DARPA) under grant no. D15A00090.

Table of Contents

List of Figures

Abbreviations

4G	fourth generation
5G	fifth generation
ACPR	adjacent channel power ratio
ADBF	adaptive digital beamforming
ADC	analog-to-digital converter
BB	baseband
BPF	bandpass filter
C-SWaP	cost, size, weight, and power
CMD	crossmodulation distortion
COTS	commercial off-the-shelf
CW	continuous wave
DAR	Digital Array Radar
DBF	digital beamforming
DCR	direct conversion receiver
DOF	degrees-of-freedom
DPD	digital pre-distortion
DR	dynamic range
DSP	digital signal processing
FAA	Federal Aviation Administration
FIR	finite impulse response

I/Q	inphase and quadrature
IC	integrated circuit
IF	intermdeiate frequency
IIP3	input third-order intercept
IM3	third-order intermodulation distortion
IMD	intermodulation distortion
IP3	third-order intercept
LFM	linear frequency modulation
LNA	low noise amplifier
LO	local oscillator
LS	least squares
LTE	Long-Term Evolution
LTI	linear and time-invariant
LUT	lookup table
MC	mutual coupling
MIMO	multiple-input-multiple-output
MP	memory polynomial
NF	noise figure
NLEQ	nonlinear equalization
NMSE	normalized mean-square error
OIP3	output third-order intercept

P1dB	1-dB compression point
PA	power amplifier
PAPR	peak-to-average power ratio
PVT	process-voltage-temperature variation
RCS	radar cross-section
RF	radio frequency
Rx	receiver
SFDR	suprious-free dynamic range
SINR	signal-to-interference-plus-noise Ratio
SNR	signal-to-noise ratio
SoI	signal-of-interest
THAAD	Theater High Altitude Area Defense
Tx	transmitter
UWB	ultra wideband
WiMAX	Worldwide Interoperability for Microwave Access
WLAN	wireless local-area-networks

Abstract

Modern radar (military, automotive, weather, etc.) and communication systems seek to leverage the spatio-spectral efficiency of phased arrays. Specifically, there is an increasingly large demand for fully-digital arrays, with each antenna element having its own transmitter and receiver. Further, in order to makes these systems realizable, low-cost, low-complexity solutions are required, often sacrificing the system's linearity. Lower linearity paired with the inherent lack of RF spacial filtering can make these highly digital systems vulnerable to high-power interferering signals– potentially introducing spectral regrowth and/or gain compression, distorting the signal-of-interest.

Digital linearization solutions such as Digital Pre-Distiortion (DPD) and Nonlinear Equalization (NLEQ) have been shown to effectively mitigate nonlinearities for transmitters and receivers, respectively. Further, DPD and NLEQ seek to extend the effective dynamic range of digital arrays, helping the systems reach their designed dynamic range improvement of $10\log_{10}(N)$ dB, where N is the number of transmitters/receivers. However, the performance of these solutions is ultimately determined by training model and waveform. Further, the nonlinear characteristics of a system can change with temperature, frequency, power, time, etc., requiring a robust calibration technique to maintain a high-level of nonlinear mitigation.

This dissertation reviews the different types of nonlinear models and the current NLEQ and DPD algorithms for digital array systems. Further, a generalized calibration waveform for both NLEQ and DPD is proposed, allowing a system to maximize its dynamic range over power and frequency. Additionally, an *in-situ* calibration method, leveraging the inherent mutual coupling in an array, is proposed as a solution to maintaining a high level of performance in a fielded digital array system over the system's lifetime. The combination of the proposed training waveform

and *in-situ* calibration technique prove to be very effective at adaptively creating a generalized solution to extending the dynamic range of future low-cost digital array systems.

1 Background, Motivation, and Previous Work

There continues to be a growing demand for highly digital phased array systems, which has produced a plethora of research. Specifically, there is a desire for low-cost, reconfigurable, multi-mission fully-digital phased array and multiple-input-multiple-output (MIMO) systems for radar and wireless communication [1]–[10]. This functionality is increasingly accompanied by the use of ultra wideband (UWB), tunable components, with each antenna element having its own transmit and receive channels allowing for easy scalability – based on the number of antenna elements. Due to each element requiring its own transciever, low-cost and low-complexity is required in order to create affordable systems [2]. Such systems offer advantages such as active electronic beamsteering, digital control over each element, and graceful degradation over the system's lifetime, etc. Further, the large number of required components leads to larger costs per element compared to standard single channel systems; on the other hand, since DR scales roughly linearly with array size – on the order of $10\log_{10}(N)$, where N is the number of transceivers – the power requirements (and, therefore, linearity) for each channel can be relaxed [8]. Digital arrays also suffer from nonlinearities – exacerbated by the use of low-cost, low-power components – inphase and quadrature (I/Q) imbalance at each channel, local oscillator (LO) synchronization issues as well as correlated LO phase noise, and phase and gain mismatches between channels. Furthermore, the correction and calibration of such issues and non-idealities has been studied [4], [11]–[14] – allowing realized systems to meet their theoretical performance gains.

The radar community has spent decades working to increase the digitization of radar systems [7]–[9], [15], through phased arrays, in order to quickly scan volumes – making use of electronic beamsteering, digital beamforming (DBF), and ultimatly adaptive digital beamforming (ADBF) – form multiple simultaneous beams, track

multiple targets, and have the ability to fullfil multiple missions. More recently, however, fourth generation (4G) Long-Term Evolution (LTE) wireless communications standards brought some of the first MIMO systems to the wireless communications community, with the fifth generation (5G) revolution further demanding highly-digital solutions. Additionally, MIMO systems have seen uses in other communications standards, such as Worldwide Interoperability for Microwave Access (WiMAX) [16], [17], and wireless local-area-networkss (WLANs) like IEEE 802.11n and IEEE 802.11ac [17]–[19].

Currently, the dream of low-cost, wideband, reconfigurable digital arrays is becoming a reality, and, thus, there is growing interest in the characterization and calibration of these systems, especially to be accomplished in real-time for fielded systems. This type of *in-situ* calibration method has been studied in [8], [12], [20]–[22], provides a method to continue to opperate the fielded systems at their maximum performance level throughout their lifetime. Additionally, many solutions for lowering the cost, size, weight, and power (C-SWaP) for digital array systems for both civilian and military radar, as well as wireless communication systems have been researched and proposed. Further, there has been a recent increase in the availability of higher frequency commercial off-the-shelf (COTS) RF components due to the continued growth in wireless communications and automotive radar. Making use of these low-cost COTS components has helped modern systems to align with C-SWaP, producing affordable digital array systems. One example of a COTS-based digital array was the Army Digital Array Radar (DAR) [1], which additionally provided one of the first published examples of mutual coupling *in-situ* calibration for a digital array. Additionally, to the author's knowledge, it was the first digital array to demonstrate the application of NLEQ (which will be discussed in detail throughout this dissertation) and spur decorrelation [4]. Lastly, partial filter-

ing for digital arrays comes digitally, after all signals have passed through the RF components, which, compared to analog arrays and subarray-digital arrays, makes digital arrays especially sensitive to interferers [7], [9], [23]. This lack of spatial filtering makes digital arrays more likely to be forced to operate in the nonlinear region due to large, unwanted signals.

On transmit, in general, as much power as possible is pushed through the system, forcing the front-end power amplifiers (PAs) to operate in their nonlinear region, or forcing inefficient backoff to remain linear. Operating PAs in their nonlinear region is highly power efficient since a lower bias voltage is needed to output a specified power-level compared to linear operation. However, operating in the nonlinear region can cause intermodulation distortion (IMD), crossmodulation distortion (CMD), harmonic distortion, and gain compression [23]–[25]. Further, low-cost RF active components tend to be even more nonlinear in nature [4]. Generally, the nonlinear characteristics of a component or system are defined by the IP3 and/or the P1dB, shown in Fig. 24a. Additionally, Padaki, Tandon, and Reed give a good overview of the differences between the different types of nonlinear distortion in [26]. In brief, nonlinear distortions can be described as:

1. IMD – when two or more signals combine to produce distortion at a new frequency, which is determined by the frequencies of the combined input signals.

2. CMD – is distortion in the form of gain and phase effects from one input frequency onto another input frequency.

3. Harmonic distortion – the introduction of higher order terms (harmonics), such as $2f, 3f, \ldots, nf$.

4. Gain compression – effects from the odd order terms that fall at their original

input frequency adding gain and phase effects that reduce the output power of a given signal.

Most research has been focused on eliminating IMD since this distortion causes adjacent-band spectral spreading and, with modern communication channels neighboring each other, the IMD can pollute adjacent channels [27]. Much development has been done to correct this spectral spreading on transmit through the use of DPD and on receive using NLEQ. These linearization techniques and a more indepth analysis on nonlinear systems is given in Chapter 2.

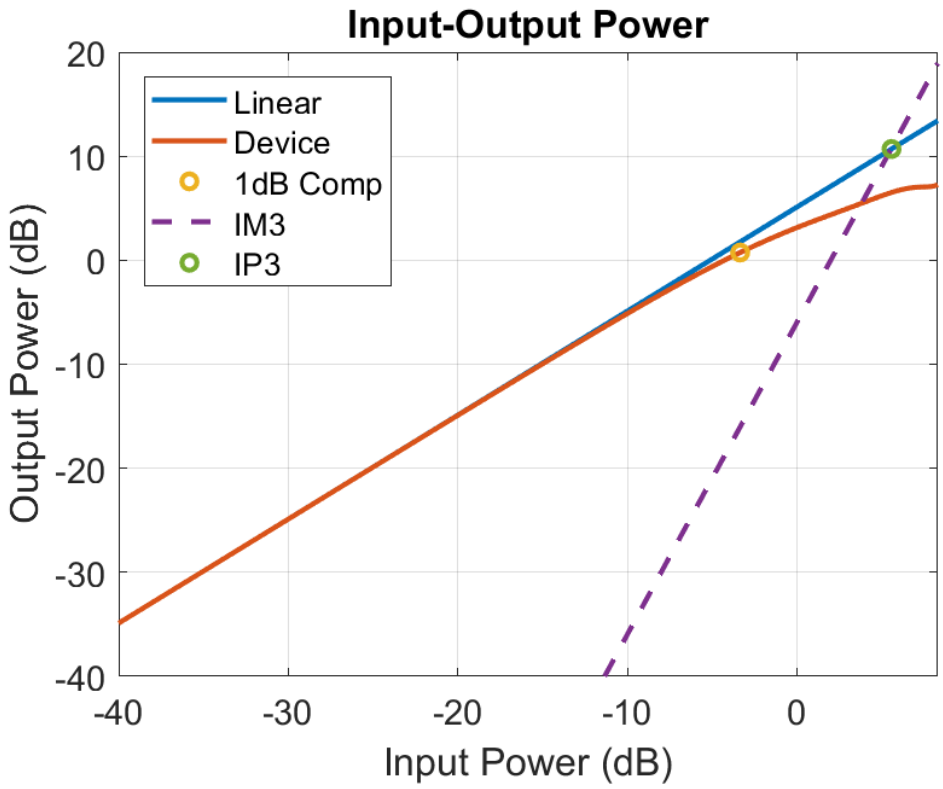

Figure 1: Input-output power plot of a generic nonlinear device, showing the IP3 and P1dB.

With a good understanding of nonlinear models from Chapter 2, Chapter 3 goes over digital array nonlinearities. Each component of a typical digital array channel is considered. Additionally, using the nonlinear models from the previous chapter,

the different ways to model and simulate these component and system nonlinearities is discussed. Further, the architecture of the transceiver itself and how that affects the system nonlinearities is discussed. Specifically, the direct-conversion transceiver, which eliminates the RF image rejection filter and intermediate frequency (IF) stages required by super-heterodyne transceivers, and has played a large role in lowering the cost, complexity, and size of modern communication and radar systems [1], [2], [4], [28]–[32] is focused on. In addition to the system nonlinearities, additional impairments such as I/Q imbalance, LO leakage, phase and gain mismatches, and mutual coupling [4], [29], [33]–[35] are reviewed. Additionally, a further digital architecture in direct sampling is briefly discussed. Lastly, array nonlinearities correlate during beamforming, limiting the $10\log_{10}(N)$ gain in DR [4], [8], [23]–[25], [36], [37]. Additionally, radar systems often operate in environments where a system's ability to correctly detect and track targets can affect people's lives – for example, automotive radar, Federal Aviation Administration (FAA) radar, military radar, and even weather radar. Therefore, these systems not only need to be properly calibrated, but they also need to be resilient to interferering signals, sometimes referred to as blockers. Chapter 3 goes over how the different types of nonlinear distortion affect a radar system's performance. Specifically, pulse-Doppler radars seek to *pull* the return signal out from the noise through coherent integration gain, however, an *incoherent* interferer can produce nonlinear distortion that affects the signal-of-interest (SoI) in the form of IMD, CMD, and gain compression. Further, Chapter 3 then focuses on decorrelation-based techniques to mitigate transceiver nonlinearities. Specifically these techniques can be broken down into decorrelation through LO differences and digital signal processing (DSP) techniques. The LO techniques can be used to mitigate even-order baseband (BB) and RF nonlinearities as well as BB and RF harmonics [4], [24], [25], [37], [38].

Additionally, the DSP technique is an array-level approach to NLEQ, which can also be extended to DPD, that was first discussed in [14] and then extended in [39].

Waveforms for NLEQ and DPD calibration and nonlinear system characterization are then discussed in Chapter 4, where a new calibration waveform is proposed. The goal of the proposed waveform is the efficiently calibrate the entire system's operational bandwidth and power in order to find one set of linearization coefficients to be used for any transmit/receive waveform. Essentially, the goal of digital array calibration, in general, is to reduce the required computational load during ADBF, or eliminate the need for the *adaptive* aspect completely. Thus, it is also essential to reduce the computational requirements of the calibration itself, allowing for opportunities for *in situ* calibration of fielded, operational systems. Lastly, information about a system's nonlinear characteristics can be realized from the use of different waveforms; for example, the system's frequency dependence [40], [41].

In general, all electronic systems require some level of calibration; low-cost digital arrays are no different and have many aspects that need to be calibrated, such as LO synchronization, I/Q imbalance, gain and phase offsets, and nonlinearities. Chapter 5 goes over a method for calibrating the NLEQ and DPD coefficients for a digital array, leveraging the system's inherent mutual coupling. This method was first proposed in [22] which calibrated an array with a memory-less nonlinearity and identical channel characteristics. Here this method is extended to calibrate a system with memory-nonlinearities and channel variations. Ultimately, this is an *in-situ* calibration technique to correct for a majority of digital array non-idealities. Finally, Chapter 6 summarizes the work and speaks to future concepts.

1.1 Digital Array Radar Systems

Phased arrays have been used for the most modern and sophisticated radars for the past several decades, however, arrays have historically only been used for military applications. More recently, however, arrays have been used for weather radar [42] and automotive radar as well. This is impart due to the decrease in cost, the increase in COTS components, as well as the continued progress in Moore's law. Further playing off of Moore's law, digital arrays have been well received by the radar community. Both fully-digital [43] as well as subarray-digital [44], [45] array radars have been developed, specifically during the past decade. However, there has been very little published work pertaining to the calibration and nonlinear correction of these systems.

Radar systems can suffer greatly from both transmit and receive nonlinearities, with both of these issues relating in some fashion to the radar range equation, given by

$$R_{max} = \left[\frac{P_t G A_e \sigma}{(4\pi)^2 S_{min}} \right]^{1/4} \tag{1}$$

where P_t is the transmit power, G is the gain of the antenna, A_e is the antenna efficiency, σ is the radar cross-section (RCS) of the target, S_{min} is the minimum detectable signal, and R_{max} is the furthest range that a target of a specific RCS can be to be detected by the system. Therefore, it is important to maximize the transmit power, often achieved by operating the PAs in the nonlinear region. Further, the receiver needs to be able to detect the smallest signal possible, which can be accomplished by increasing the amount of gain throughout the receive chain, as well as minimizing the noise figure (NF). One way to lower the NF is for the first component to have a large gain and a low NF itself, as described in Eq. (2), given

by

$$F_{sys} = F_1 + \frac{(F_2 - 1)}{G_1} + \frac{(F_3 - 1)}{G_1 G_2} + \dots . \tag{2}$$

This means that the first component in the receiver, after the antenna, would need to be a low noise amplifier (LNA). However, this prevents a bandpass filter (BPF) from being able to remove any spectral interferers, opening the LNA up to more spectrum and, thus, increasing the likelyhood of operating in the nonlinear region. A strong interferer can easily distort the SoI through IMD, CMD, and gain compression – this is especially true for pulse-Doppler radars, which rely on coherent integration to maximize the signal-to-noise ratio (SNR). Therefore, it is important to provide some level of protection against nonlinear components, which can be done through DPD for Tx and NLEQ for Rx. Additionally, it is necessary that digital array radar systems are correctly calibrated and are able to be quickly and easily re-calibrated in the field in order to accurately beamform, enabling the radar to determine the range, velocity, and direction of a target.

1.2 5G MIMO Systems

Massive MIMO for 5G wireless networks will make use of low-cost, low-power, low-complexity components in order to properly scale array sizes and provide a high density of base-stations. System-level DR increases linearly with the number of antenna elements, allowing for the use of lower-cost/power/complexity transceivers than are required for legacy systems [8]. The past decade has seen a great increase in the number of mobile, wireless devices, with data traffic increasing 24-fold from 2010 to 2015, and expected to increase by 500- to 1000-fold from 2010 to 2020 [46], [47]. Smart-devices, such as phones, watches, televisions, and multiple other in-home devices, have created a saturated in-door spectral environment, making up 70 percent of all data consumption [47]. Furthermore, the advent of the Internet-of-

Things (IoT), with an estimated 50 billion connected devices by 2020, will increase mobile data traffic to an expected 24 Exabytes per month [48]. Along with this large increase in the number of mobile devices has come a strong demand for increased data rates – due to the desire for high speed mobile internet, smart cars/homes, augmented reality (AR), virtual reality (VR), and IoT [48]. To satisfy this need, data rates are expected to achieve 10-50 Gbps for 5G, compared to the 100 Mbps that 4G provides [48].

The increase and diversity in Radio Access Technologies (RATs) has forced researchers to look for more efficient ways to use the limited available spectrum. Traditionally, the spectrum bands were allocated for specific services, leading to an inefficient use of the RF spectrum, but recent research has suggested a dynamic sharing of the spectrum based on spatio-temporal needs. To facilitate this idea, the US Federal Communications Commission (FCC) has recently made the 3550-3700 MHz band available, along with 600 MHz of the AWS-3 band [26], [49]. The Citizens Broadband Radio Service (CBRS) bands – 3550-3700 MHz – which were previously dedicated to Naval Radar (3550-3650 MHz) and Fixed Satellite Systems (3650-3700 MHz), recently made available for wireless broadband, have received much attention and research [50]–[54]. The authors of [53], [54] studied the coexistence of Naval Radar and mobile communication systems, further focusing on co-channel and adjacent channel interference. The authors in [51] further studied spectrum sharing in the 5 GHz Unlicensed National Information Infrastructure band, commonly used for WiFi. Additionally, [55] studied the effect of spatio-spectral interference in an unlicensed mmWave band, such as the 60 GHz band. Furthermore, one of the most popular proposed methods for better utilizing the spectrum is through spatial multiplexing.

Multiple-input-multiple-output (MIMO) systems offer a solution to the demands

of 5G mobile networks through the use of spatial multiplexing. MIMO systems are related to phased array technology, which has been used for military radar and researched for decades [7]–[9], [15]. MIMO consists of multiple antenna elements for both transmit and receive, improving throughput, capacity, and coverage [56]. MIMO has seen initial uses in some 4G Long-Term Evolution (LTE) standards, wireless local-area-networks (WLAN, IEEE 802.11n, IEEE 802.11ac) [17]–[19], Worldwide Interoperability for Microwave Access (WiMAX) [16], [17], and radar [57]. Massive MIMO, which consists of orders of magnitude more antennas than standard MIMO, will further increase network capacity, and spectral and energy efficiency [6], [9], [56], [58], [59].

Massive MIMO consists of hundreds of antennas, relying on spatial multiplexing to serve tens of users and increase spectral efficiency [6], [15]. In order to make massive MIMO systems affordable, the elements need to consist of low-cost, low-power, low-complexity components. Creating such systems is one of the major goals for 5G, due to the need for higher network densification and the socioeconomic consequences of expensive systems [6], [9], [47]. Higher network density is required for multiple reasons; higher frequencies – which offer larger bandwidths, and thus, higher data rates, such as millimeter-wave (mmWave) – suffer much more from indirect path loss and therefore have limited non-line-of-sight (NLOS) communication performance. Denser networks also help to reduce power consumption because each base station (BS) will have a shorter radius to cover before another BS takes over coverage. Power requirements can further be reduced in massive MIMO systems because equivalent isotropic radiated power (EIRP) increases by M^2 when the number of antenna elements is increased by M, further reducing both component and operational costs [9].

mmWave, which covers the frequencies of 30-300 GHz, provides a promising

solution for the high data rates and spatial flexibility demanded by 5G MIMO systems [55], [60]. The small wavelength of mmWave frequencies will allow MIMO antennas to effectively fit into mobile devices, such as smartphones and IoT sensors, allowing them to take advantage of larger bandwidths and spatial multiplexing. Furthermore, the misconception that higher frequencies suffer insurmountable propagation loss can be invalidated when arrays are used to compensate for loss of physical aperture area [15], [61]–[63]. Therefore, increased propagation loss for line-of-sight (LOS) communications at mmWave frequencies is readily compensated for through the use of multiple antennas. It is important to note that mmWave NLOS communications suffer greater degradation from blocking by obstacles (e.g. buildings, cars, and people) or attenuation from environmental factors (e.g. foliage, precipitation, etc.) relative to traditional "beachfront" frequencies below 6 GHz [61]–[64]. However, such degradation can be compensated for by the additional spatial diversity available at the higher frequencies for sufficiently dense networks [61]. Further, if networks are sufficiently dense, restricted NLOS communications can improve spectral efficiency by using spatial blocking/attenuation to enable spectral re-use by nearby cells. mmWave frequencies have seen initial uses for communication systems in IEEE 802.11ad, which makes use of the unlicensed 60 GHz band [59], [64], [65]. In addition to the 60 Ghz band, the 28-30 GHz, 38 GHz, and 73 GHz bands have also been heavily studied for mobile communications [46], [59]–[61], [64], [66]–[73]. Lastly, mmWave MIMO systems are physically very small, containing many components, and are thus constrained by the need for heat dissipation [69].

One of the most important benefits provided by massive MIMO is the reduction of spatial interference through the use of beamforming, allowing spectrum to be reused for simultaneous communication with multiple users [9]. Using narrow

beams can help to mitigate spatial interference, but on the other hand, it increases the risk of link failure [47] – especially in the case of moving users [64], [74]. Furthermore, narrow beams on transmit help add a physical layer of security, preventing eavesdroppers outside of the spatial-beam from detecting the transmission [58]. While narrow beamforming techniques on transmit help to mitigate interfering with other BSs and users, on receive some low-cost massive MIMO systems, like digital phased arrays, are particularly sensitive to interference due to some level of reduction in analog spatial filtering [7]–[9], [15], [75]. This will be exacerbated by the simultaneous operation of 5G small cells and legacy macro cells, leading to irregular cell shapes/sizes and producing inter-cell interference [46]. This is also of concern for WLANs operating in unlicensed bands – such as the industrial, scientific and medical (ISM) band, which are deployed with little to no coordination [46].

In a naively deployed, densely populated systems environment such as WLAN and the initial deployment of 5G BSs operating along with legacy cells, interferers will be a limiting factor of system capacity [9]. Strong, unmitigated interferers decrease the signal-to-interference-plus-noise Ratio (SINR), which, for wireless communication systems, decreases the throughput. Additionally, strong interferers can drive the receiver into compression, producing IMD, further distorting the SoI, or even saturating the analog-to-digital converter (ADC). Therefore, it is imperative to implement methods – both analog and digital – to mitigate spatial and spectral interferers along with their residual IMD. Further, transmitter nonlinearities, which are typically introduced by the PA, need to be mitigated to prevent the spectral pollution of adjacent channels [27]. Lastly, an *in-situ* calibration method will be required, especially for massive MIMO BSs, in order to maximize the attainable data-throughput enabled by 5G.

1.3 Digital Array Beamforming

Beamforming is the process of the frequency-dependent linear combination of the signals from each element of the array [8]. A good review of DBF and its trade spaces is given by Fulton in [8], which is briefly reviewed here. DBF of an array of M elements can be described as

$$Y_p(\omega) = \sum_{m=1}^{M} H_{m,p}(\omega) X_m(\omega) \tag{3}$$

where $Y_p(\omega)$ is the frequency-domain result of the pth beam, $H_{m,p}(\omega)$ is the frequency-domain DBF processing of the mth element and pth beam, and $X_m(\omega)$ is the Rx signal of the mth element. The received signal can be given by

$$X_m(\omega) = F_m(\omega, \theta, \phi) G_m(\omega) \tag{4}$$

where $G_m(\omega)$ is the frequency-dependent gain of the mth element, and $F_m(\omega, \theta, \phi)$ is the embedded element pattern of the mth element, which includes all mutual coupling and finite array effects, as well as the element's location on the array.

The DBF processing can be implemented in an finite impulse response (FIR) type form, given by

$$y_p[n] = \sum_{m=1}^{M} \sum_{k=0}^{K-1} a_{m,p}[k] x_m[n-k] \tag{5}$$

where $a_{m,p}[k]$ are the DBF weights for the pth beam for the mth element at time k, and $x_m[k]$ is the time-domain signal from element m. Estimation of the errors in F_m and G_m is required to accurately derive the weights $a_{m,p}[k]$, while ADBF can be used to remove any residual errors – however, this requires an increase in computational expenses. Further, the G_m change with temperature, frequency, and

power (nonlinearities) and require calibration to reduce the number of degrees-of-freedom (DOF) in ADBF.

Fully-digital arrays offer the highest DOF, down to the element level, for ADBF processing. However, this can become extremely computationally expensive as arrays increase in size, therefore subarray-based processing is discussed as a solution in [8]. Further, it was shown that with accurate array calibration, the requirements of ADBF can be greatly reduced and even eliminated [8].

1.4 Digital Array Calibration

In general, arrays, both digital and analog, need to be calibrated; specifically, it is required that the amplitude and phase of each element is performing properly to ensure that the desired beam pattern is established [12], [13]. Further, even more important for small, finite arrays, the mutual coupling between elements can lead to pattern and/or frequency variations in each element [12]. In general, two types of calibration exist: "external calibration," typically performed in a spectrum-quiet environment, such as an anechoic chamber, before the system is fielded, and "internal calibration," which can be used to update the calibration of the fielded system [12]. Low-cost digital arrays make use of low-cost, low-complexity components, which are typically nonlinear in nature [4], [14], [76] – this characteristic often being defined by the IP3 and/or the P1dB – have been a topic of much interest in the recent decade. Initially, the issues of linearity were focused on the transmitter, specifically the PA, which is typically the most power hungry component in the system. Therefore, reducing the cost and power-consumption of the Tx PAs, allowing them to operate in the more efficient nonlinear region, is a seemingly straightforward way to meet the goals defined by C-SWaP. However, operating PAs in their nonlinear region has its consequences, such as the addition of memory effects (causing equal-

ization issues), compression of the higher power parts of the transmitted waveform, and spectral regrowth. Spectral regrowth, though undesired for radar, is a topic of much concern for communication systems – spectral regrowth pollutes adjacent bands, effecting nearby (in spectrum) users, often measured by the adjacent channel power ratio (ACPR) [77]. Furthermore, in recent years low-cost COTS components have also been used for receivers – lowering the linearity requirements, further exacerbating the sensitivity of digital arrays to interferers. On a side note, digital arrays are more sensitive to spatial interferers than analog (or subarray-digital) arrays due to their lack of spatial selectivity in the RF front-end and the typically wide-open embedded element pattern design for array antenna elements [7]. In order to mitigate these issues caused by nonlinear components many linearization techniques have been studied.

Digital pre-distortion (DPD) and nonlinear equalization (NLEQ) have both received a large amount of attention and research, the latter more recently, however. DPD and NLEQ have both been used to extend the spur-free dynamic range (SFDR) of systemss, mitigating intermodulation distortion (IMD) products and removing high-power signal compression. In general, DPD and NLEQ techniques have focused on single channel calibration and correction, while more recently some array system-level approaches have been investigated. Additionally, as with array calibration, there exist two types of DPD/NLEQ calibrations, also considered "external calibration," and "internal calibration." External calibration, as with array calibration, is completed prior to the device being fielded, often making use of look-up-tables (LUTs) to be used for different frequency and power combinations. Further, internal calibration can be implemented *in situ*, often with added system complexity, making use of loop-back receivers for DPD and lower DR reference receivers for NLEQ. This added complexity, however, goes against the goals of C-SWaP and

the desire to create systems of low-cost and low-complexity; therefore, in this paper we propose a mutual coupling-based calibration method for both DPD and NELQ in a digital array. Additionally, the characteristics of a nonlinear system can change with power, frequency, and temperature [12], [14], [77]–[81], further justifying a need for an *in situ* calibrtaion method.

The remainder of this dissertation lays out some of the inherent nonidealities in digital array systems and then goes over current methods for mitigating these distortions. Further, new calibration techniques are proposed for training the NLEQ and DPD algorithms for mitigating the system nonlinearities of digital arrays. However, before these linearization solutions can be discussed, nonlinearities, in general, are reviewed and discussed in the next Chapter.

2 Nonlinear Models and Linearization Techniques

A nonlinear system, in the most general sense, is a system that is *not* linear (i.e. it cannot be accuratly described by the elementary $y = mx + b$) – that is, a system that does not follow the superposition principle [82], [83]. The simplest way to describe a nonlinear system is through expansion of the elementary linear system, often referred to as a power series (or Taylor series) [84], and is given by

$$y(t) = \sum_{n=0}^{\infty} c_n x^n(t). \tag{6}$$

In most systems, the linear term dominates the input-output relationship and, therefore, engineers typically model the system as LTI. However, some components function through their inherent nonlinearity – mixers, frequency multipliers, etc. Further, as we continue to push toward smaller form factor, lower cost, and increasingly wider bandwidth systems, engineers need to begin to consider the nonlinearities of all components and find low cost solutions, such as NLEQ and DPD, to mitigate the added distortions. This Chapter will first review the most common ways to model nonlinear systems, then will go over the types of nonlinear distortions that occur in RF systems, and finally will present ways to mitigate system nonlinearities. Additionally, in this Dissertation when referring to nonlinear systems, it is assumed that they are nonlinear systems with memory unless otherwise specified.

2.1 Nonlinear Models

In general, nonlinear systems can be broken up into two types: weakly-nonlinear, and strongly-nonlinear; a simple example of these is shown in Fig. 2. Weather a system is weakly or strongly nonlinear is partially subjective, but, generally, the

difference lies in the sharpness of the *knee* or bend in the transition from the linear to nonlinear regions of the power curve. Most active RF components can be described as both weakly and strongly nonlinear depending on how far into the nonlinear region the component is being operated. However, some components, such as an analog-to-digital converter (ADC) or limiter are best described as strongly nonlinear since a sharp cut-off in the output power exists. Ultimately, this paper focuses on weakly nonlinear systems (i.e. we assume that the components limiting the linearity of an RF system are weakly linear and enter compression much before the strongly nonlinear components, such as the ADC). Additionally, two generalized bandwidth cases are considered: narrow band and wideband. Narrow band will, in general, refer to a case where there is a generally flat response in the frequency response of the system; that is, there is little to no frequency dependence or memory effects. Wideband, on the other hand, will be the most generalized case, where frequency dependence has an effect – in some cases, a great effect – and needs to be taken into account.

The proceeding subsections will go over different nonlinear models, not nececearily in any order of complexity, but in more of a derivation/historical order. The Taylor series, Eq. (6), was already metioned and is the simplest way to represent a nonlinear system with a polynomial. The remainder of the models in this section will all include memory, also referred to as frequency dependence. This, of course, adds to the complexity of the models, but also helps them to better model real systems, especially in the wideband sense.

2.1.1 Volterra Series

The Volterra series, (11), is a general expression of nonlinear systems, which was the subject of much of the early work on nonlinear systems. Initially, in order to

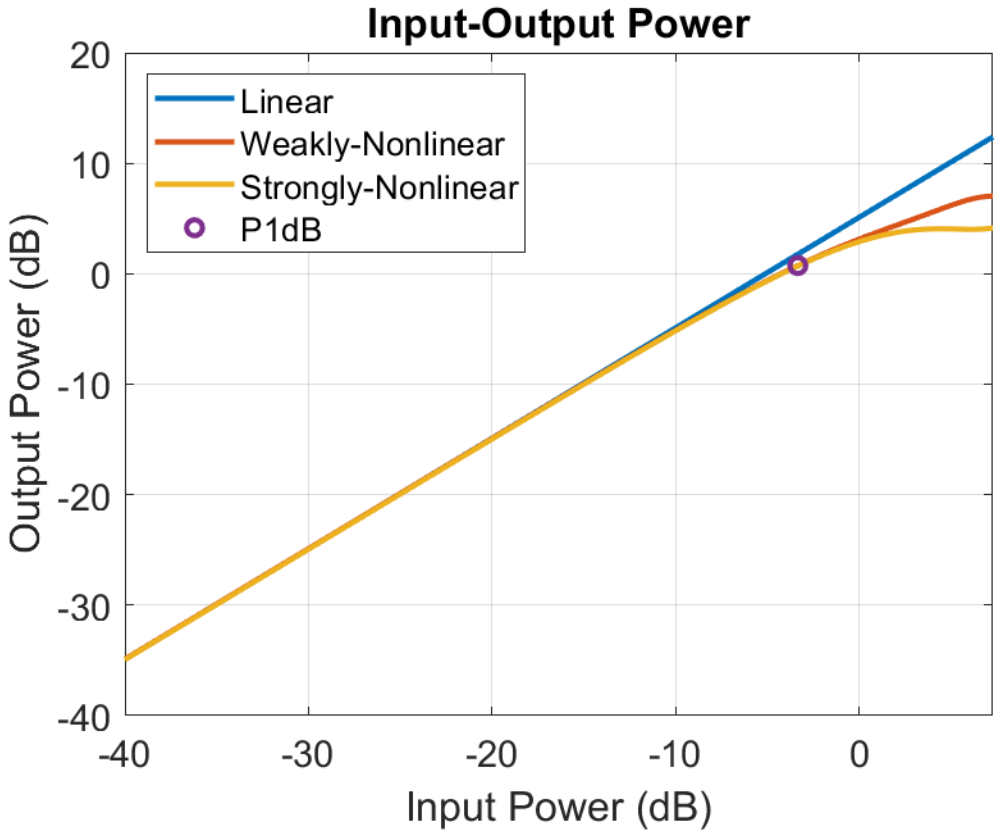

Figure 2: The input-power vs output-power plot, comparing a linear system, a weakly-nonlinear system, and a strongly-nonlinear system.

model a system, restrictions such as the input being required to be Gaussian white noise, and the measurement of only the first two kernels were applied [83]. Many of these methods were extended in the 1940s to 1960s at MIT by Wiener, Lee, Bose, Schetzen, and others, including the development of the Wiener series and the Lee-Schetzen method [83]. Due to the complexity and large size of the Volterra series, block-structure models were developed, including the Hammerstein, Wiener, and Wiener-Hammerstein models – these all being special cases of the Volterra series.

The most generalized way to represent a nonlinear system with memory using a polynomial is the Volterra series [85]–[88]. The Volterra series can be seen as an extension of a Taylor series, which is given by (6). The Volterra series [88]–[90] is

simply the k-dimensional convolution and can be represented as

$$\begin{aligned} y(t) = h_0 &+ \int_{-\infty}^{\infty} h_1(\tau_1)x(t-\tau_1)d\tau_1 \\ &+ \int_{-\infty}^{\infty}\int_{-\infty}^{\infty} h_2(\tau_1,\tau_2)x(t-\tau_1)x(t-\tau_2)d\tau_1 d\tau_2 \\ &+ \int_{-\infty}^{\infty}\int_{-\infty}^{\infty}\int_{-\infty}^{\infty} h_3(\tau_1,\tau_2,\tau_3)x(t-\tau_1)x(t-\tau_2)x(t-\tau_3)d\tau_1 d\tau_2 d\tau_3 \\ &+ \cdots \end{aligned} \tag{7}$$

which can be expressed more compactly as

$$y(t) = h_0 + H_1[x(t)] + H_2[x(t)] + \cdots + H_n[x(t)] + \cdots \tag{8}$$

where

$$H_n[x(t)] = \int_{-\infty}^{\infty} \cdots \int_{-\infty}^{\infty} h_n(\tau_1,\ldots,\tau_n)x(t-\tau_1)\cdots x(t-\tau_n)d\tau_1\cdots d\tau_n \tag{9}$$

Taking a look at this convolution in the discrete domain [88], [90], the Volterra series is given by

$$y(n) = \sum_{k=1}^{K} y_k(n) \tag{10}$$

where

$$y_k(n) = \sum_{m_1=0}^{M-1} \cdots \sum_{m_k=0}^{M-1} h_k(m_1,\ldots,m_k)\prod_{l=1}^{k} x(n-m_l) \tag{11}$$

or, simply

$$
\begin{aligned}
y(n) = & \sum_{m=0}^{M-1} h_1(m)x(n-m) \\
& + \sum_{m_1=0}^{M-1}\sum_{m_2=0}^{M-1} h_2(m_1,m_2)x(n-m_1)x(n-m_2) \\
& + \sum_{m_1=0}^{M-1}\sum_{m_2=0}^{M-1}\sum_{m_3=0}^{M-1} h_3(m_1,m_2,m_3)x(n-m_1)x(n-m_2)x(n-m_3) + \cdots
\end{aligned}
\tag{12}
$$

with h_k being referred to as the k^{th} Volterra kernel. The Volterra series model is effective for modeling weakly-nonlinear systems with memory – systems that are not driven too far into compression, (i.e. ADC saturation is a strongly-nonlinear system)[86], [91]. This is due to the Volterra series needing to expand to have an extremely large number of parameters to model systems with strong nonlinearities and long memory effects, making it inefficient to implement [86], [91]. In other words, a weakly nonlinear system can be well described by only the first few Volterra kernels [89], [90]. Typically, the Volterra series has been limited to third or fifth order models, which can realistically only model extremely weak nonlinearities [85]. Due to the large number of parameters that can make up a Volterra series and its usefulness at modeling nonlinear systems with memory (it is linear in its parameters – the Volterra kernels [92], [93]) many truncated/pruned, special cases of the Volterra series have been studied [91]–[94]. Three commonly studied, specialized cases of the Volterra series are the Wiener, Hammerstein, and Wiener-Hammerstein models, discussed later in this Chapter.

A method was proposed by Zhu and Brazil [85] to reduce the number of parameters in a Volterra series model by projecting the Volterra series onto a set of orthonormal basis functions called the Laguerre functions. Laguerre functions, de-

fined by their Z-transform, are given by

$$L_k(z,\lambda) = \frac{\sqrt{1-|\lambda|^2}}{1-z^{-1}\lambda}\left\{\frac{-\lambda^* + z^{-1}}{1-z^{-1}\lambda}\right\}^k \qquad k \geq 0 \tag{13}$$

with the Volterra model becoming

$$\begin{aligned}\tilde{Y}(n) =& \sum_{k=0}^{L-1} c_1(k) l_k(n) \\ &+ \sum_{k_1=0}^{L-1}\sum_{k_2=0}^{L-1}\sum_{k_3=0}^{L-1} c_3(k_1,k_2,k_3) l_{k_1}(n) l_{k_2}(n) l^*_{k_3}(n) + \cdots\end{aligned} \tag{14}$$

where

$$l_k(n) = \sum_{m=0}^{M-1} \phi_k(m)\tilde{X}(n-m) = L_k(z,\lambda)\tilde{X}(n) \tag{15}$$

It can be seen that the size, and thus accuracy, of the model depends on L, though it can also been seen that the use of Laguerre basis functions leads to a great reduction in the number of parameters needed when compared to the Volterra model.

Generally, when linear filters are used for Volterra filtering, the linear filters are extended into a multichannel system, with each parallel linear filter processing an order of the Volterra series. To more directly apply linear filtering techniques to Volterra filtering, V-vector algebra was developed in [94], preserving the time-shift property. The V-vector algebraic structure is that of a nonrectangular matrix, allowing Volterra filters to be treated in the exact same way as classical linear filters. Additionally, they suggest an extension of the V-vector algebra for linear multichannel systems, where the channels have different memory lengths.

The V-vector developed in [94] was then used in [92] to model a PA with nonlinear memory (due to the use of wideband signals). The V-vector was employed using parallel linear FIR filters, with the coefficients being solved for using the recursive least-square (RLS) algorithm.

Continuing from the V-vector algebra and its application in [94] and [92], respectively, Zhu and Brazil in [91] develop a *near-diagonality* structural restriction to simplify the Volterra series by pruning the redundant kernels. This elimination of some of the kernels reduces the total number of parameters in the Volterra series, allowing it to be used to model systems with higher-order nonlinearities and longer memory effects. Further, this near-diagonality restriction is actually a generalization of the memory polynomial, discussed later, which only includes on-diagonal terms. They define the distance from the diagonal as l, where $|i_m - i_n| \leq l$. Additionally, they imply that the distance away from the diagonal, l, can depend on the order – a larger value of l can be used for lower-order nonlinearities to model longer memory effects, while a smaller value of l can be used for higher-order nonlinearities. Lastly, results were provided, showing that the diagonality restriction improved complexity, greatly reducing the required number of parameters, while having very little effect on its ability to model the system.

A dynamic deviation reduction-based (DDR) Volterra model was proposed by Zhu, Pedro, and Brazil in [93], which is similar to that of the pruned Volterra series model presented by Zhu in [91]. They rewrite the Volterra series in **??** to be

$$\begin{aligned} y(n) = &\sum_{p=1}^{P} h_{p,0}(0,\ldots,0)x^p(n) \\ &+ \sum_{p=1}^{P}\left\{\sum_{r=1}^{p}\left[x^{p-r}(n)\sum_{i_1=1}^{M}\cdots\sum_{i_r=i_{r-1}}^{M} h_{p,r}(0,\ldots,0,i_1,\ldots,i_r)\prod_{j=1}^{r}x(n-i_j)\right]\right\} \end{aligned} \tag{16}$$

where r represents the order of the dynamics of the products. Thus, the pruning of the Volterra model is accomplished by restricting the value of r, such that $1 \leq r \leq R$. This is referred to as the DDR because r is the order of the dynamic deviation of the Volterra model. Additionally, the DDR Volterra model is much more flexible as

it has three parameters that can be altered, P, M, and r. Results for a Volterra model with an order $P = 5$ and memory of $M = 3$ were displayed in a well-organized table, showing that while when only first-order dynamics ($r = 1$) were considered the model performance was poor, but performance greatly increased when second-order dynamics ($r = 2$) were included. Further, while increasing the order of the dynamics only slightly improved the model performance, the peak performance was actually when $r = 3$ (for $r = 4, 5$ the performance was actually less than when the model was restricted to a maximum of third-order dynamics). The authors explain that this is actually a common occurrence in nonorthogonal Volterra models due to use of too many coefficients, adding more uncertainty to the estimation process. They DDR Volterra model provides an effective method for reducing the number of parameters in the Volterra model, and can actually lead to an increase, not only in computational efficiency and complexity, but also in model performance.

In the following subsections, simplified versions of the Volterra series will be reviewed. Generally, each model can be seen as taking a specific *cut* from the Volterra kernel. These models seek to reduce the number of terms, attempting to focus on the "most important" terms. Many of these models are what are referred to as "block" based models, meaning that their components can be broken down into different general blocks, such as static nonlinearity and frequency dependence (filter) blocks.

2.1.2 Wiener Model

The Wiener model is an important, special case of the Volterra series for three reasons: 1.) it only contains two *vectorized* polynomials (think of the Volterra kernels as matricies), which can be easily solved for, 2.) most RF systems/components can be generally represented as a Wiener model, and 3.) the use of blocks help give

the system a better physical representation. The Wiener model is made up of two blocks, an LTI system, $H(q)$, followed by a static nonlinearity, $N(\cdot)$, [81], [86], [87], shown in Fig 3. The Wiener model is a good, simplified, representation of a receiver; first there is generally an antenna and a BPF, which introduce linear frequency dependence and are represented by the LTI system, followed by an LNA, which can be represented (in the narrowband sense) by the static nonlinearity.

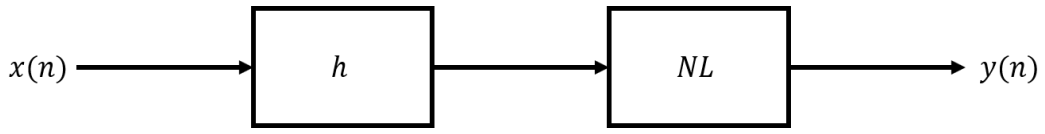

Figure 3: Wiener model block diagram

The RF Wiener model is given by

$$\begin{aligned} y(n) &= N[H(q)u(n)] \\ &= \sum_{k=1}^{K} a_k \left[\sum_{m=0}^{M-1} h(m)x(n-m) \right]^k \end{aligned} \tag{17}$$

where M is the memory depth and P is the order of the nonlinear polynomial. The number of coefficients for a Wiener model is simply $M + P$ allowing it to better model higher order, more strongly nonlinear systems. However, it can also be seen that the output $y(n)$ is *nonlinearly* related to the filter coefficients $h(n)$ [87]. Therefore, it can be stated that the Wiener model is *nonlinear* in its parameters, making it difficult to estimate. Lastly, a baseband representation with only odd-

order powers from [81], [86] is given in Eq. (18).

$$\begin{aligned} y(n) &= N[H(q)u(n)] \\ &= N[\sum_{m=0}^{M} b_m u(n-m)] \\ &= \sum_{p=1}^{P} h_{2p-1}[|\sum_{m=0}^{M} b_m u(n-m)|]^{2(p-1)} \times \sum_{m=0}^{M} b_m u(n-m)] \end{aligned} \tag{18}$$

Wiener models contain cross-terms – nonlinear terms consisting of the multiplication of multiple different time delays (i.e. $x(t)x(t-1)x(t-3)$). Most RF systems contain cross-terms (embedded in the general, Volterra series); however, in many cases the cross-terms do not dominate the overall nonlinear response. Further, cross-terms are more difficult to de-embed from a system response since they are, as shown by the Wiener model, nonlinear in their own creation. On the other hand, the cross-terms have a more intuitive physical relationship; think of the input signal bouncing around a device – a time delay – and then combining with the correct input or a different time delay. Lastly, the Wiener model has an inverse, in the Hammerstein model, described in the following subsection.

2.1.3 Hammerstein Model

The Hammerstein model is another important special case of the Volterra series for many of the same reasons why the Wiener model is important. In general, the Hammerstein model is the inverse of the Wiener model; that is, the Hammerstein model is described by a static nonlinearity, $N(\cdot)$, followed by an LTI system, $H(q)$, [81], [84], [86], [87], shown in Fig. 4. Further, if we cascade a Wiener and Hammerstein system (order doesn't matter) and the LTI systems and static nonlinearities of the models are inverses of each other (i.e. the Hammerstein model's LTI system is the inverse of the Wiener model's LTI system, etc.), the cascade actually becomes a

linear system. This relationship can be leveraged for nonlinearity mitigation, described later in this Chapter.

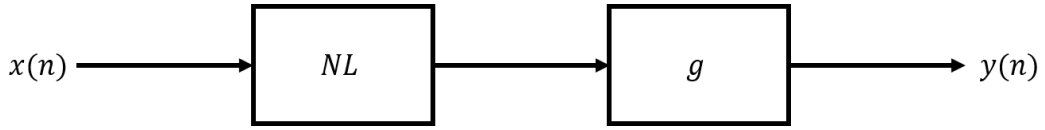

Figure 4: Hammerstein model block diagram

The RF Hammerstein model is given by

$$\begin{aligned} y(n) &= H(q)N[u(n)] \\ &= \sum_{m=0}^{M-1} g(m) \sum_{k=1}^{K} a_k x^k (n-m). \end{aligned} \tag{19}$$

As with the Wiener model, the Hammerstein model has $M + P$ coefficients; however, the Hammerstein model, since the nonlinearity precedes the frequency dependence, is *linear* in its parameters $(g(m)a_k)$ [81], [87]. This property makes the coefficients of the Hammerstein model much easier to estimate. Additionally, the baseband representation, with only odd-order powers, from [81], [86] is given in Eq. (20).

$$\begin{aligned} y(n) &= H(q)N[u(n)] \\ &= \sum_{m=0}^{M} b_m \sum_{p=1}^{P} h_{2p-1} |u(n-m)|^{2(p-1)} u(n-m) \end{aligned} \tag{20}$$

The Wiener and Hammerstein models are both special cases of the Volterra series, easily represented using block diagrams of a simple LTI filter and static nonlinearity. Furthermore, they are two of the simplest ways to represent nonlinear systems with memory effects, however this simplicity limits their effectivness for DPD or NLEQ. For example, in [95], the authors used a Hammerstein model-based approach to modele PAs with strong memory effects. As with the Hammerstein

model, first there was a static nonlinearity, but then instead of a simple LTI filter, a memory polynomial (MP)-based model was employed. Furthermore, instead of a simple MP model, an orthogonaly MP model was used to further lower the normalized mean-square error (NMSE), linearizing the PAs. The MP model, a generalization of the Hammerstein model, is discussed later in this chapter.

2.1.4 Wiener-Hammerstein Model

Another common block-based method used to capture a wider array of models is to add more blocks in series with a Wiener or Hammerstein model; a common version of this method is the Wiener-Hammerstein model. The Wiener-Hammerstein model, Fig. 5, is an LTI system followed by a static nonlinearity followed by another LTI system [81]. There is also a Hammerstein-Wiener model, which is a static nonlinearity followed by an LTI system and another static nonlinearity [96], [97] – it should be mentioned that this model is much less common in the literature than the Wiener-Hammerstein model.

Figure 5: Wiener-Hammerstein model block-diagram

The RF Wiener-Hammerstein model is given by

$$\begin{aligned} y(n) &= G(q)N[H(q)u(n)] \\ &= \sum_{m_1=0}^{M-1} g(m_1) \sum_{k=1}^{K} a_k \left[\sum_{m_1=0}^{M-1} h(m_1)x(n-m) \right]^k . \end{aligned} \tag{21}$$

The Wiener-Hammerstein model is more general than the Wiener or Hammerstein models themselves, but, as with the Wiener model, it *nonlinear* in the parameters. Though, it can easily be seen that the Wiener-Hammerstein model is a much more

realistic representation of both transmitters and receivers; for example, a receiver will first include a filter (being represented by the first LTI block), followed by an LNA (which can be modeled as a Hammerstein model, or the nonlinear block followed by the second LTI block).

Furthermore, branches can be added in parallel, adding some flexibility and generalization to the models – resulting in common models such as the parallel Hammerstein (PH) model (Fig 7) [86], [98], [99], the parallel Wiener model [87], [98], and the parallel Wiener-Hammerstein model [97].

2.1.5 Parallel Wiener Model

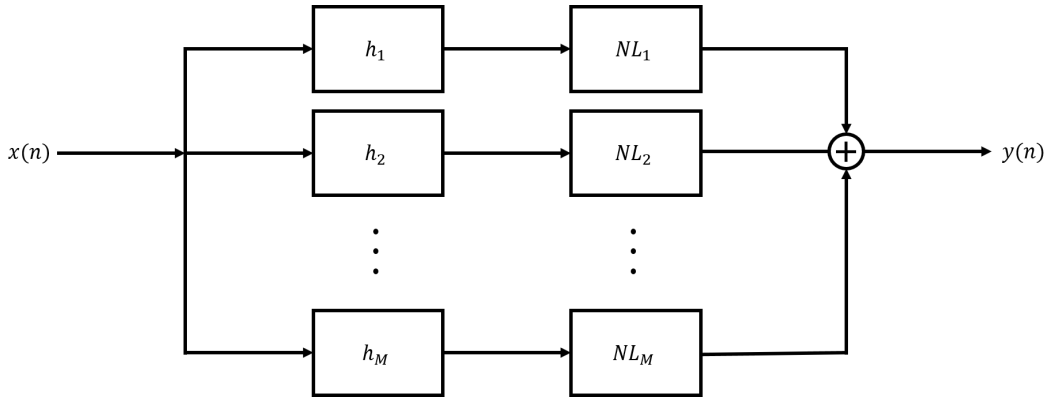

Figure 6: Parallel Wiener model block diagram

The parallel Wiener model, seen in Fig 6, is a generalization of the Wiener model. If we let $v_i(n)$ be the output of the i^{th} LTI filter, and let $y_i(n)$ be the output of the i^{th} nonlinearity, then we can define $v_i(n)$ as [40], [87], [98]

$$\begin{aligned} y_i(n) &= H_i(z)X(z) \\ &= h_i(n) * x_i(n) \\ &= \sum_{m=0}^{M-1} h_{i,m}x(n-m) \end{aligned} \tag{22}$$

and

$$\begin{aligned} y_i(n) &= \sum_{p=1}^{P} f_{i,p} v_i^p(n) \\ &= \sum_{p=1}^{P} f_{i,p} \left[\sum_{m=0}^{M-1} h_{i,m} x(n-m) \right]^p \end{aligned} \tag{23}$$

and, finally

$$\begin{aligned} y(n) &= \sum_{i=1}^{B} y_i(n) \\ &= \sum_{i=1}^{B} \sum_{p=1}^{P} f_{i,p} \left[\sum_{m=0}^{M-1} h_{i,m} x(n-m) \right]^p \end{aligned} \tag{24}$$

A parameter identification method for parallel Wiener systems was developed in [40]. This was accomplished by representing the first branch of the system with a memoryless model – thus $h_1(t) = \delta(t)$ – and finding NL_1 from single-tone measurements. Then using the cross-correlation function between the input and the error $\epsilon_i = y_i(t) - \hat{y}_i(t)$ to find $h_i, (i = 2, \ldots, M)$. Finally, the static nonlinear coefficients of $NL_i, (i = 2, \ldots, M)$ were determined by minimizing the mean square error (MSE), ϵ_i^2. New branches were added until the MSE was below a certain threshold.

2.1.6 Parallel Hammerstein Model

The parallel Hammerstein (PH) model is given by [86]. Let $y_i(n)$ be the i^{th} output of the static nonlinearity and let $y_i(n)$ be the output of the i^{th} LTI filter, then

$$y_i(n) = \sum_{p=1}^{P} f_{i,p} x^p(n) \tag{25}$$

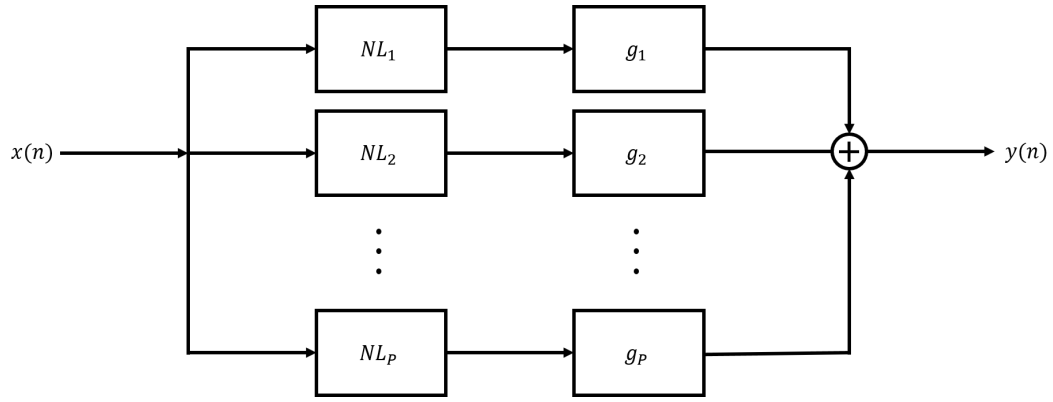

Figure 7: Parallel Hammerstein model block diagram

and

$$\begin{aligned} v_i(n) &= H_i(z)V_i(z) \\ &= h_i(n) * v_i(n) \\ &= \sum_{m=0}^{M-1} h_{i,m} v_i(n-m) \\ &= \sum_{m=0}^{M-1} h_{i,m} \sum_{p=1}^{P} f_{i,p} x^p(n-m) \\ &= \sum_{m=0}^{M-1} \sum_{p=1}^{P} h_{i,m} f_{i,p} x^p(n-m) \end{aligned} \tag{26}$$

and, finally

$$\begin{aligned} y(n) &= \sum_{i=1}^{B} y_i(n) \\ &= \sum_{i=1}^{B} \sum_{m=0}^{M-1} \sum_{p=1}^{P} h_{i,m} f_{i,p} x^p(n-m) \end{aligned} \tag{27}$$

Let each block in the be its own order. In that sense, the first block is just an LTI filter, the second block (odd order only) is simply a x^3 followed by an LTI.

Further, the baseband expression for the model, given in [86] is

$$\begin{aligned} y(n) &= \sum_{p=1}^{P} H_{2p-1}(q)|u(n)|^{2(p-1)}u(n) \\ &= \sum_{p=1}^{P}\sum_{m=0}^{M} b_{m,2p-1}|u(n-m)|^{2(p-1)}u(n-m) \end{aligned} \tag{28}$$

which shows that there is one parameter for each power p and delay m, resulting in a total of $(M+1)\times P$ terms. Typically, the second summation goes from 0 to $M-1$ and there are, thus, M terms. Further, the PH model, compared to the Hammerstein model, better models nonlinear memory effects – since each memory term of each power term has its own parameter. Though the PH model is a generalization of the Hammerstein and, thus, can model a wider range of nonlinear systems, it can contain many more parameters than the basic Hammerstein model. Additionally, it will be shown that the PH model is identical, mathematically, to the commonly used memory polynomial (MP) model.

2.1.7 Memory Polynomial

The difference between the standard Hammerstein model and the PH model is that the different orders are filtered by different filters $H_i(q)$. The PH model is also often referred to as a memory polynomial (MP) model. The Hammerstein model is actually a special case of the MP/HP model [98], and can be shown that for a matrix of MP coefficients

$$\mathbf{A} = \begin{bmatrix} a_{11} & a_{12} & a_{13} & \dots & a_{1M} \\ a_{21} & a_{22} & a_{23} & \dots & a_{2M} \\ \vdots & \vdots & \vdots & \ddots & \vdots \\ a_{P1} & a_{P2} & a_{P3} & \dots & a_{PM} \end{bmatrix}$$

Then, for a Hammerstein, the coefficients can be represented as vectors

$$\mathbf{c} = [c_1, c_2, \ldots, c_P]^T \tag{29}$$

$$\mathbf{h} = [h(0), h(1), \ldots, h(M)]^T \tag{30}$$

Therefore, it can be shown that a MP is a Hammerstein, with $a_{pm} = c_p h(m)$; thus $\mathbf{A} = \mathbf{c}\,\mathbf{h}^T$ [87], [98]. Furthermore, it has been shown that the MP is a special case of a parallel Wiener model [98], when

$$H_q(z) = z^{-q} \tag{31}$$

or

$$h_q(n) = \delta(n - q) \tag{32}$$

The MP model is a commonly model for nonlinear behavioral modeling, DPD, and NLEQ [41], [87], [98]. Simply, it is a truncated Volterra series, containing only the diagonal terms.

The MP model was used in [41] to model a nonlinear system with memory and its effectiveness was compared to that of a static memoryless model. The performance of the MP model was determined by using **??**, which was proposed in the paper. Additionally, it was shown that the MP model was effective at modeling the asymmetries in the IMD3 spurs. The authors in [98] used the MP model as a method for DPD for systems modeled with a Wiener-Hammerstein model, another MP model, a Wiener model, and a parallel Wiener model. It was further shown in this paper that the MP was also a parallel Hammerstein model, and ultimately offered a good compromise between generality and ease of parameter estimation/complexity.

The MP is a reduction of the Volterra series, where only the diagonal terms are

used [100]. Other variations of the MP model have been researched, such as the orthogonal MP and the GMP, which includes cross-terms [100]. Furthermore, there exists the envelope MP model, which only imparts the the magnitude information from the memory terms, given by

$$y(n) = \sum_{j=0}^{M} \sum_{i=0}^{N} a_{ji} x(n)|x(n-j)|^{i-1}. \tag{33}$$

This is similar to the cross-memory polynomial (CMP), which makes use of the magnitude of the static term, which imparting the phase information of the memory terms [101], given by

$$y(n) = \sum_{m=0}^{M-1} \sum_{p=1}^{P} a_{pm} x(n-m)|x(n)|^{p-1} \tag{34}$$

2.2 Generalized Memory Polynomial

$$\begin{aligned} y_{GMP}(n) &= \sum_{k=0}^{K_a-1} \sum_{l=0}^{L_a-1} a_{kl} x(n-l)|x(n-l)|^k \\ &= \sum_{k=0}^{K_b} \sum_{l=0}^{L_b-1} \sum_{m=1}^{M_b} b_{klm} x(n-l)|x(n-l-m)|^k \\ &= \sum_{k=0}^{K_c} \sum_{l=0}^{L_c-1} \sum_{m=1}^{M_c} c_{klm} x(n-l)|x(n-l+m)|^k \end{aligned} \tag{35}$$

2.2.1 NARMAX Model

The nonlinear autoregressive moving average model with exogenous inputs (NARMAX), described in [83], represents a wide class of nonlinear systems, given by

$$
\begin{aligned}
y(k) =& F[y(k-1), y(k-2), \ldots, y(k-n_y), \\
& u(k-d), u(k-d-1), \ldots, y(k-d-n_u), \\
& e(k-1), e(k-2), \ldots, e(k-n_e)] + e(k)
\end{aligned} \tag{36}
$$

where $y(k)$, $u(k)$, and $e(k)$ are the output, input, and noise of the system, respectively. Additionally, n_y. n_u, and n_e are the number of lags for the output, input, and noise of the system, respectively. The model can better be explained by comparing a linear finite impulse response (FIR) filter and an infinite impulse response (IIR) filter. Let the FIR filter be described as

$$
y(k) = b_1 u(k-1) + b_2 u(k-2) + \cdots + b_n u(k-n) \tag{37}
$$

and let the IIR filter be described by

$$
y(k) + a_1 y(k-1) + \cdots + a_n y(k-n) = b_1 u(k-1) + \cdots + b_m u(k-m) \tag{38}
$$

The importance of these differences were described in [83] – an FIR filter may often need 50 coefficients, while an IIR filter to describe the same system might only need 4 coefficients ($n = m = 2$). Though the FIR filter is often much easier to estimate, the IIR filter is much more concise – in this comparison, the FIR filter is equivalent to the Volterra series and the IIR filter is equivalent to the NARMAX model, which contains both delayed inputs and outputs.

2.3 Neural-Network

2.3.1 Radial-Basis Function Neural Networks

Radial-basis function neural networks (RBFNN) concist of three layers: 1. an input layer, 2. a hidden layer, and 3. an output layer. The RBFNN model structure proposed in [102] consists of $L+1$ input nodes, $\mathbf{x} = [r(n), r(n-1), \ldots, r(n-L)]^T$, where $r(n)$ is the input envelope, and two output nodes, $g(\cdot)$ and $f(\cdot)$. The output is given by

$$y(n) = g(r(n))e^{j(\Phi(n)+f(r(n)))} \tag{39}$$

where $\Phi(n)$ is the input phase. Thus, the proposed RBFNN has $M \times (L+3)+2$ parameters, where M is the number of neurons. Measured results were then taken in [102] using two different wideband CDMA (WCDMA) waveforms, one with a bandwidth of 4 MHz and the other with a bandwidth of 20 MHz. The performance of the proposed RBFNN model was compared to that of a PH model (referenced to be the same model used in [41], which was an MP model) by comparing their normalized mean-square error (NMSE) and adjacent channel error power ratio (ACEPR), given by

$$\begin{aligned} \bar{\epsilon} &= 10\log_{10}\left(\frac{\epsilon}{\sum_n |y_{meas}(n)|^2}\right) \\ \epsilon &= \sum_n |y_{meas}(n) - y_{RBFNN}(n)|^2 \end{aligned} \tag{40}$$

and

$$\text{ACEPR} = \frac{\int_{adj} |E(f)|^2 df}{\int_{ch} |Y(f)|^2} \tag{41}$$

respectively [86], [102]. The results from [102] show that the RBFNN had better

in-band performance (lower NMSE) than the PH model, while the PH model had significantly greater performance for out-of-band performance (ADEPR). Though, as the PH model is a commonly used model due to its effectiveness and efficiency at modeling nonlinear systems with memory, it is promising to see that the RBFNN model had similar performance. The same authors, in [86], extend the work done in [102] by comparing the PH and RBFNN models also to Volterra, Wiener, Hammerstein, and static nonlinarity models. Additionally, two different amplifiers (one for 2G and one for 3G) as well as two different waveforms and bandwidths. As in the previous study, the RBFNN model proved the most effective model at minimizing the NMSE, while the PH was best at minimizing the ACEPR. Furthermore, the models were cross-validated, where the PH had the lowest NMSE and ACEPR. It should be noted, however, that their the review conducted in [86] was not extremely rigorous and did not give a fair comparision of the performance of the different models. For example, computational time was not included and, while the number of parameters of the tested models were mentioned, the number of parameters of each of the models were not the same, giving an obvious advantage to the PH and RBFNN models. Lastly, they did not effectively show how sensitive the models were to changing the number of parameters – for example, some models may be more effective with few parameters, while others can better represent a system when a large number of parameters are used.

Different behavioral models for RF (power amplifiers) PAs were analyzed in [86]. The Wiener, Hammerstein, PH, radial basis-function neural network (RBFNN), and Volterra models were first discussed and then used to model two different PAs to determine the most effective model. Their results showed that the PH and RBFNN models were the most effective at modeling the two PAs; the PH had the lowest adjacent channel error power ratio (ACEPR), while the RBFNN had the lowest

normalized mean-square-error (NMSE). Furthermore, during cross-validation (A-B testing), the PH proved to be more robust, having a lower NMSE and ACEPR, than the RBFNN or other models. Though these are important insights, it should also be taken into account that the number of parameters in the models were not equivalent.

2.3.2 Comparison of the Models

Finally, to conclude this Section, we show some of the most significant results in the table below. These results are meant to help with the comparison of the models – comparing the number of parameters, error, and computational time. From the table we can see that the MP model had the best performance, in a sense of error, but suffered from a large number of parameters and high computational time. The Hammerstein-MP model as well as the parallel Hammerstein model make good compromises between generality, complexity, and the minimization of error.

Model	Order	Memory	no. params	Error (dB)	Time (s)
MP	7	3	12	-41.38	0.27
MP	7	4	16	-41.95	0.29
MP	9	5	25	-42.43	0.47
MP	17	9	81	-42.58	2.21
Hammerstein	7	4	8	-40.61	0.18
Hammerstein	9	5	10	-40.94	0.24
Hammerstein	17	9	18	-41.01	0.53
Wiener	7	4	8	-40.69	0.20
Wiener	9	5	10	-40.91	0.25
Hammerstein-MP	17, 13	3	30	-42.00	0.74
Hammerstein-MP	11, 15	6	38	-42.52	1.17
Hammerstein-MP	17, 17	9	90	-42.58	2.44
CMP	7	4	16	-40.69	0.21
CMP	9	5	25	-40.91	0.28
PH (B=40)	7	4	8	-41.90	2.71
PH (B=40)	9	6	11	-42.36	4.90
PH (B=40)	15	7	15	-42.44	11.72
PH (B=10)	7	4	8	-41.90	0.73
PH (B=10)	9	6	11	-42.31	1.31
PH (B=10)	13	8	15	-42.40	3.17

2.4 Nonlinear Distortion

Nonlinear devices produce intermodulation distortion (IMD), cross-modulation distortion (CMD – sometimes referred to as XMD), harmonic distortion, and compressive (or gain) distortion. First, we will take a look at IMD, CMD, and harmonic distortion. Assume that we have an input signal consisting of three sinusoids, given by

$$y_{in} = A_1 \cos(\omega_1 t) + A_2 \cos(\omega_2 t) + A_3 \cos(\omega_3 t) \tag{42}$$

where A_i are the amplitudes and ω_i are the frequencies of the three tones. Then the signal is passed through a third-order nonlinear system, given by

$$h(x) = k_1 x + k_2 x^2 + k_3 x^3 \tag{43}$$

where k_i are the coefficients of the nonlinear system. The resulting output of passing the signal through the nonlinear system is [103]

$$
\begin{aligned}
y_{out} &= k_1(A_1\cos(\omega_1 t) + A_2\cos(\omega_2 t) + A_3\cos(\omega_3 t)) \\
&+ k_2(\frac{1}{2}A_1^2(1+\cos(2\omega_1 t)) + \frac{1}{2}A_2^2(1+\cos(2\omega_2 t)) + \frac{1}{2}A_3^2(1+\cos(2\omega_3 t)) \\
&+ \frac{1}{2}A_1A_2(\cos((\omega_1-\omega_2)t) + \cos((\omega_1+\omega_2)t)) \\
&+ \frac{1}{2}A_1A_3(\cos((\omega_1-\omega_3)t) + \cos((\omega_1+\omega_3)t)) \\
&+ \frac{1}{2}A_1A_3(\cos((\omega_2-\omega_3)t) + \cos((\omega_2+\omega_3)t))) \\
&+ k_3(\frac{3}{4}A_1^3\cos(\omega_1 t) + \frac{1}{4}A_1^3\cos(3\omega_1 t) \\
&+ \frac{3}{4}A_2^3\cos(\omega_2 t) + \frac{1}{4}A_2^3\cos(3\omega_2 t) \\
&+ \frac{3}{4}A_3^3\cos(\omega_3 t) + \frac{1}{4}A_3^3\cos(3\omega_3 t) \\
&+ \frac{1}{4}A_1^2A_2(\cos((2\omega_1-\omega_2)t) + \cos((2\omega_1+\omega_2)t)) \\
&+ \frac{1}{4}A_1^2A_3(\cos((2\omega_1-\omega_3)t) + \cos((2\omega_1+\omega_3)t)) \\
&+ \frac{1}{4}A_1A_2^2(\cos((\omega_1-2\omega_2)t) + \cos((\omega_1+2\omega_2)t)) \\
&+ \frac{1}{4}A_1A_3^2(\cos((\omega_1-2\omega_3)t) + \cos((\omega_1+2\omega_3)t)) \\
&+ \frac{1}{4}A_2^2A_3(\cos((2\omega_2-\omega_3)t) + \cos((2\omega_2+\omega_3)t)) \\
&+ \frac{1}{4}A_2A_3^2(\cos((\omega_2-2\omega_3)t) + \cos((\omega_2+2\omega_3)t)) \\
&+ \frac{3}{4}A_1A_2A_3(\cos(\omega_1-\omega_2-\omega_3)t + \cos(\omega_1+\omega_2-\omega_3)t \\
&+ \cos(\omega_1-\omega_2+\omega_3)t + \cos(\omega_1+\omega_2+\omega_3)t))
\end{aligned}
\tag{44}
$$

The simplest and most straight forward way to represent a nonlinear system is

with a power-series, given by

$$h(x) = \sum_{i=0}^{N} k_i x^i. \tag{45}$$

Here we take a look at a third-order case, such as

$$h(x) = k_0 + k_1 x + k_2 x^2 + k_3 x^3. \tag{46}$$

Then, for simplicity we first show of a single sinusoid

$$x(t) = A(t)\cos\left[\omega_c t + \theta(t)\right] \tag{47}$$

is affected by the nonlinear system, such that

$$\begin{aligned}
y &= h[x(t)] \\
&= k_0 + k_1 x(t) + k_2 x^2(t) + k_3 x^3(t) \\
&= k_0 + k_1 A(t)\cos\left[\omega_c t + \theta(t) - \phi_1\right] \\
&+ \frac{1}{2}k_2 A^2(t) + \frac{1}{2}k_2 A^2(t)\cos^2\left[2\omega_c t + 2\theta(t) - 2\phi_2\right] \\
&+ \frac{3}{4}k_3 A^3(t)\cos\left[\omega_c t + \theta(t) - \phi_3\right] \\
&+ \frac{1}{4}k_3 A^3(t)\cos^3\left[3\omega_c t + 3\theta(t) - 3\phi_3\right] \\
&= k_0 + \frac{1}{2}k_2 A^2(t) \\
&+ k_1 A(t)\cos\left[\omega_c t + \theta(t) - \phi_1\right] + \frac{3}{4}k_3 A^3(t)\cos\left[\omega_c t + \theta(t) - \phi_3\right] \\
&+ \frac{1}{2}k_2 A^2(t)\cos^2\left[2\omega_c t + 2\theta(t) - 2\phi_2\right] \\
&+ \frac{1}{4}k_3 A^3(t)\cos^3\left[3\omega_c t + 3\theta(t) - 3\phi_3\right]
\end{aligned} \tag{48}$$

where the terms k_0 and $\frac{1}{2}k_2 A^2(t)$ fall at DC, $2\omega_c$ and $3\omega_c$ are the second and third

harmonics, and $\frac{3}{4}k_3A^3(t)\cos\left[\omega_c t + \theta(t) - \phi_3\right]$ induces AM-AM and AM-PM distortion as well as gain compression on the fundamental. From the nonlinearities produced by a signal tone two of the three main types of distortion have been demonstrated: harmonic distortion and gain compression. Looking at the output of two tones from the nonlinear system will yield examples of IMD and CMD as well:

$$x(t) = A_1(t)\cos\left[\omega_1 t + \theta_1(t)\right] + A_2(t)\cos\left[\omega_2 t + \theta_2(t)\right] \tag{49}$$

Then,

$$
\begin{aligned}
y(t) &= h[x(t)] \\
&= k_1 A_1(t) \cos\left[\omega_1 t + \theta_1(t) - \phi_{110}\right] \\
&+ k_1 A_2(t) \cos\left[\omega_2 t + \theta_2(t) - \phi_{101}\right] \\
&+ \frac{1}{2} k_2 A_1^2(t) \\
&+ \frac{1}{2} k_2 A_2^2(t) \\
&+ \frac{1}{2} k_2 A_1^2(t) \cos\left[2\omega_1 t + 2\theta_1(t) - \phi_{220}\right] \\
&+ \frac{1}{2} k_2 A_2^2(t) \cos\left[2\omega_2 t + 2\theta_2(t) - \phi_{202}\right] \\
&+ \frac{1}{2} k_2 A_1 A_2(t) \cos\left[(\omega_1 - \omega_2)t + \theta_1(t) - \theta_2(t) - \phi_{21-1}\right] \\
&+ \frac{1}{2} k_2 A_1 A_2(t) \cos\left[(\omega_1 + \omega_2)t + \theta_1(t) + \theta_2(t) - \phi_{211}\right] \\
&+ \frac{6}{4} k_3 A_1^2 A_2 \cos\left[\omega_2 t + \theta_2(t) - \phi_{301}\right] \\
&+ \frac{6}{4} k_3 A_1 A_2^2 \cos\left[\omega_1 t + \theta_1(t) - \phi_{310}\right] \\
&+ \frac{1}{4} k_3 A_1^3(t) \cos\left[3\omega_1 t + 3\theta_1(t) - \phi_{330}\right] \\
&+ \frac{1}{4} k_3 A_2^3(t) \cos\left[3\omega_2 t + 3\theta_2(t) - \phi_{303}\right] \\
&+ \frac{3}{4} k_3 A_1^2(t) A_2(t) \cos\left[(2\omega_1 - \omega_2)t + 2\theta_1(t) - \theta_2(t) - \phi_{32-1}\right] \\
&+ \frac{3}{4} k_3 A_1(t) A_2^2(t) \cos\left[(2\omega_2 - \omega_1)t - \theta_1(t) + 2\theta_2(t) - \phi_{3-12}\right] \\
&+ \frac{3}{4} k_3 A_1^2(t) A_2(t) \cos\left[(2\omega_1 + \omega_2)t + 2\theta_1(t) + \theta_2(t) - \phi_{321}\right] \\
&+ \frac{3}{4} k_3 A_1(t) A_2^2(t) \cos\left[(\omega_1 + 2\omega_2)t + \theta_1(t) + 2\theta_2(t) - \phi_{312}\right]
\end{aligned}
\tag{50}
$$

The second-order IMD (IM2) terms are given by

$$
\begin{aligned}
&\frac{1}{2} k_2 A_1 A_2(t) \cos\left[(\omega_1 - \omega_2)t + \theta_1(t) - \theta_2(t) - \phi_{21-1}\right] \\
&\frac{1}{2} k_2 A_1 A_2(t) \cos\left[(\omega_1 + \omega_2)t + \theta_1(t) + \theta_2(t) - \phi_{211}\right]
\end{aligned}
\tag{51}
$$

while the third-order IMD (IM3) terms are given by

$$\begin{aligned}
&\frac{3}{4}k_3A_1^2(t)A_2(t)\cos\left[(2\omega_1-\omega_2)t+2\theta_1(t)-\theta_2(t)-\phi_{32-1}\right]\\
&\frac{3}{4}k_3A_1(t)A_2^2(t)\cos\left[(2\omega_2-\omega_1)t-\theta_1(t)+2\theta_2(t)-\phi_{3-12}\right]\\
&\frac{3}{4}k_3A_1^2(t)A_2(t)\cos\left[(2\omega_1+\omega_2)t+2\theta_1(t)+\theta_2(t)-\phi_{321}\right]\\
&\frac{3}{4}k_3A_1(t)A_2^2(t)\cos\left[(\omega_1+2\omega_2)t+\theta_1(t)+2\theta_2(t)-\phi_{312}\right]
\end{aligned} \tag{52}$$

Additionally, CMD (here, referred to as CM3) is given by

$$\begin{aligned}
&\frac{6}{4}k_3A_1A_2^2\cos\left[\omega_1t+\theta_1(t)-\phi_{310}\right]\\
&\frac{6}{4}k_3A_1^2A_2\cos\left[\omega_2t+\theta_2(t)-\phi_{301}\right]
\end{aligned} \tag{53}$$

where there is some AM-AM induced from one signal onto the other, potentially leading to the desensitization [103] of the system. CMD is of extreme concern, especially for radar systems [104], however is often ignored since it doesn't lead to a very evident change in the spectrum.

2.5 Types of Nonlinear Distortion and Radar Considerations

The relationship between CMD and IMD were compared in [105], where it was determined that the effects of CMD need to be taken into account through vectoral addition. Assuming a desired signal

$$y_1(t) = a|H_1(jp)|\cos\left(pt+\phi_p\right) \tag{54}$$

where $|H_1(ip)|$ and ϕ_p are the modulus and phase at the frequency p, respectively, of the first-order transform of frequency p of $x(t) = a\cos pt + b\cos qt + c\cos rt$. Then introducing two 'unwanted' signals at frequencies q, r, we get the CMD given

by

$$|\Delta y| \cos(pt + \psi) = \frac{1}{4} ab^2 |A_{p,2q}| \cos(pt + \phi_{p,2q}) + \frac{1}{4} ac^2 |A_{p,2r}| \cos(pt + \phi_{p,2r}) \tag{55}$$

where

$$\begin{aligned} A_{p,q} &= |A_{p,2q}| e^{j\phi_{p,2q}} \\ &= H_3(jp, jq, -jq) + H_3(jp, -jq, jq) + H_3(jq, jp, -jq) \\ &+ H_3(-jq, jp, jq) + H_3(jq, -jq, jp) + H_3(-jq, jq, jp) \end{aligned} \tag{56}$$

where H_3 is the third-order transform for the frequencies p, q and q. The CMD is a complex quantity introducing both AM-AM and AM-PM distortion to the system. Then the increase in the output of frequency p can be written in complex form, as

$$\Delta y = \frac{1}{4} ab^2 A_{p,2q} + \frac{1}{4} ac^2 A_{p,2r}. \tag{57}$$

What [105] points out is that unless q and r are nearly equal, then the CMD is not simply $A_{p,2q} + A_{p,2r} = 2A_{p,2q}$ due to their imaginary parts. Essentially, they are added together as vectors, meaning that the CMD can both increase or decrease when more unwanted signals are added or removed. On the other hand, the IMD is given by the third-order transform H_3 of the frequencies p, q, and q with their relationship as $(2q - p)$, such that

$$y_{p,2q} = \frac{1}{4} ab^2 |B_{p,2q}| \cos[(2q - p)t + \phi_{2q,p}] \tag{58}$$

where

$$B_{p,2q} = H_3(-jp, jq, jq) + H_3(jq, -jp, jq) + H_3(jq, jq, -jp). \tag{59}$$

Finally, the CMD is related to the real part and the IMD is related to the modulus of the given distortion vector with their relationship between each other deviating at large frequency spacings between the modulation frequencies.

The effects of CMD on radar receiver dynamic range was investigated in [106]. In a radar, the effects of CMD are caused by the presence of a large interferering, or unwanted, signal that mixes with the desired, or wanted, signal to create some modulation [106]. These modulation effects are caused by the odd order nonlienarities in the receiver [106]. The subclutter visibility (SCV) is the attainable dynamic range of a radar is the ratio between the power of a spectral peak to the noise power in a Doppler cell [106]. However, CMD can introduce additional sideband power between range cells, desensitising the receiver. An equation was derived in [106], which will be included here:

Radar sensitivity should not be limited by internal noise or nonlinearities; receiver noise can be suppressed with gain stages, for example. However, the odd-order terms of receiver nonlinearities introduce IMD and CMD [107]. Some of the IMD terms created by large unwanted signals can appear above the noise floor, degrading the radar sensitivity [107]. On the other hand, in the case of CMD, the unwanted signal modulated the radar's signal-of-interest, essentially limiting the achievable sensitivity of the radar [107].

Additionally, for the case of digital arrays, the IMD signal power will grow by a factor of

$$N = 20\log_{10}(n)\text{dB} \tag{60}$$

where n is he number of receivers [107]. This is due to the coherent addition of the IMD signals and incoherent addition of the uncorrelated noise. The IMD will grow in voltage, by $20\log_{10}(n)$ dB, while the noise will grow by $10\log_{10}(n)$ dB; resulting in the IMD growing by $10\log_{10}(n)$ dB when compared to the noise, similar to the

actual received signals [107].

Amplifiers are used to increase the level of the signal (the gain of the system) prior to other receiver components, in order to prevent the noise from dominating the signal-of-interest and increase the system sensitivity [108]. Additionally, amplifier performance is typically specified with figures such as NF, gain, and IP3 [108]. Further, receivers must be able to tolerate large unwanted, interferering signals, often from users in adjacent channels [108]. Multiple strong interferering signals, paired with receiver nonlinearities can create IMD products that appear close to the desired signal; ultimately resulting in desensitization of the receiver – limiting it's ability to process very weak signals [108]. Additionally, a single strong interferer – often referred to as a blocker – can also result in receiver desensitization [108].

A large blocker reduces receiver sensitivity through two phenomone; the first is gain compression caused by the third-order nonlinearity [108]. The other, due to the second-order nonlinearity, upconverts low-frequency noise to the desired signal frequency [108].

In active array radars, IMD products experience an SNR gain, requiring higher system linearity [109]. Further, since the analog front-end often has a wider bandwidth than the instantaneous bandwidth of the radar system, signals that are out of the digitized bandwidth may produce IMD that fall on the desired signal (in-band) [109]. Additionally, interference can come from other transmitting systems, both in-band and out-of-band, as well as rain, sea, or land clutter [109].

2.6 Transmit Nonlinearities

Transmitter nonlinearities and digital pre-distortion (DPD) methods (used to mitigate Tx nonlinearities) have been heavily studied for almost three decades. A simple method to reduce system cost and power consumption is to operate the Tx power

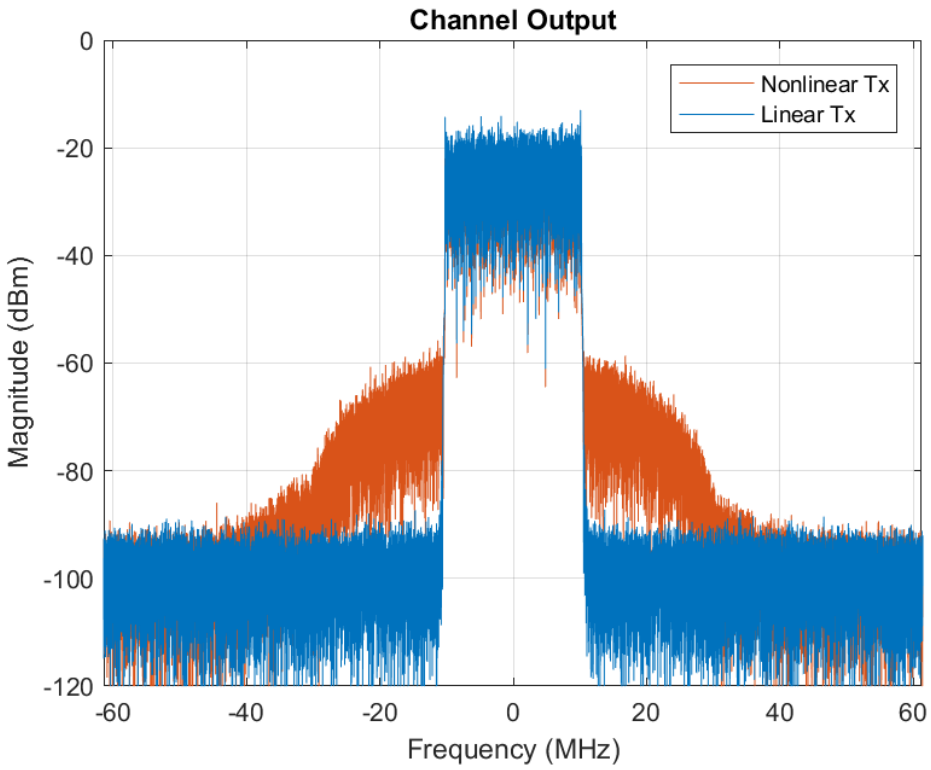

Figure 8: Nonlinear Tx channel, demonstrating IMD pollution of adjacent channels.

amplifier (PA) in the more efficient nonlinear region. Operating in the nonlinear region of a PA creates spurious products caused by IMD; degrading the error vector magnitude (EVM) of the in-band signal and polluting the already saturated wireless spectrum (OOB spectral regrowth is typically measured by the adjacent channel power ratio (ACPR) [110]) shown in Fig. 8 in orange – negatively effecting users in adjacent channels [17], [76], [111]–[113]. An efficient method for computing the location (in frequency) and magnitudes of IMD in a transmit PA was presented in [114]. Due to the efficiency benefits of operating in the nonlinear region, DPD has been heavily studied to mitigate the spectral spreading, while retaining the other desirable traits. DPD methods have also been proposed to mitigate Tx I/Q imbalances and crosstalk/mutual coupling present in MIMO systems [17], [33]. This section gives an overview of some of the different DPD techniques in published literature.

A MP model was proposed in [80] to correct power and frequency dependence in a wideband radar amplifier – specifically for use in a digital phased array. The authors also propose a Bayesian method making use of Gibbs sampling, a form of the Markov chain Monte-Carlo (MCMC) algorithm, which – compared to least-squares optimization – is able to gracefully adapt to changes in the amplifier's characteristics, including temperature variations. [115] analyzed the nonlinear distortion in MIMO transmitters caused by PAs. They simulated a 28 GHz, 64-element array with a four-stage class AB GaN MMIC PA, modeled by a memoryless power series. They further show that as the beam is steered and the active impedance of the array changes, then the PA load impedance also changes, degrading the effectiveness of DPD, which was trained at 50 ohms. The authors of [116] developed an impedance-dependent memory polynomial (IDMP) model for DPD of a wideband phased array radar. The IDMP takes into account the dependence on power, frequency, and impedance, all of which are affected by the scan angle and mutual coupling of the array. The IDMP was shown to be more effective than an MP at linearizing the PA of the phased array radar, and was proposed as a potential solution for MIMO communications DPD.

The authors in [117] presented an adaptive DPD method that can be implemented in a field programmable gate array (FPGA) for real-time adaptation. The DPD is made up of a predictive nonlinear auto-regressive moving average (NARMA) that is implemented by means of look-up tables (LUTs). An adaptive least mean-square (LMS) based correction called "nonlinear filtered-x LMS algorithm" with a Volterra series basis was implemented in [118]. The difference for an iterative pre-distortion and post-distortion solution is that the output of the pre-distortion adaptive filter can suffer from instability due to the filter delays. Filtered-x LMS provides an adaptive solutions without causing instability. Additionally, [119] pro-

vides a detailed explanation of the LMS algorithm.

A weighted MP (WMP) was proposed in [120] as the basis for the modeling and DPD of a PA. The WMP, given by

$$\begin{aligned} y_{WMP}(n) &= \sum_{i=0}^{N_s} \alpha_i w_s(\mid x(n) \mid) x(n) \mid x(n) \mid^i \\ &+ \sum_{i=1}^{N_D} \sum_{j=1}^{M} \beta_{ij} w_D(\mid x(n) \mid) x(n-j) \mid x(n-j) \mid^i, \end{aligned} \tag{61}$$

is shown to require half as many coefficients as the standard MP to achieve the same performance and is used to better handle high PAPR waveforms which, for a PA, exhibit mild nonlinear behavior and strong memory effects at low power levels, and strong nonlinear behavior with mild memory effects at higher power levels. A finite impulse response (FIR) MP DPD for wideband PAs was proposed in [121]. They showed that the derivation of a MP from the Volterra series is a consequence of the narrowband approximation, which is not valid for wideband signals. Therefore they precede the MP with an FIR filter to further reduce the frequency dependence of the PA. They show that their proposed FIR-MP DPD method further linearizes the PA with an 80 MHz waveform at 2 GHz by providing 11 dB more ACLR improvement. In [101], an FPGA-based DPD solution for PA linearization using a CMP model was provided. They further compare the effectiveness of the CMP model with a MP model with the same number of coefficients. The coefficients are solved for using recursive least squares (RLS), and the CMP proves to perform very similarly to the MP model, both of which greatly outperform the memoryless static power series. They further suggest that their method be implemented in an FPGA for cost-effective nonlinear circuit characterization and modeling. [112] proposed two methods for reducing the complexity of Volterra series, while providing

a more robust DPD basis than a simple MP. Methods of grouped Volterra series and pruned Volterra series are discussed and demonstrated for OFDM signals for massive MIMO systems, reducing the ACLR by 4 dB more than a memory-less correction, but showing little improvement over a MP basis. Lastly, the author of [112] states that there is less importance placed on the basis set used for DPD ACLR minimization, as long as the bases themselves span enough effective delays.

The mitigation of PA and I/Q nonidealities was demonstrated in [33]. The authors employed a PH based model, estimating the coefficients using a least squares based technique, showing effective mitigation of IMD for a wideband OFDM signal. MIMO systems also suffer from crosstalk or mutual coupling – which can be nonlinear (before the PA) or linear (at the antenna) [17], [35], [111]. Nonlinear crosstalk can have a great effect on DPD, and the authors of [17] proposed a crossover DPD (CO-DPD) model to mitigate the effects of crosstalk on PA linearization. They showed that CO-DPD could mitigate IMD of the PA almost 30 dB more than conventional DPD when the channel suffered from -20 dB of nonlinear crosstalk. The authors of [111] expanded the crossover model to include the correction of I/Q imbalance. Their measured results showed that their proposed method of the joint mitigation of nonlinearities, I/Q imbalance, and crosstalk resulted in a further reduction of the ACLR by 9 dBc, compared to the crossover model. The joint mitigation of nonlinearities, I/Q imbalance, and crosstalk was further explored in [122], where the authors used a real-valued MIMO MP (RMP) model, which considers the I/Q as separate input signals. This model showed good computational efficiency and effective ACLR mitigation. Additionally, a neural network DPD solution for crosstalk, I/Q imbalance, DC-offset, and PA nonlinearity was presented in [35].

Additionally, DPD has recently been studied for MIMO hybrid beamforming

cases, where each digital channel (and its' DPD) should support multiple PAs [76], [123]–[126]. That is, compared to single channel, element-level DPD, hybrid-beamforming DPD requires a single DPD solution for multiple PAs. Furthermore, the PAs in the analog beamformer can each receive different weights, leading to the PAs possibly operating in different nonlinear regions. Beam-oriented DPD was studied in [76], [123], [126] – focusing on the mitigation of IMD in the direction of the main beam and reducing DPD complexity by using one precoder per subarray. Finally, the nonlinear characteristics of each PA in an array differ from one-another and affect using the same DPD for multiple PAs, which was studied in [76], [126], [127].

The importance of DPD, especially for low-cost MIMO communication systems, cannot be overstated. DPD allows the PA to operate in the nonlinear region on Tx, which is more power efficient and further lowers the cost of the system. Additionally, DPD helps to lower the ACLR, contributing to a more efficient use of the spectrum and preventing the transmission of energy into sensitive bands – such as global positioning system (GPS) and aviation radar. Further, the most effective DPD methods are ones than can easily adapt to different waveforms and to changes in the nonlinear characteristics of the system due to temperature and/or frequency variations. Lastly, it is worth noting that in 2017 the first RF transceiver with on-chip DPD was released by Analog Devices – the AD9375 [128] – to be used in pre-5G massive MIMO systems. This COTS DPD transceiver is just the beginning of what will enable low-cost 5G systems.

Receive Nonlinearities There are two main differences between DPD and receive-NLEQ. On receive, compared to transmit, there is no *a priori* knowledge of the signals – especially in the case of wireless communications – and signals from multiple sources can move through the channel [30]. Secondly, a receiver chain

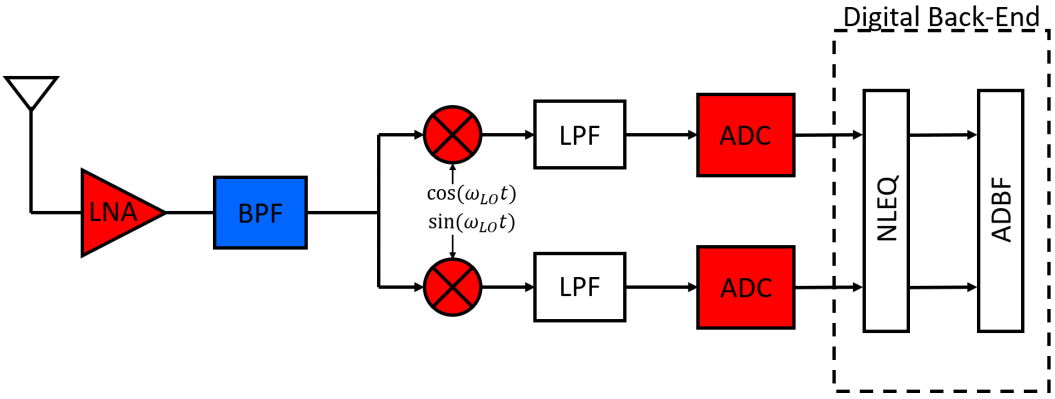

Figure 9: General nonlinear Rx channel of digital MIMO array with typical nonlinear components in red and the bandpass filter in blue, since it can be linear when active components are used for tuning.

typically contains a bandpass filter to remove OOB interferers, inducing frequency dependence on the received signals that is unnecessary on the transmit side [77]. Additionally, one of the major concerns of receiver nonlinearities for communications systems is that IMD can fall on top of weak desired signals, distorting the signal and increasing the bit-error-rate (BER) [129]. Lastly, a comprehensive review of analog techniques for linearization of RF receivers is given in [130], while here we continue to focus on DSP-based solutions.

Fig 9 shows a general MIMO array Rx channel consisting of multiple nonlinear components [131]. Perhaps the most studied culprit of Rx channel nonlinearities is the low-noise amplifier (LNA), due to the low-cost nature of operating in the nonlinear region. This is typically the first component after the antenna, defining the noise figure (NF) of the channel. The LNA is usually followed by a bandpass filter (BPF), used to filter any OOB interferers and the even-order IMD products. The BPF can be either a linear or nonlinear component depending on if it is passive or active, respectively. In reconfigureable systems, which make use of tunable components, the BPF tends to be nonlinear, further contributing to the RF nonlinearities of the system [77]. Additionally, the filter (either passive or active) contributes heav-

ily to the frequency dependence of the channel, requiring the use of memory terms in the NLEQ solution. The in-phase (I) and quadrature (Q) mixers are inherently nonlinear in nature, contributing baseband IMD to the system. Finally, the analog-to-digital converters (ADCs) can also be nonlinear in nature. The nonlinearities of each of these components compound to further increase the complexity of the NLEQ solution. Additionally, it was shown in [36] that IMD spurs in array beams are formed at predictable "apparent" directions, which has also been studied in [4] and [67].

The effect of amplifier nonlinearities on SNR and capacity for wireless communication receivers was studied in [132], showing that the IMD limits the maximum SNR and capacity. An analysis for system receiver nonlinearities in multi-band OFDM (MB-OFDM) systems is proposed in [133], specifically for the first band group of the Multi-Band OFDM Alliance (MBOA) standard [134], which contains three bands of 528 MHz each, in the frequencies between 3.1 and 4.8 GHz. With a maximum power spectral density (PSD) of -41.3 dBm/MHz, this band is particularly sensitive to strong interferers. The authors proposed a technique for the characterization of ultra wide-band (UWB) nonlinear systems, showing that the common two-tone text is only valid for narrow-band (NB) systems. Their proposed technique consists of analyzing the two-tone performance of the entire band, providing simulations to show its effectiveness.

The effect of LNA nonlinearities with memory for wideband spectrum sensing was studied in [135], where the spectral regrowth caused by a low-cost LNA can fall in unused channels, making them appear to have a user. Furthermore, the impact of receiver nonlinearities on spectrum sensing is studied in [131]. They consider the nonlinearities caused by the LNA and mixer, concluding that while the nonlinear distortion of both devices degrade the system performance, the LNA typically

dominates the system nonlinearities. LNA and mixer-induced receiver nonlinearities was further studied in [30], where the authors demonstrated the modeling and mitigation of RF and BB nonlinearities in direct conversion receivers, such as the receiver in Fig 9. This is accomplished with the use of three adaptive filters (AFs): one for I/Q balance, one for RF nonlinearities, and one for BB nonlinearities – further split into one for each I and Q. Normalized LMS (NLMS), which provides a more stable convergence than standard LMS, was employed along with a memoryless basis. The AFs proved effective at mitigating RF and BB nonlinearities, first for a two-tone input and then with a binary phase-shift keyed (BPSK) input to demonstrate its effectiveness at correcting high-PAPR signals. Lastly, they state that with the use of NLEQ allows for low-cost, low-complexity receiver architectures, specifically in the case of software defined radio (SDR) and cognitive radio (CR). The same authors, in [129], studied the improvement of the BER in Global System for Mobile Communications (GSM) by applying NLEQ. A similar technique was implemented in [136] to mitigate the spectral spreading of a strong BPSK signal that fell on a weak GSM signal. LMS was implemented, along with a real memoryless basis, on an FPGA in an SDR receiver, demonstrating an algorithm and implementation for real-world scenarios. Furthermore, the FPGA implementation proved to make a very efficient use of the computational resources with little processing delay. NLMS was again applied in [27] to implement a blind correction of nonlinearities in a wideband receiver.

An NLEQ method for assisting a tunable channel select filter (CSF) realized in 65 nm CMOS was implemented in [137]. A low-resolution, oversampling auxiliary ADC was used to capture in-band and OOB interferers and IMD, and then applied LMS to mitigate the nonlinearities. The LMS NLEQ did not update continuously to save power, but updated periodically to account for process, voltage, and tem-

perature (PVT) variations. An auxiliary ADC in CMOS was also used in [79] to mitigate nonlinearities and extend the SFDR, specifically for phased array radars. Furthermore, the sampling speed of the auxiliary ADC was reduced to further save power and continual background calibration was used to account for PVT variations, specifically temperature. Lastly, the effectiveness of background calibration compared to single temperature calibration was shown for 10° C to 80° C.

RF NLEQ for direct conversion receivers was further studied in [4], showing that the IMD spurs in a digital array radar (DAR) – in this case consisting of a direct conversion 4x4 digital array and low-cost commercial off-the-shelf (COTS) components – tend to correlate spatially. The RF spurs were mitigated with the use of NLEQ and LO out-phasing. LO out-phasing suppresses the even-order spurs through decorrelation – all even order products will have a random phase applied to them so that when DBF is performed, they add in power instead of voltage, giving a $10\log_{10}(N)$ mitigation where N is the number of elements in the array. A weighted least-squares (WLS) version of NLEQ was used to deal with the odd order spurs, which tend to correlate spatially as explained in [36].

Similarly, IMD effects on phased arrays due to interferers was studied in [67]. The authors show the results of the impact of three interferers on a 32-element 28 GHz array for 5G applications by showing how system-level IIP3 changes with scan angle due to the spatial IMD caused by the interferers. This further shows the need for receiver side NLEQ in interferer-filled 5G environments, as well as more effective linearity metrics.

All the previously mentioned methods of NLEQ are applied after the received signal has passed through the RF front-end, meaning that if the incoming signals are too strong they can push the LNA too far into compression for NLEQ to effectively model; at this point the linear signal cannot be completely recovered. Another

possibility is for the ADC to saturate, clipping the high-power portions of the signal, which again leads to information loss. This leads to the DR being defined not by the linearity of the RF front-end (when effective NLEQ techniques are implemented), but by its ability to handle strong interferers. To this end, extending the DR of MIMO receivers further requires analog interferer mitigation. Specifically, mitigating strong spatial interferers will suppress the in-band interferers that the RF filter cannot, and will allow the LNA to safely be placed directly after the antenna (before the filter) to minimize the system's NF.

Receiver NLEQ provides a very effective method of mitigating IMD, extending the DR and linearity of low-cost MIMO systems. With the very saturated spectral environment and the lack of inherent spatial filtering in fully-digital arrays and MIMO systems, mitigating nonlinearities caused by strong blocker signals is necessary for operating at the data rates demanded by 5G. Furthermore, adaptive NLEQ solutions that can adjust to different combinations of received signals and to changes in the nonlinear characteristics of the receiver are the most promising for extending the DR and capacity of real 5G MIMO systems.

2.6.1 Summary of NLEQ Techniques

In general, a system-specific NLEQ basis such as the pruned Volterra series presented in [112] provides the best combination of computational efficiency (number of computed terms) while remaining a mathematically robust model. Furthermore, it has been shown that an adaptive solution, such as LMS, provides the most dynamic method for mitigation of spectral pollution for Tx and spectral regrowth due to strong interferers for Rx. Lastly, it should be noted that IMD correlate in space (during beamforming), meaning that a two-fold solution is required in mitigating IMD in the individual channels, while also decorrelating the IMD at the array-

level. This is of particular importance for the receivers, where IMD, both spatial and spectral, can distort the SoI – especially in the case of strong spatial interferers.

3 Digital Array Modeling and Dynamic Range

When designing a modern digital array, whether it be for radar or wireless communications, one of the initial steps is to attempt to model and simulate the system [138]. Of course, there are many tools and simulators, but, in general, many lack the ability to simulate an entire digital array with nonlinearities and other impairments. One such tool is the MATLAB Phased Array System Toolbox, which was demonstrated in [138]. One of the advantages of the MATLAB Phased Array System Toolbox is its ability to simulate the entire array, from the element pattern, to the geometry to an entire radar system. Additionally, the user can add imperfections in the array, which need to then be calibrated. However, one capability missing from the toolbox is the ability to simulate component-level impairments. A phased array system simulator, which included the modeling and simulation of component-level impairments was discussed in [139]. This simulator, also written in MATLAB, was called the Nonlinear Array System Modeler (NASM) and was further used to simulate a nonlinear receive array in [23]. Modeling and simulating a digital array system can help to make the design process more straightforward and cost-effective [138]. Additionally, it is important to be able to effectively model all potential nonidealities in the array system. This Chapter, then, discusses different ways to model and simulate digital array systems. Further, the DR concerns for digital arrays are reviewed, as well as decorrelation methods to extend the DR of a digital array system.

3.1 Modeling and Simulation

This Section will go over a number of different factors to take into account when attempting to model and simulate an array system, whether it be fully-digital, subarray digital, or analog. First, the most common transceiver architectures will be

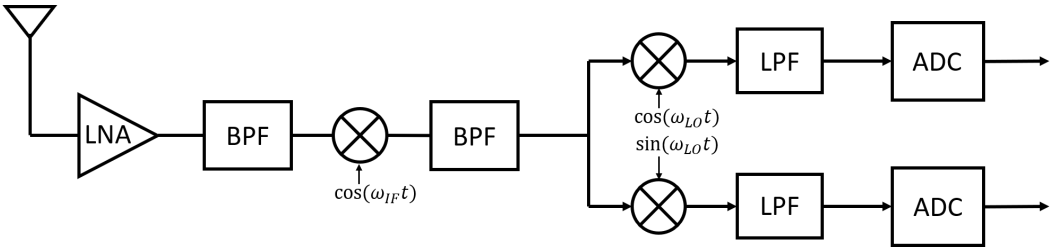

Figure 10: An example of a superheterodyne receiver.

reviewed – the architecture chosen will ultimately determine which and how many components need to be modeled. Next, methods for modeling specific components, such as amplifiers and mixers, will be discussed. Lastly, a general procedure for setting up an array simulation will be shown.

3.1.1 Transceiver Architectures

Other than the array geometry, the transceiver architecture is one of the more general topics of system design that will greatly impact how the system performs and what kinds of impairments can/will occur. The three types of transceiver architectures that will be breifly discussed here are the super heterodyne, the direct-conversion (also referred to as homodyne), and direct sampling. Here these architectures are discussed in terms of the receivers, however the architectures are nearly identical for transmitters.

The superheterodyne receiver, Fig. 10, has been, historically, a very popular receiver. First, the RF is mixed down to some intermdeiate frequency (IF), allowing the IF to be a lower frequency than the RF. However, this first mixer adds more complexity to the receiver, not only in the mixer and LO required for the IF, but also in the requirement of the proceeding image-reject filter – filters are often the largest component in modern integrated circuit (IC)-based systems. Additionally, a superheterodyne receiver can have multiple IF stages, each requiring additional image reject filters. However, over the past decade or two, with the increased demand

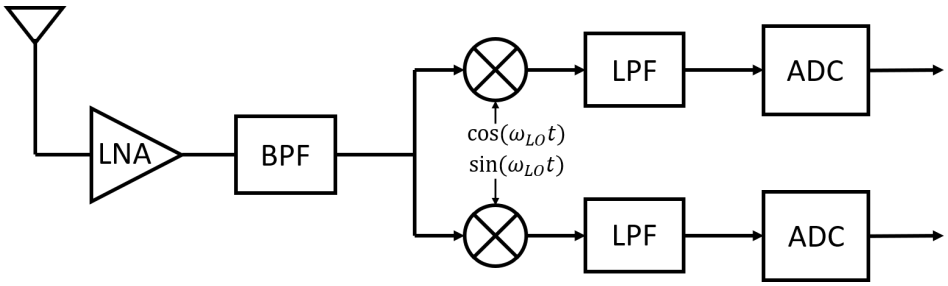

Figure 11: An example of a direct conversion (homodyne) receiver.

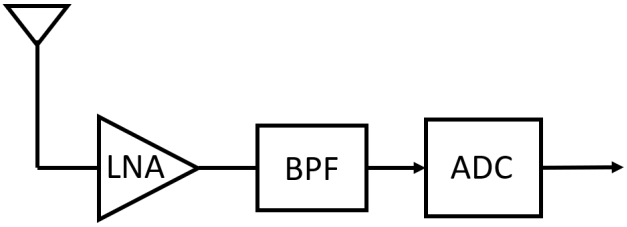

Figure 12: An example of a direct sampling receiver

for wireless communication devices, which require minimal form factor, the direct conversion receiver (DCR) have become the architecture of choice [81], shown in Fig. 11. One of the main advantages has to do with the removal of the additional mixer(s), each of which would requires an image reject filter [29], [140]. However, DCRs can also suffer from an increase in phase noise for the LO compared to the superheterodyne receiver. This is becasue the LO of the DCR is at a higher frequency than the LO of the superheterodyne receiver and phase noise scales with frequency. Additionally, there is a possibility that the has more baseband (post-mixer) gain stages, which can produce additional baseband nonlinearities and increased I/Q-imbalance, which can be corrected with DSP [28], [29].. Lastly, there are direct sampling systems, an example is shown in Fig. 12. The direct sampling receiver does not include a mixer; the ADC samples the RF signal directly. Some of the advantages of a direct sampling architecture is the removal of LO phase noise, removal of I/Q-imbalance, and mitigation of a DC-offset.

3.1.2 Amplifier

Amplifiers are typically described by their gain, NF, and nonlineaity (e.g. input third-order intercept (IIP3)/output third-order intercept (OIP3) and P1dB). Additionally, digital arrays generally make use of solid-state amplifiers – semiconductor technologies suffer from process-voltage-temperature variation (PVT), which introduce channel variations in the array. The focus of these variations has often been on the gain of the amplifier; gain variations in phased array channels leads to poor beamforming, changing the beamwidth and sidelobe levels. However, the variations in nonlinearity has began to receive more attention [23], [77]. Finally, amplifiers' gain and nonlinearity also change with frequency, therefore some frequency response needs to be further modeled [77]. Chapter 2 went over different models for nonlinear systems; for simplicity we will take a look at modeling the amplifier as a Wiener, Hammerstein, and Wiener-Hammerstein system.

As we want to be able to effectively model an amplifier, it is important to look at these different models to show how the order of the frequency response affects the amount of nonlinearity, or spectral regrowth, that shows up in the output of the system. For example, if the filter is first, then there could be a reduced signal into the nonlinearity and if the signal is knocked down 1 dB then the nonlinearity is changed 3 dB and hence is the same nonlinearity. Otherwise if the nonlinearity is first then the IM3 and main tones are changed the same amount. This is the difference between Wiener and Hammerstein. Additionally a Wiener-Hammerstein system will include some combination of this and therefore, is the most accurate in adding gain and nonlinearity variations throughout the bandwidth.

Recall from Section 2 that the Wiener and Hammerstein models are inverses of each other; each being made up of a static nonlinearity (power series) and an LTI system (in this case we use an FIR filter). First, before we can compare how the

order of the nonlinearity and the filter effects the spectral output, we must design each block. The nonlinearity is selected to be fifth order (odd-order only), with coefficients of

$$c = [1 \quad -0.03 \quad 0.02]. \tag{62}$$

Then, the frequency response of the system is chosen to also consist of three terms for simplicity; the FIR coefficients are

$$a = [0.9 \quad -0.1 \quad 0.05]. \tag{63}$$

Figure 13 shows the input-output power of the nonlinearity as well as the frequency response of the LTI system.

A two-tone comparison was made between the two models; two tones of frequencies -1 MHz and 15 MHz inside a bandwidth of 100 MHz (-50 MHz to 50 MHz) at an input power of 3 dB. Figure 14 shows the output of each stage of both the Hammerstein and Wiener models. From this, we can see that, at least for this case, the nonlinear spurs are directly affected by the frequency response for the Hammerstein model – this is an obvious conclusion given that the output of the nonlinear block then passes through the LTI system. However, the consequence of this is that the Hammerstein model as a larger effective bandwidth when the frequency response of the system is applied. On the other hand, the input of the Wiener model is the only section of spectrum that is directly affected by the frequency response – for a fifth order system this means twenty-percent of the bandwidth that is affected in a Hammerstein system. Generally, larger bandwidths suffer more greatly from memory effects (frequency dependence); therefore, a reasonable conclusion can be that since Hammerstein systems have a greater effective bandwidth when affected by the system's frequency response, Hammerstein systems add more fre-

quency dependence to the output. Finally, the dynamism of the frequency response will ultimately determine which model imparts more frequency dependence on the system.

Figure 15 compares the output of the Hammerstein and Wiener models. The resulting magnitudes of the input tones are approximately identical for the two models, while there are noticeable differences between the nonlinear spurs. From the magnitudes of the third-order and fifth-order spurs, we can see that the magnitudes of the upper and lower spurs vary more greatly for the Hammerstein model. Again, it at the point the reader should be reminded that these results are for the specific nonlinear and LTI blocks that were selected.

Additionally, Figure 16 shows the output from each of the different stages of the Wiener-Hammerstein model. The resulting output for this case is nearly identical to the output of the Hammerstein model – again, this is due to the more narrow-band affect of the two-tones through the pre-nonlinearity LTI block. From this, we can determine an effective way to model an RF amplifier and its nonlinearities.

A Wiener-Hammerstein model is the most promising due to its ability to add both narrow and wideband frequency dynamics. The first filter should be used to throttle the level of nonlinearity (i.e. the P1dB) of the system, while the second filter will add the frequency dependence of the whole system – the second filter should also have greater ripple (higher order filter), with a much higher derivative of its frequency response.

3.1.3 Mixer

A mixer can contribute many different types of distortion, which all need to be modeled to effectively simulate a phased array system. Firstly, the phase noise from the LO will contribute to the overall noise in the system; however this noise

will combine directly with the received signal and will be spectrally on top of the received signals. Additionally, if many elements in an array share the same LO or reference, the correlation of the phase noise needs to be modeled. Generally, the phase noise can improve at a rate of $10\log_{10}(N)$ dB where N is the number of independent LOs in an array [141]. Additionally, mixers introduce a DC-offset (or LO leakage), which can dominate weaker signals, especially ones that are centered in the band. Further, mixers in an I/Q receiver can be unbalances – having some differences in phase and amplitude between the inphase and quadrature channels. Even though I/Q-imbalance can be digitally corrected for, it is important to be able to effectivenly modeling it when designing a system. Not only as a method of testing the I/Q-balancing algorthim, but also to determine the limitations of the selected components for the system, or the requirements of the components based on system requirements.

3.2 Digital Array Dynamic Range

Dynamic range is an important metric for all types of systems, but is especially important when it comes to radar systems. Taking a look at the radar range equation, given by [142]

$$R_{max} = \left[\frac{P_t G_t G_r \lambda^2 \sigma}{(4\pi)^3 S_{min}}\right]^{1/4} \tag{64}$$

shows that the radar return signal suffers R^4 losses. On the other hand, interfering signals only suffer the standard R^2 propagation losses. Therefore, a radar receiver needs to be able to detect the smallest possible radar return, while also being able to handing the higher power interfering signals. How great this ability is, is essentially defined as the DR of the system. However, as was discussed in [143], [144], there are many definitions for DR and the task of choosing the correct definition can be

daunting. Further, in general, for a digital array, the DR improves on the order of $10\log_{10}(N)$ dB, where N is the number of transceivers [8], [23], [24], [144]. However, this increase in DR is typically limited by the correlation of spurious products.

An example of one type of the correlated spurs is shown in Fig. 17, where two CW tones at two different angles push a receiver into its nonlinear region. This generates two IM3 that correlated during beamforming to predictable angles, discusses in detail in [36]. However, with the addition of NLEQ, the spurs can be mitigated, essentially decorrelated, improving the system SFDR. Additionally, the main components that are going to generate correlated spurs, generally, will be the two components discussed earlier in this Chapter: the amplifier and the mixer. Further, the previous Chapter discussed NLEQ techniques for mitigating amplifier nonlinearities, which is the technique that was used to extend the DR of Fig. 17. On the other hand, current techniques for the mitigation, or decorrelation, of spurs were discussed in detail in [144].

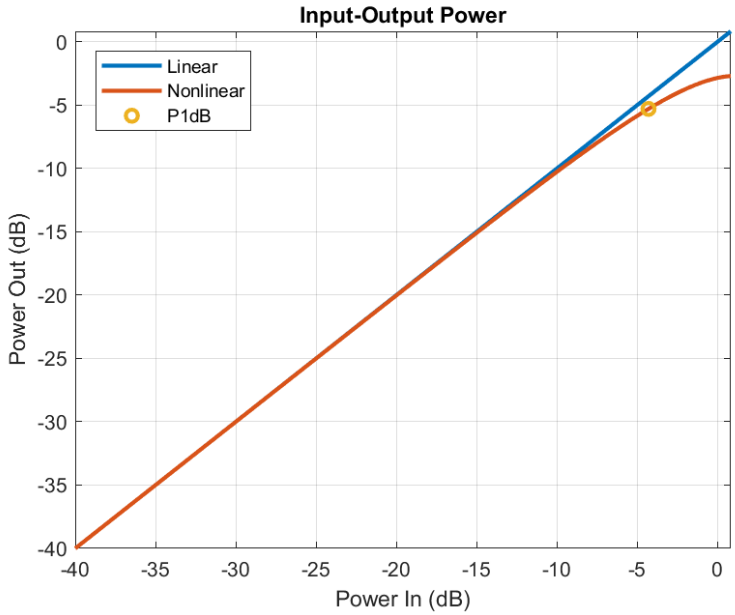

(a)

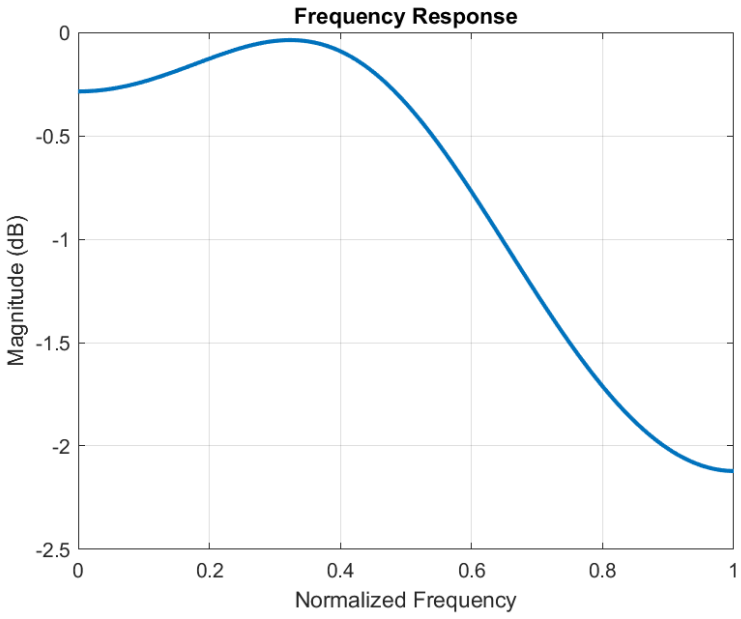

(b)

Figure 13: The two fundamental blocks of nonlinear systems; (a) the input-output power plot describing the static nonlinearity block, and (b) the frequency response of the LTI system block.

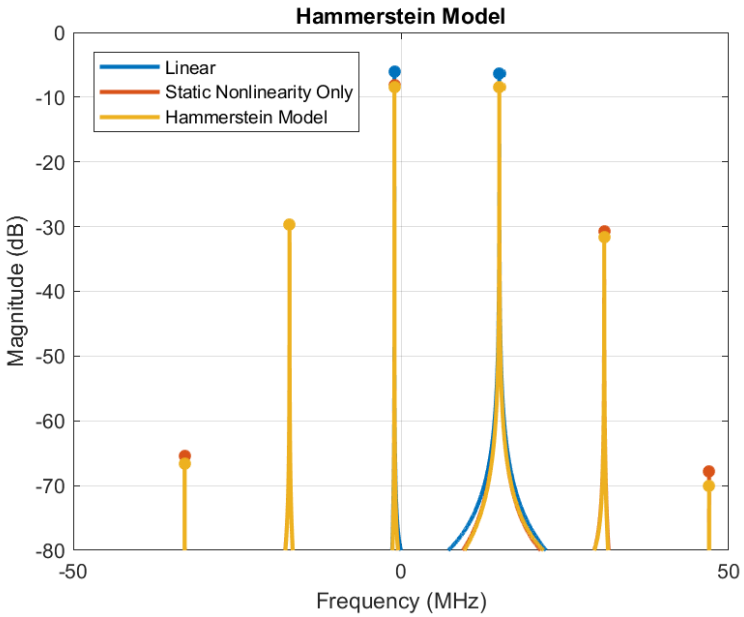

(a)

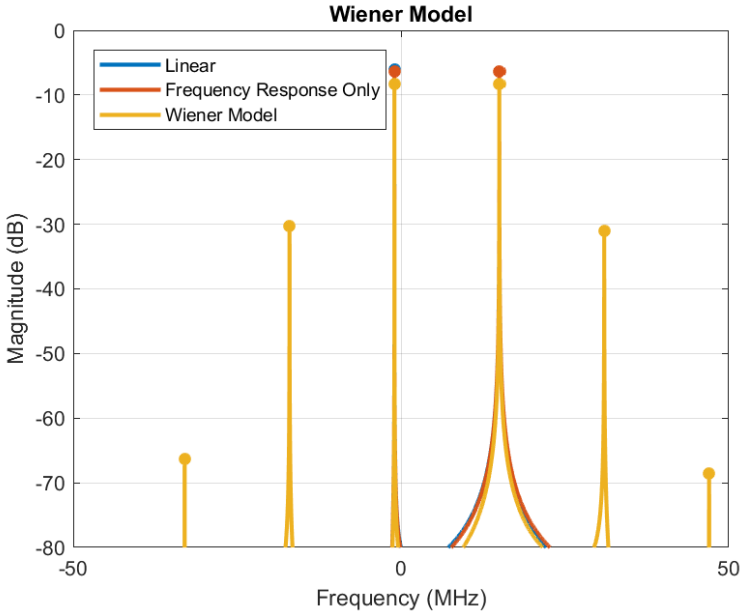

(b)

Figure 14: Step by step plots of a signal of two CW tones passing through (a) a Hammerstein model system and (b) a Wiener model system. These plots show how the placement of the LTI system and the nonlinearity affect the magnitude of the resulting signals.

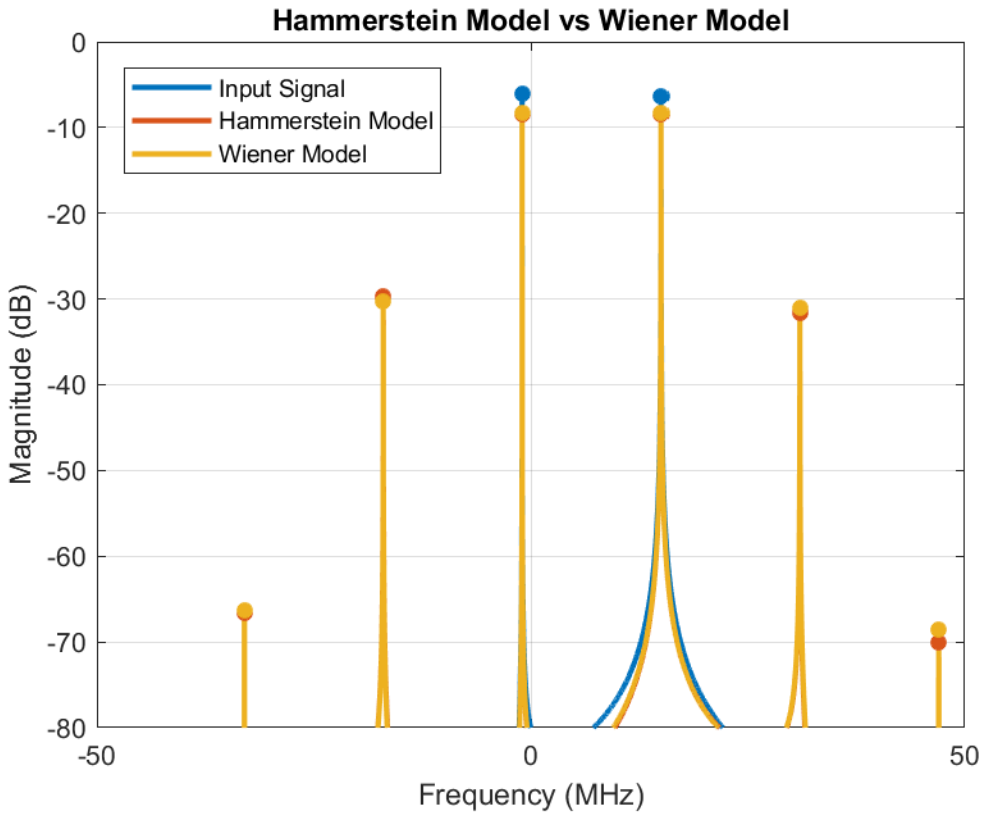

Figure 15: Comparison between the output of a Hammerstein model and a Wiener model when two CW tones are input into their nonlinear region. It is evident that the location of the nonlinearity and frequency dependence can impact the magnitude of the resulting nonlinear spurs, as well as the main input signals.

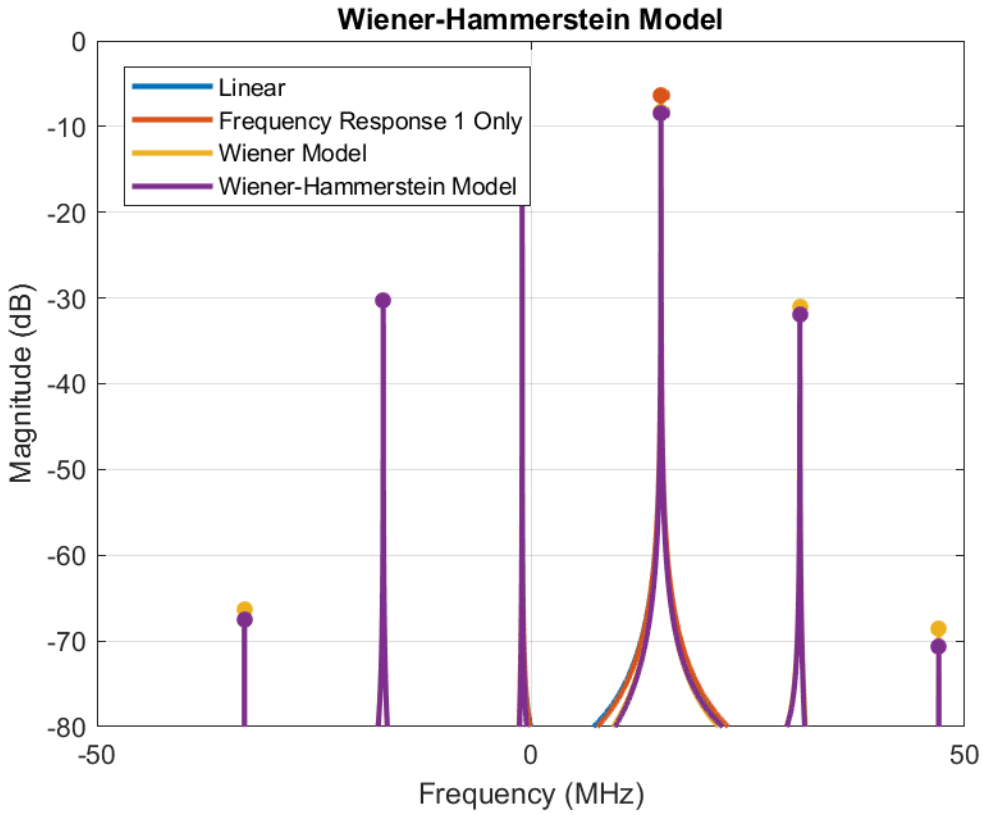

Figure 16: An step-by-step example of two CW tones passing through the nonlinear region of a Wiener-Hammerstein Model.

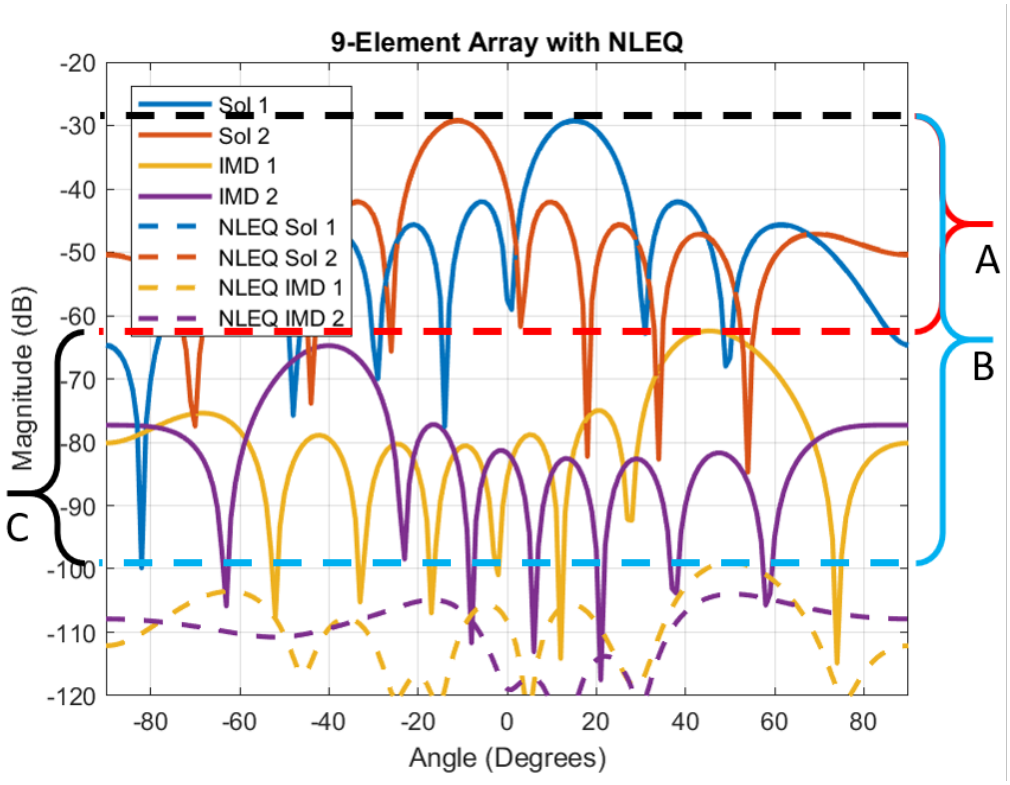

Figure 17: Digital beamforming results from [23], [144], showing two received signals and their nonlinear IM3 spurs. (A) the SFDR of the array, limited by the IM3, (B) the SFDR of the array with NLEQ, and (C) the DR improvement with NLEQ.

4 Waveforms for Nonlinear Calibration

The calibration waveform plays a large role in the effectiveness and accuracy of the training, both for NLEQ and DPD [23]. Similarly so, the waveform used for nonlinear behavioral modeling has been shown to determine the accuracy and speed at which a nonlinear system can be modeled [40], [41], [84], [89], [145], [146]. Further, the calibration waveform, in addition to the nonlinear model from Section 2, is one of the most crucial aspects in linearization.

Simply, the complexity required for the calibration of a nonlinear system is, in general, based on three things:

1. System bandwidth: is the system operating in a narrowband or wideband sense? In this case, and throughout the paper, narrowband refers to a situation in which the frequency response of the system is flat [145], while the wideband sense must take into account the changing frequency response of the system.

2. The dynamism of the signals going through the system: for Tx DPD this may be more straightforward as the user, and often times the system engineers, have *a priori* knowledge and control of the waveforms going through the system. On the other hand, for Rx NLEQ more caution needs to be taken toward the surrounding spectral environment; especially in this increasingly crowded spectral environment, many more signals other than the signal-of-interest (SoI) will likely go through the Rx chain.

3. Calibration time and nonlinear model complexity, e.g. the number of coefficients required, the length of waveform, etc.

Therefore, an ideal calibration waveform (and model) would integrate/train over the system bandwidth, while being generalized enough to handle all types of signals

that will go through the system. Further, obviously a quick calibration time is highly desired, especially for *in situ* calibration of a fielded system. One factor that affects the calibration waveoform's time is how long (how many samples) the waveform spends at the nonlinear region – the high power region – without pushing the system too far into saturation. This, in general, is determined by the waveform's crest factor and, thus, the peak-to-average power ratio (PAPR).

A waveform's crest factor is given by

$$C = \frac{|x_{peak}|}{x_{rms}} \tag{65}$$

while the PAPR of a waveform is given by

$$PAPR = \frac{|x_{peak}|^2}{x_{rms}^2} = C^2 \tag{66}$$

where x_{rms} is given by

$$x_{rms} = \sqrt{\frac{1}{N}\sum^{N} x_i^2}. \tag{67}$$

It is well known, and easily seen, that a single sinusoid has an of $\frac{1}{\sqrt{2}}$ and, thus, a PAPR of about 3 dB. Further, as the number of sinusoids increases by N, the also increases by a factor of $\sqrt{N}$, leading to a PAPR of $10\log_{10}(2N)$ dB. It is also well known that has an infinite PAPR – however, the PAPR is finite for a bandlimited case.

A waveform with a lower PAPR will spend more time at the higher power levels of the signal compared to a signal with a large PAPR. Further, the maximum power of a signal will determine how far into saturation the nonlinear system is being probed and, ultimately, will determine power of the waveform allowed for nonlinear calibration. In other words, the peak power allowed into the nonlinear system will

be set based on the nonlinear characteristics such as P1dB and IP3. Then, based on the PAPR of the waveform, the waveform power can be determined. Therefore, waveforms with a lower PAPR can have a larger total power to probe the nonlinear system, and will be able to probe the higher power, nonlinear regions of the system – without driving the system too far into saturation – for a larger percentage of the total signal length.

Another important thing to take into account when determining the calibration waveform for a nonlinear system is the nonlinear terms that will be created from the waveform. For example, the classic two-tones given by $x_1(t) = A_1 e^{j\omega_1 t}$ and $x_2(t) = A_2 e^{j\omega_2 t}$ when passed through the third-order nonlinear system

$$y_{out} = k_1 y_{in} + k_2 y_{in} |y_{in}|^2, \tag{68}$$

with linear coefficient k_1 and third-order nonlinear coefficient k_3, will result in

$$\begin{aligned} y_{out} =& (k_1 A_1 + \frac{3}{4} k_2 A_1^3 + \frac{3}{2} k_2 A_1 A_2^2) e^{j\omega_1 t} \\ &+ (k_1 A_2 + \frac{3}{4} k_2 A_2^3 + \frac{3}{2} k_2 A_1^2 A_2) e^{j\omega_2 t} \\ &+ \frac{3}{4} k_2 A_1^2 A_2 e^{j((2\omega_1 - \omega_2)t)} \\ &+ \frac{3}{4} k_2 A_1 A_2^2 e^{j((2\omega_2 - \omega_1)t)} \end{aligned} \tag{69}$$

with the out-of-band terms being ignored. Thus, the input contained frequencies ω_1 and ω_2 with the output of the nonlinear system only adding two more frequencies: $2\omega_1 - \omega 2$ and $2\omega_2 - \omega_1$. Further, a three-tone waveform with input frequencies of ω_1, ω_2, and ω_3 will result in nine additional frequencies: $2\omega_1 - \omega_2$, $2\omega_1 - \omega_3$, $2\omega_2 - \omega_1$, $2\omega_2 - \omega_3$, $2\omega_3 - \omega_1$, $2\omega_3 - \omega_2$, $\omega_1 + \omega_2 - \omega_3$, $\omega_1 - \omega_2 + \omega_3$, $-\omega_1 + \omega_2 + \omega_3$. In the case where the number of input frequencies are greater than two, there is a change that some of the IMD products will call at the same frequency as the input

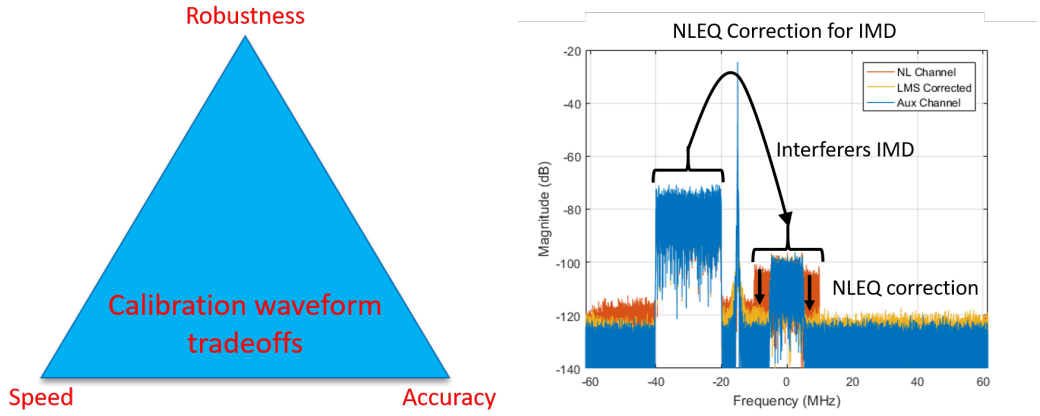

(a) (b)

Figure 18: (a) the typical tradeoffs made when evaluating and choosing the best calibration waveform and (b) an example of the dynamic spectral situations to which the calibration waveform must properly train the NLEQ algorithm to respond (from [81])

siganl or as another IMD. This leads to a loss of orthogonality for the calibration model, making it less effective at generalizing the linearization to any input signal. Therefore, it is ideal to have a calibration waveform where the nonlinear products fall at independent frequencies so that the complex coefficient for that nonlinearity can be simply extracted. This Chapter proposes a general calibration waveform for systems with a large variety of input waveforms, making use of all possible combinations of power and frequency throughout the system.

4.1 Literature Review

Early work on nonlinear system identification – much before the concept of leveraging DSP for lineariztaion – focused on the use of white noise waveforms; however with the increased digitization new waveforms and techniques have been used [89]. One of the first and most important publications on this topic, by Boyd and Chua [89], proposed a multitone (harmonic probing) method. Simply, they proposed a way of constructing a multitone waveform, making use of two relatively prime fre-

quencies, in which no second-order IMD products fall into the same frequency bin or at one of the input tone frequencies. This leads to a waveform that can quickly probe a large bandwidth, while producing IMD products (or tones) that are still easily extracted. Then, Pedro and Carvalho [84] proposed a multisine waveform for behavioral modeling/testing of nonlinear systems. Further, in [23] a bandlimited waveform was proposed for NLEQ calibration in order to train on a wide swath of powers and frequencies. However, the high PAPR of and the fact that IMD at certain frequency are produced from multiple pairs of input frequencies reduce its effectiveness as a generalized calibration waveform.

In the more narrowband sense, two-tones are frequently used for simple nonlinear modeling of systems [145]. Two input tones will then produce two third-order IMD (IM3), two fifth-order IMD (IM5), etc., which makes the waveform good for visualization and quantification (see Figure **??**) of the nonlinearity in a system. Ku and Kenney in [40], [41], [146] used two tones to evaluate many aspects of nonlinear systems. In [146] the authors used two-tone IMD measurements to calculate the error vector magnitude (EVM) of a power amplifier (PA). In [40] the authors, in an well received paper, used two-tones to quantify the memory effects in a PA through changes in the IM3/IM5 magnitudes with respect to the spacing between the two tones. Lastly, in [41] the authors additionally showed that asymmetries between the two IM3 in a two-tone excitation map to the amount of memory effects that are present in the nonlinear system. Pedro and Carvalho, in [145], then showed that, for narrowband memoryless cases, two tones can provide valuable information about a nonlinear system. Two-tones were additionally compared to three tones and bandlimited WGN in [145]. Further, two tones were also used in [77] for NLEQ, evaluating the residual magnitude of the IM3 to determine the optimal number of memory terms in a memory polynomial-based NLEQ.

Linear frequency modulated (LFM) signals (also referred to as chirps), which are typically used for pulse compression in radar systems, have also received some attention for nonlinear system identification. A DPD calibration waveform based on a triangular chirp was proposed in [147]. Their waveform consisted of two segments: the first segment applied the highest spectral power to the middle frequencies, while the second segment amplified the higher frequency components. Additionally, a memory polynomial was used for the DPD model for the nonlinear system, a PA, showing good correction on an orthogonal frequency-division multiplexing (OFDM) waveform using the chrip-based calibration waveform. The same authors, in [148], proposed multiple windowed chirp-based calibration waveforms for DPD of an Long Term Evolution (LTE) transmitter. In this case, the Bartlett-Chirp calibration waveform lead to the best linearization of the PA. Lastly, the initial phase of a chirp for nonlinear identification of a Hammerstein model system was discussed in [149].

4.2 Generalized Calibration Waveform

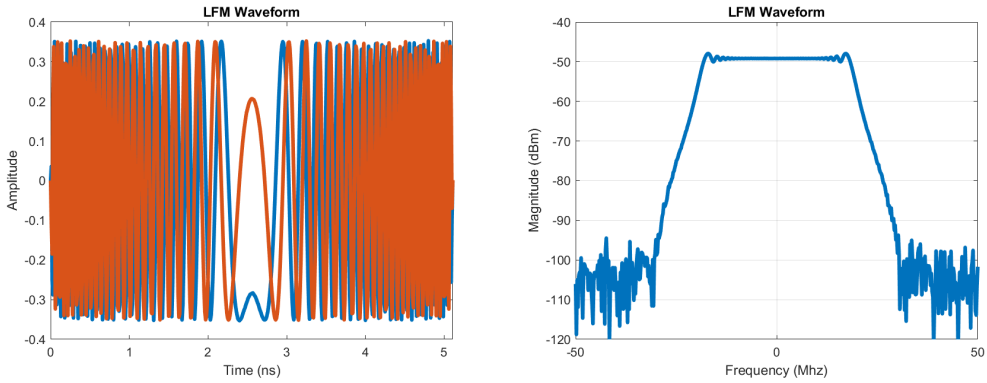

(a) (b)

Figure 19: A simple example of an LFM waveform.

The LFM waveform, shown in Figure 19, has classically been used for pulse-Doppler radars in order to minimize the radar range resolution with a large band-

with, while maintaining a long pulse for maximum transmit power, and is given by [150] as

$$x(t) = A\,\text{rect}(r/T)\ \cos\left(2\pi f_0 t + \pi\alpha t^2\right) \tag{70}$$

with

$$\alpha = \frac{\beta}{\tau}, \tag{71}$$

where τ is the pulsewidth, β is the waveform bandwidth, and f_0 is the starting frequency (e.g. for the 40 MHz waveform shown in Figure 19 at complex baseband, $f_0 = -20$ MHz and $\beta = 40$ MHz). Further, the *time-bandwidth product* is defined as $\beta\tau > 1$. Simplifying to look only at the chirp section of the waveform, given by [142] as

$$x(t) = cos(\pi\frac{\beta}{\tau}t^2) \qquad 0 \leq t \leq \tau \tag{72}$$

and in complex baseband notation

$$x(t) = \exp j\pi\beta t^2/\tau = \exp j\theta(t) \qquad 0 \leq t \leq \tau \tag{73}$$

where

$$\theta(t) = \pi\frac{\beta}{\tau}t^2 = \pi\alpha t^2 \tag{74}$$

from [142], [150]. Lastly, the instantaneous frequency of the LFM is given by [142], [150]

$$F_i(t) = \frac{1}{2\pi}\frac{d\theta(t)}{dt} = \frac{\beta}{\tau}t \qquad \text{Hz}, \tag{75}$$

which shows that at any point in time the LFM is made up of a single frequency, shown in Figure 20, defined by αt Hz. In that sense, in the frequency domain, it is simply probing the environment, or system, similar to a network analyzer, making it a great waveform for wideband calibration. Additionally, another quality that makes the LFM a very suitable waveform for NLEQ and DPD calibration is its low

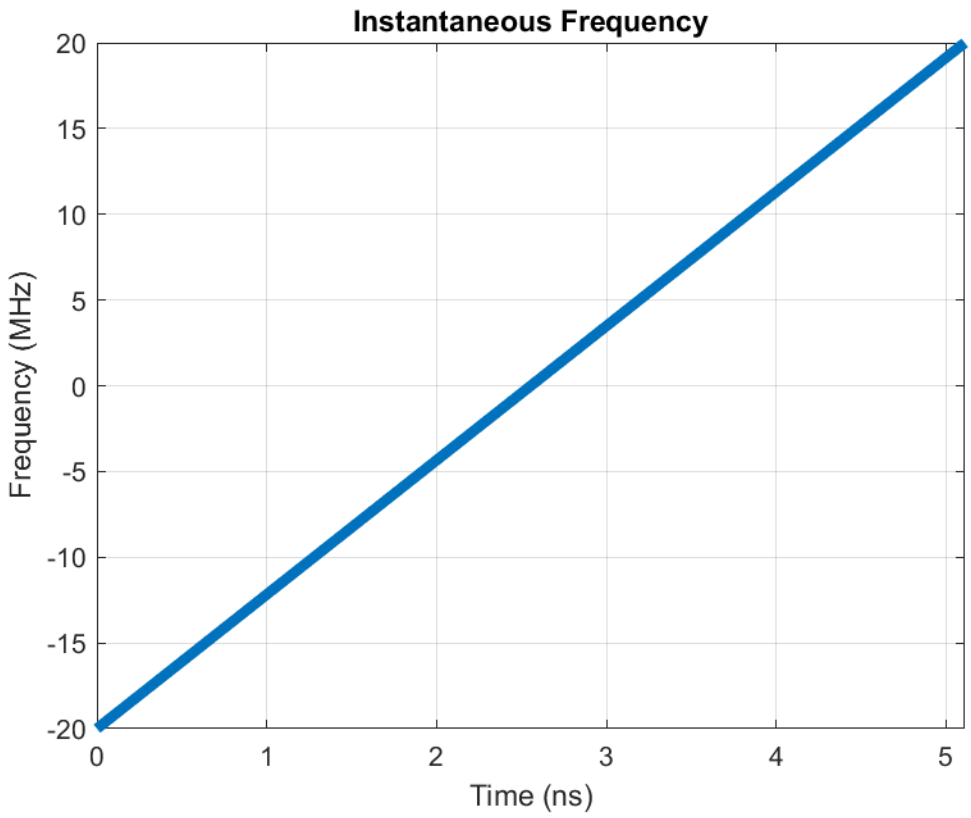

Figure 20: An example of the frequency-step through time for an LFM waveform.

PAPR, which allows it to probe the nonlinearity more often. The PAPR of an LFM can be shown to be approximately 9 dB – the of the waveform is $\frac{1}{2\sqrt{2}}$.

Further, we can see that in a memory-less nonlinear system, a single LFM does suffer from spectral regrowth – this is shown in Figure 21 (b). This is, again, because the LFM is simply a sweep in frequency. However, spectral regrowth will begin to occur once the waveform is introduced into a nonlinear system with memory. This is intuitive as the previous sample, or frequency in the case of an LFM, will affect the proceeding sample/frequency, leading to IMD.

The proposed waveform is the superposition of two LFMs that are offset in frequency; this leads to a waveform that is spectrally similar to sweeping two tones. This takes advantage of the two-tone waveform for linearization since all of the

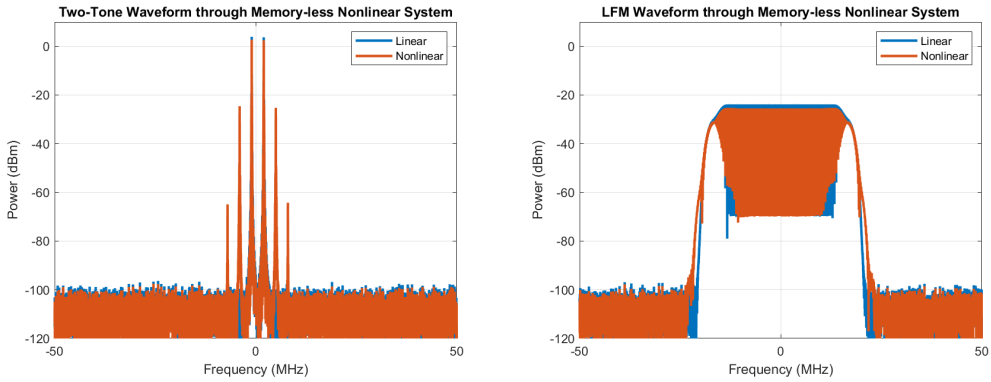

(a) (b)

Figure 21: Results from two different waveforms being passed through a memory-less nonlinear system, with (a) a two-tone waveform, with very low SFDR from the large IM3, and (b) a LFM waveform that is deep into compression, but maintains a high SFDR since none of the frequencies mixed.

frequencies (fundamentals, harmonics, IMD) fall into their own frequency bins. However, the proposed offset-LFM waveform can also occupy a large bandwidth. Additionally, compared to other wideband waveforms, there is minimal spectral regrowth, allowing the waveform to extend closer to the edges of the bandwidth of the system. The frequency offset between the two LFMs – in addition to the nonlinear frequency dependence – will ultimately determine the excess bandwidth beyond the input waveform that makes up spectral regrowth. This is a huge advantage of the offset-LFMs compared to other wideband calibration waveforms as it allows the calibration waveform to probe much closer to the band-edge of the system, shown as a comparison between the two waveforms in Figure 22. From Figure 22 we can see that the offset-LFMs do not suffer from the usual amount of spectral regrowth, which is typically given as $3\times$ the bandwidth for third-order nonlinearities, $5\times$ the bandwidth for fifth-order, etc.

The reader should note that caution needs to be taken when using wideband waveforms and probing close to the band-edge of a nonlinear system if the system suffers from baseband nonlinearities. Baseband nonlinearities from such a, rela-

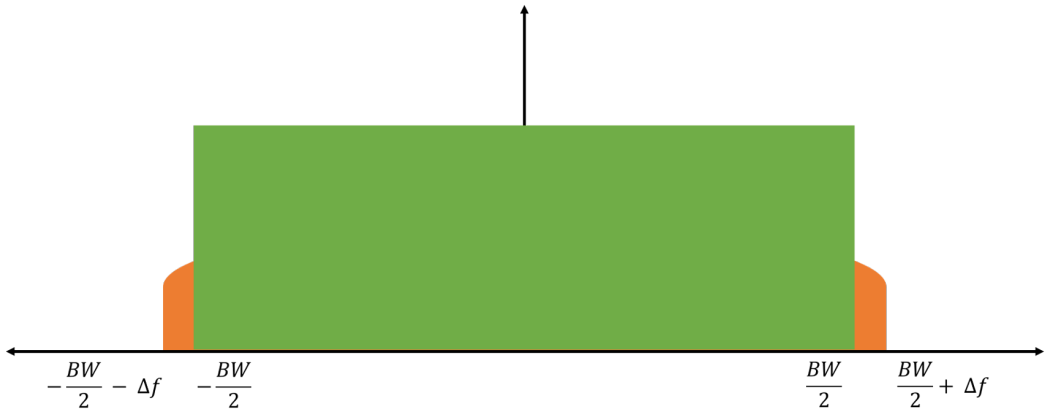

(a)

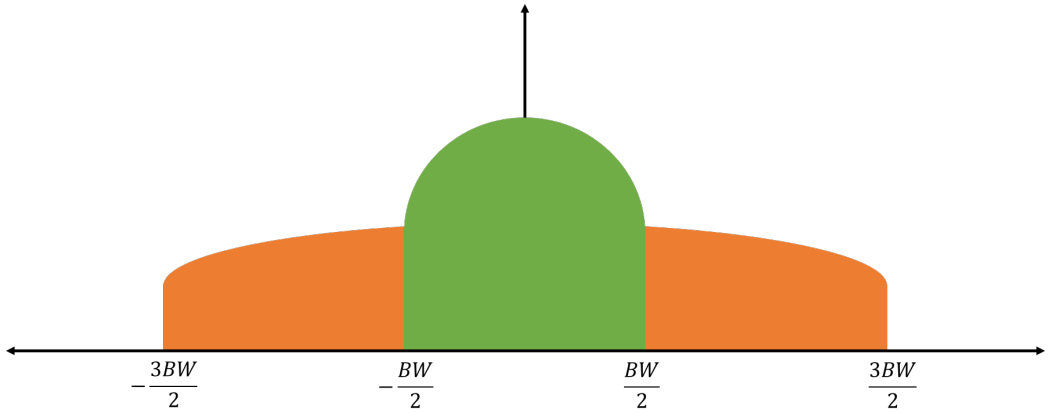

(b)

Figure 22: Comparison of bandwidth efficiency for NLEQ/DPD calibration with (a) the proposed offset LFMs being able to place probing tones near the band-edge, limited by the frequency delta between the two waveforms, while (b) an example of a generic wideband waveform with third-order spectral regrowth of $3BW$.

tively, wideband waveform can create IMD products and harmonics that alias when the are digitized by the ADC. This would obviously lead to a breakdown in the nonlinear modeling abilities. Further, in the case of baseband nonlinearities it could be effective to superpose additional LFMs in order to obtain information about more of the nonlinear Volterra kernels (e.g. $\omega_1 + \omega_2 + \omega_3$).

4.3 Results

Simulations were run in MATLAB to evaluate the performance of the proposed offset-LFM waveform for NLEQ calibration – NLEQ was chosen over DPD since the receiver observes a more dynamic signal environment and, thus, the NLEQ calibration needs to be robust. The nonlinear model used to generate the system nonlinearities was based on a MP from [23], which had five (odd-order) power terms and six delay terms, for a total of thirty coefficients. A bandwidth of 100 MHz was chosen, which is close to the bandwidth of the Analog Devices AD9371 that was used in [23], and 8,192 (2^{13}) samples were used for each waveform. Further, the NLEQ model was also a MP with four power terms (up to seventh order) and eight memory terms. The proposed waveform was constructed of two offset LFMs, one swept from -35 MHz to 32 MHz, while the other went from -32 MHz to 35 MHz – the two LFMs were offset by 3 MHz. Similaryly, fifteen sets of two-tones were taken throughout the bandwidth, to be used for calibration performance testing, (also taking up the bandwidth of -35 MHz to 35 MHz), each set also having a spacing of 3 MHz. Additionally, the two-tone set that was used as a comparison for the proposed waveform was made up of a single tone at -1 MHz and another at 2 MHz. Further, the two calibration waveforms were at the same power.

Initial simulations show very promising results, with the proposed waveform greatly outperforming two-tone training over the bandwidth of the system. Figure 23 shows the two calibration waveforms, with their linear, nonlinear, and NLEQ training spectrum being show. It is evident that the offset-LFMs can probe nearly the entire bandwidth of the system with only a tiny sliver of spectral regrowth, while the two-tone waveform suffers from a greater amount of spectral regrowth since all of the waveform's power is concentrated at two frequencies. The comparison of the calibration performance is then shown in Figure 24. Figure 24 (a) shows when the

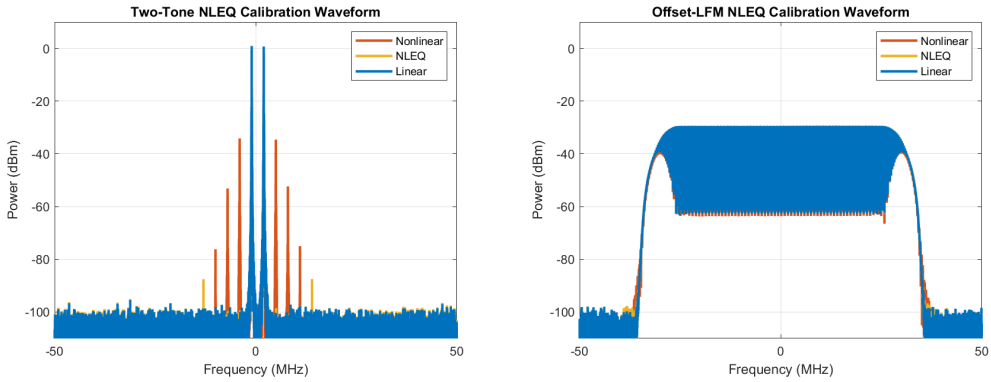

(a) (b)

Figure 23: Two-tone results from AB testing of the (a) two-tone calibration waveform and (b) the proposed two-tone-LFM generalized calibration waveform.

calibration and testing waveforms are at the same power; the two-tone calibration waveform is then identical to the testing waveform, which is why the two-tone calibration outperforms at one point in the center of the band. However, it is quite evident that the calibration performance quickly degrades to a point at the edges of the band where NLEQ begins to "fail", meaning that NLEQ actually begins to lead to a increase in nonlinear spurs. On the other hand, while the proposed waveform's performnance does begin to degrade towards the far edges of the band, it does remain reasonably effective, and at a similar level of effectiveness at that, throughout the majority of the bandwidth of the system. Figure 24 (b) and (c) are similar plots with the testing waveforms being 1 dB and 2 dB lower than the calibration waveforms, respectively. What we can see is that the proposed offset-LFM calibration continues to maintain a high level of NLEQ performance, while the two-tone calibration waveform quickly degrades.

4.4 Conclusion

From these illistrative results, we can see that these initial simulations of the proposed offset-LFM calibration waveform proves very promising at producing a more

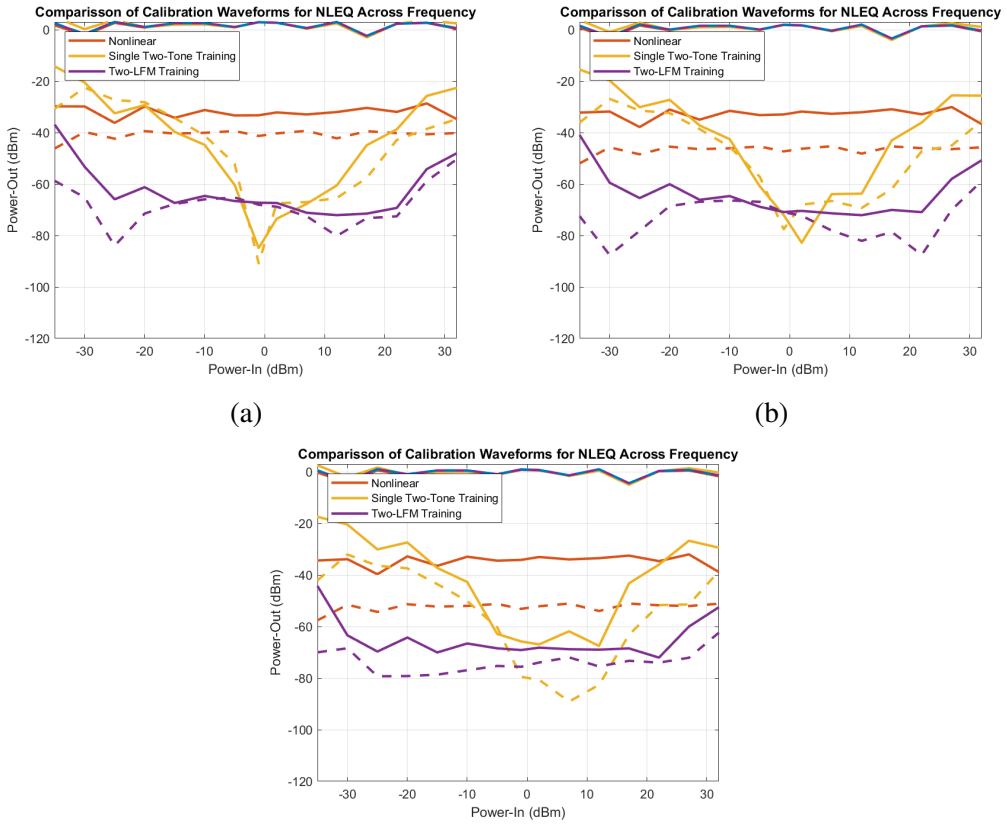

Figure 24: Comparison between a single two-tone training and the proposed offset-LFMs waveform. The dashed lines at the bottom are the fifth-order IMD, while the solid lines at the bottom are the third-order IMD: (a) the results for when the two-tone testing waveforms are at the same power of the training waverforms, (b) the testing waveforms are 1 dB lower in power than the training waveforms, and (c) the testing waveforms are 2 dB lower in power than the training waveforms.

robust calibration waveform for NLEQ and, thus, DPD as well. It is increasinly necessary to have a robust calibration waveform for NLEQ (and DPD) in the increasing spectrally rich environoment, paired with the growing demand for untra-wideband, reconfigureable systems. Future work will include further analysis on the performance of the proposed calibration waveform, along with measurements on a modern digital phased array.

5 Mutual Coupling Calibration of Digital Array Systems

All RF systems, especially phased arrays, need to be calibrated. For phased arrays, the amplitude and phase of each element need to be *aligned* to effectively form a beam in the desired direction, as well as maintain the desired sidelobes and be able to effectively place a null in the direction of an unwanted signal/interferer [11], [12], [151]–[154]. Further, LO offset as well as I/Q-imbalance need to receive some form of calibration to properly modulate and demodulate transmitted and received signals, respectively [12]. The NLEQ and DPD coefficients also need to be calibrated to effectively linearize the system [22]. As previously discussed, the phase, amplitude, LO-offset, I/Q-imbalance, and nonlinearities change over a system's lifetime, as well as with temperature, frequency, etc. [81]. Additionally, the precise element location needs to be accounted for [11]; many modern systems make use of tileable, modular designs that can suffer from unknown gaps between panels – this issue is obviously exacerbated for higher frequencies, such as mmWave, in terms of wavelength – leading to possible inaccuracies in the element locations.

Phased array calibration can be broken down into two general categories: initial calibration and *in situ* calibration. Additionally, in those categories there are two general types of calibration: internal and external [12]. Internal calibration refers to an array *self*-calibrating by using *internal* calibration mechanisms. On the other hand, external calibration refers to the use of equipment that is not a part of the operational array system. One type of these internal mechanisms use RF coupling networks between different Tx and Rx pairs; however, these coupling networks can add large amounts of complexity as well as introduce further unintended errors [153]. Another type of internal calibration mechanism makes use of an additional probe, which can either transmit or receive, or both [155]. Further, a calibration probe can either be embedded into the array panel, attached in front of the array, or

placed on the edges of the array. Some advantages of a calibration probe is that it adds very little complexity, compared to the coupling network, and the probe can calibrate multiple elements, potentially the entire array simultaneously. Further, probe-based calibration can potentially occur during system operation in the case of *in situ* calibration. On the other hand, the calibration probe increases the physical format of the system when extended out in front, while changing the active impedance of the near elements in the array when embedded in the panel. An additional complication is that not every array element will receive the same amount of calibration accuracy since the element distance from the probe will vary across the array panel. A final internal calibration mechanism is to leverage the inherent mutual coupling present in the array. The mutual coupling method requires that the system be an element-level digital transmit-receive system that has individual control of the elements to operate at full-duplex – simultaneous transmit and receive (STAR) [12], [153]. However, if the system meets those requirements, no additional complexity is required for the system. One potential downside of the mutual coupling calibration is the DR requirements. This is especially of concern for phased array radars, which transmit high amounts of power, while receiving very small signals. One solution can be to add a *gainless* path around the Tx PA or Rx LNA, or to add a switchable attenuator on the Tx/Rx chain.

Initial calibration is required once the phased array system has been built, before the system is fielded [152]. Initial calibration will typically use an external calibration method, often in a spectrally quiet environment, such as an anechoic chamber [12], [153]. Process variations and fabrication flaws lead to unknown phases and amplitudes for each element of a phased array. Without knowing these inherent errors, it is impossible to operate the system properly. Further, internal calibration methods are more difficult and do not function well as the phase and amplitude

of the components required for internal calibration are also unknown. Therefore, external calibration is generally required to determine the phase and amplitude of each newly fabricated array element and align the system. Additionally, sometimes it is desired for a system to not require further calibration after the array has been fielded. This requires a large amount of calibration – often manifesting itself in a lookup table (LUT) – over all operational frequencies, temperatures, angles, and more. A great example of initial calibration was done for the Theater High Altitude Area Defense (THAAD) [152], [155], consisting of $25,344$ T/R modules (from 72 subarrays), each with a 6-bit phase shifter and 6-bit attenuator. Additionally, the THAAD employed six reference horns for *in situ* calibration purposes. Initial calibration, described in [152], was accomplished with a planar nearfield scanner, where only eight of the 64 phase shifter states were calibrated. Only calibrating eight of the 64 states was a tradeoff between time and accuracy, incurring an additional error of 0.6 degrees. Further, the distribution of the receiver gains were shown, having a Gaussian-like distribution. Further, after the system was initially calibrated by the nearfield scanner, the six reference horns measured couplings between each horn and each array element, these coupling values are then stored as the "golden standard" calibration [155].

After a system has been fielded, calibration is often required to update the phase and amplitude of each array element [12], [153]. How often these updates occur greatly depend on the operational environment and tolerances of the system. For the *in situ* calibration of a fielded system, it is highly desired to make use of one of the internal calibration methods previously discussed, allowing the system to operate without further intervention [153]. However, one growing area of research for *in situ* calibration is based on the external use of a drone – allowing for the far field calibration of a fielded system. Drone-based calibration is also extremely

useful in updating and re-calibrating legacy systems that may not have many of the aforementioned internal calibration mechanisms.

5.1 In-Situ Calibration Techniques

As mentioned, the THAAD employed six coupling horns used to calibrate the system in teh field. The procedure, described in [155], is to compare the newly measured couplings between the horns and an array element with the golden standard coupling measurements from the initial calibration, and then set the amplitude and phase based on the difference. This ensures that the each element maintains the correct amplitude and phase. Further, this method allows for the replacement of subarray panels without the need for factory calibration. The calibration horns can simply measure the couplings of the elements in the replaced panel and adjust the phase and amplitude accordingly. However, one flaw in the calibration method for the THAAD is that only one single element of the 25,344 elements is calibrated at a time.

An on-chip calibration method was proposed in [156] and was refered to by the authors as built-in-self-test (BIST). The BIST made use of a coupling network which was coupled to all of the antenna ports. They propose that the BIST be calibrated, before being connected to the antennas, with low cost DC and low-frequency probes. Then, after the chip is connected to the antenna, the BIST can update the calibration of the, now, fielded system. Further, they point out that the impedance seen by the BIST will be different for those two situations and needs to be accounted for. Lastly, results were shown for both an X-band and a W-band phased array.

Fulton and Chappell [12] demonstrated the use of mutual coupling calibration for a element-level digital array radar. They used the mutual coupling to calibrate

not only the phase and amplitude of each transmitter and receiver, but also to correct for DC offset and I/Q imbalance. Further, the effectiveness and importance of this *in situ* calibration was demonstrated by increasing the temperature of part of the array. As the temperature increased, the phase and amplitude of the elements began to drift; after an increase of 14° C, one of the transmit elements had drifted in phase by almost 180°. The array was able to re-align the elements by using their proposed mutual coupling calibration. The concept used by Fulton and Chappell is what much of the proposed calibration method in this dissertation is based on. Similarly, another mutual coupling based calibration was proposed in [153]. In their proposed method, first they identify the pairs of elements in the array that should have similar coupling between them (based on geometry, polarization, etc.). Next, equations based on relating the element coupling pairs to each other in each set of similar couplings were formed. Lastly, these equations are put into the complex logarithmic domain in order to form an over-determined matrix equation, which can be solved in the least-square sense. Most recently, Peccarelli and Fulton [22] used mutual coupling to calibrate the NLEQ and DPD coefficients for a digital array. However, the work only presented results for a narrowband, memoryless case, using two tones, with an array of identical elements. The work in [22] is then extended here to a wideband case, training the NLEQ and DPD coefficients across the entire band for a digital array with non-identical elements and frequency dependence.

5.1.1 Mutual Coupling

Mutual coupling (MC) has been used to calibrate the amplitude and phase errors in phased arrays, for both Tx and Rx channels [12]. To the authors' knowledge, the only research that has been conducted in mutual coupling based NLEQ and DPD calibration was demonstrated in [22]. The proposed method is to initially use the

low-power mutual coupling calibration method proposed in [12] to calibrate the phase and gain errors for each element and the mutual coupling between elements. Second, the Rx nonlinearities will be calibrated, ultimately to be used for NLEQ. Lastly, Tx nonlinearities will be calibrated, to be used for DPD.

From [20], [21], we have the $\mathbf{TR}$ matrix, used to represent the effects of coupling, gain, and leakage of the signals between Tx and Rx elements. The matrix is given by

$$\mathbf{TR} = \mathbf{G}^R(\mathbf{I} + \mathbf{L}^R)\mathbf{C}(\mathbf{I} + \mathbf{L}^T)\mathbf{G}^T \tag{76}$$

where $\mathbf{G}^T$ and $\mathbf{G}^R$ are diagonal matrices of the gain of the Tx and Rx channels, respectively, $\mathbf{I}$ is the identity matrix, $\mathbf{L}^T$ and $\mathbf{L}^R$ are the leakage between Tx and Rx, but can be ignored for fully digital arrays with independent channel circuitry, and $\mathbf{C}$ is the coupling matrix. Here it was assumed that the channels were operating in their linear regions by using two separate measurements. In the first state, transmitters were operated at low power and receivers were operated in their normal state, in the second state, transmitters were operated in their normal state and receivers were attenuated. These operational modes were used to measure Rx errors, ignoring the low power Tx errors, and to measure Tx errors, ignoring the attenuated Rx errors. Lastly, the symmetry of the coupling matrix can be used to further estimate the Rx and Tx errors, and the coupling values [12].

5.2 Mutual Coupling for DPD/NLEQ Calibration

Mutual coupling provides a great opportunity for *in-situ* DPD/NLEQ calibration without any need for additional internal or external equipment – however, in the results presented here, a switched RF attenuator is placed in the Rx chain, prior to the nonlinear active components. In this Section we investigate the ability of

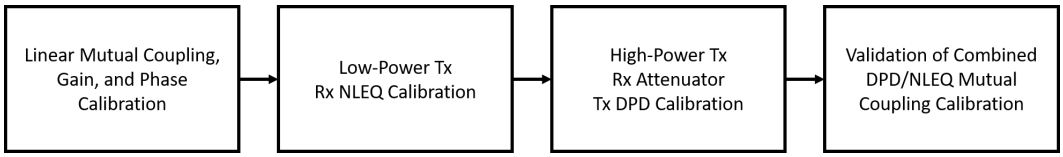

Figure 25: The general proposed mutual coupling calibration procedure.

a system to to leverage the inherent mutual coupling in an array to calibrate both the Rx NLEQ and Tx DPD parameters – essentially to extend the overall SFDR of the entire system and/or improve the system's efficiency. First, linear mutual coupling, as described in Sec. 5.1.1, is used to estimate the couplings between the different Tx and Rx elements, in addition to estimating the Tx and Rx gains, as well as the Tx frequency dependence. Leveraging these estimates, the system can then calibrate the Tx and Rx nonlinearities. First, the method for MC-DPD/NLEQ will be described (conceptually shown in Figure 25 and Figure 26) and then results from MATLAB simulations will be shown. Lastly, an extension of the current simulations will be described.

After linear mutual coupling calibration is used to estimate the gains, couplings, and frequency dependence, the Rx NLEQ coefficients are calibrated, followed by the Tx DPD coefficients. The NLEQ parameters are calibrated before DPD since it is possible to operate the Tx in the low-power linear region, while still coupling over enough power to nearby receivers to drive the Rx LNAs into the nonlinear region. Additionally, since the Tx is operating in the linear region, it is easy to apply the linear Tx frequency dependence that was computed during linear mutual coupling calibration. Digitally removing the Tx frequency dependence allows us to assume that any nonlineary and frequency dependence seen on the receive is from the receiver itself. Now, with the recevied waveform, the estimated Tx and Rx gains, and the estimated coupling values between the different elements, we can estimate a linear version of the received waveform. This estimated linear waveform can be

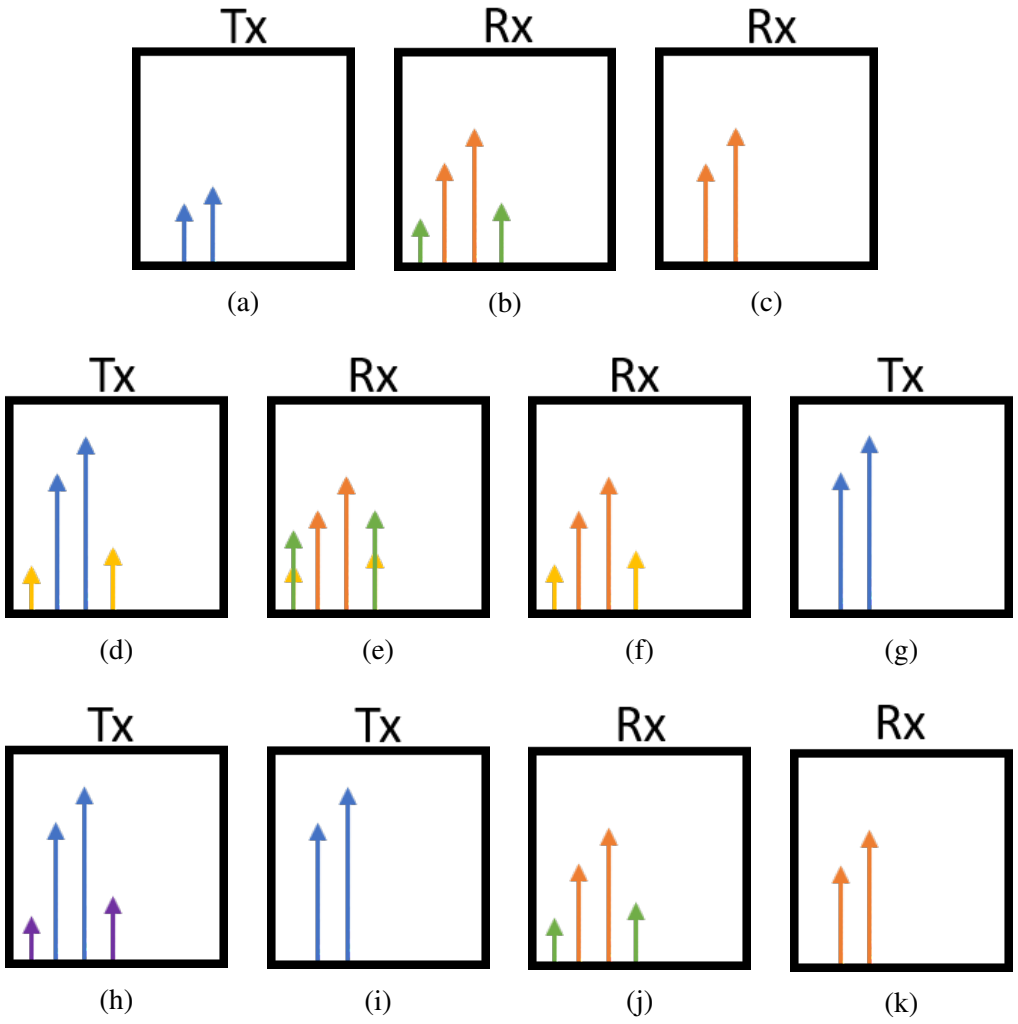

Figure 26: Mutual coupling DPD/NLEQ calibration method, NLEQ calibration: (a) the low-power Tx signals in blue, (b) the Rx signals coupled from the Tx output in orange with their IMD in green, and (c) the Rx signals after NLEQ has been effectively calibrated and applied, removing the spurs. DPD calibration: (d) the high-power Tx signals in blue with their IMD in yellow, (e) the Rx signals coupled from the Tx output in orange with their IMD in green and the Tx IMD shown again in yellow, (f) the Rx signals after NLEQ has been applied, removing the Rx induced spurs, effectively showing the remaining Tx spurs, and (g) the Tx output after DPD has been calibrated from the NLEQ Rx signals. DPD/NLEQ validation: (h) the high-power Tx signals in blue with their DPD IMD in purple, (i) the Tx output, showing an effectively linear spur free signal, (j) the Rx signals coupled from the Tx output in orange with their IMD in green, and (k) the Rx signals after NLEQ has been applied, removing the Rx induced spurs, showing a linear spur free signal.

used along with the received waveform to calibrate the NLEQ coefficients – here this is accomplished using least squares (LS). Next, now that we have calibrated the Rx NLEQ coefficients, we can calibrate the remaining Tx DPD coefficients.

First, the switchable RF attenuator is switched on, helping to attenuate the high-power Tx waveform, preventing the recevier from being completely saturated. Then, the transmitter is operated in its efficient, high-power nonlinear region – note that the Tx frequency dependence correction is not applied here. In order to more accurately estimate only the Tx nonlinearities and frequency dependence, the previously calibrated NLEQ coefficients are used to remove any Rx nonlinearities and frequency dependence. Then, after NLEQ has been applied, we can say that the remaining signal represents the transmitted signal. Similarly to the NLEQ calibration, the estimated Tx and Rx gains and coupling values are used to estimate a linear received signal. The estimated linear signal is then, again, used with the NLEQ corrected signal to estimate the DPD parameters. Now that the NLEQ and DPD coefficients have been calibrated, the corrections can be applied to the Tx and Rx, respectively, to mitigate the nonlinearities of the entire array, extending the effective SFDR of the system.

5.3 Simulations

Simulations of the proposed MC-DPD/NLEQ method were conducted in MATLAB, similarly to those from [22], using a 9×9 digital array of horizontally polarized dipoles, shown in Figure 27. The magnitude of the mutual coupling between the elements is shown in Figure 28, also from [22]; the diagonal with the strongest coupling represents the self-coupling between an element's transmitter and receiver. Further, the array was simulated at a center frequency of 3 GHz, with an element spacing of half-lambda. Additionally, the system had a bandwidth of 100 MHz,

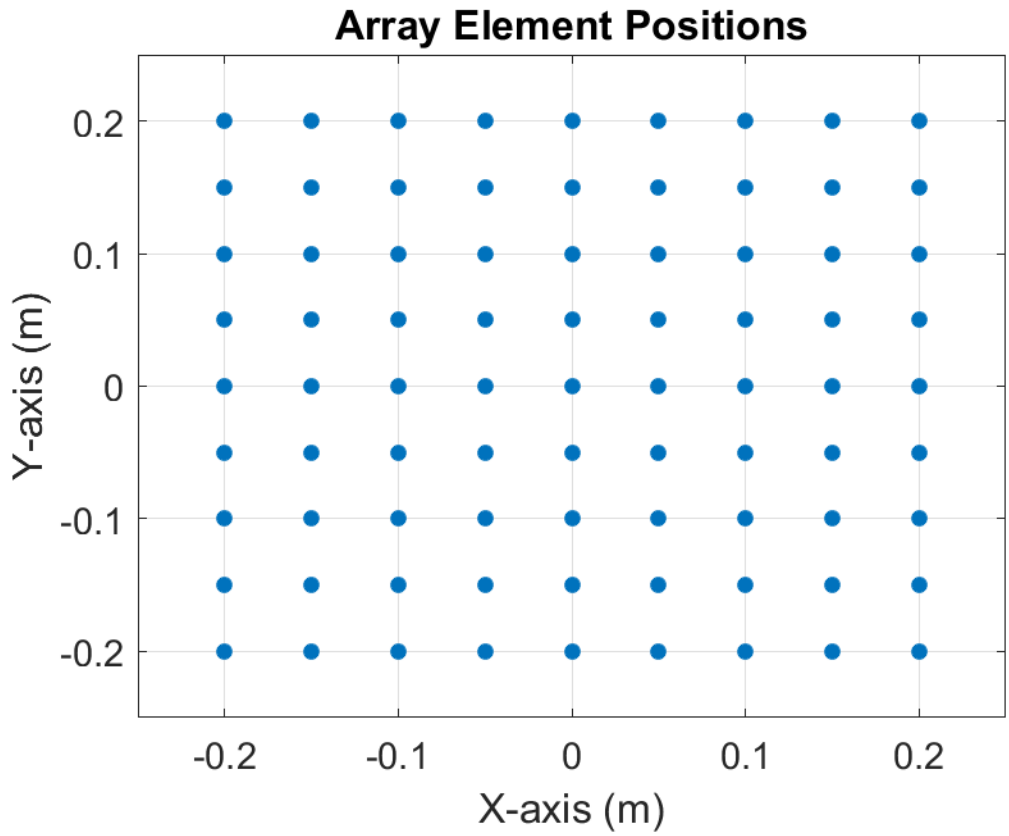

Figure 27: The geometry used for the simulated 9×9 array.

similar to the Analog Devices AD9371, or about a 3.34% fractional bandwidth. An offset-LFM waveform, discussed in the previous Chapter, was used to calibrate both NLEQ and DPD – the length of the waveform in the simulation was 2^{14} samples, or 164μs. The remainder of this Section describes the full simulation setup, as well as the results. First, the frequency dependence of the system, one of the differences from [22], is discussed. Then, the models of the Tx and Rx nonlinearities are defined, similarly to [22]. Lastly, the simulated results are shown and discussed.

5.3.1 Frequency Dependence

Firstly, one of the main differences between this work and the work from [22] is that the simulated array in this Chapter had frequency dependence in the channels, as

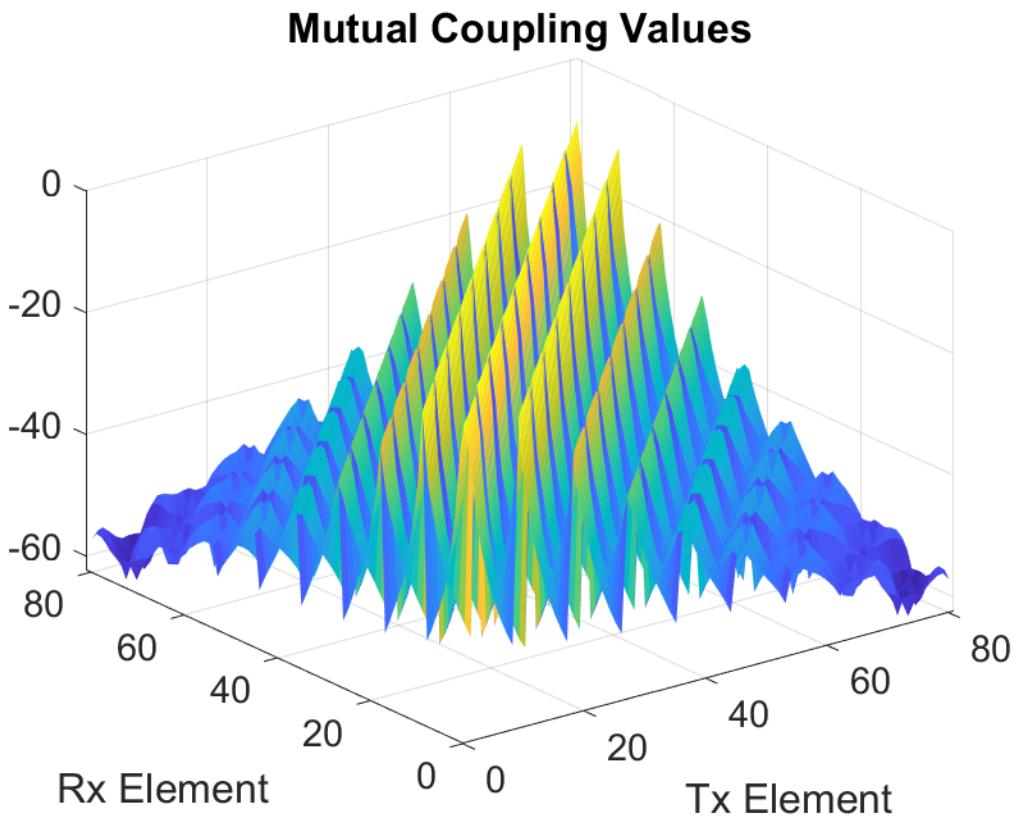

Figure 28: The mutual coupling values between the 81 elements. The diagonal shows self-coupling, which is by far the strongest.

well as performance variations between the elements. This required linear mutual coupling calibration prior to NLEQ/DPD calibration, in order to account for the element variations, as well as frequency dependence. From Chapter 2, we know that the nonlinear models for NLEQ and DPD can account for frequency dependence. However, first we need to be able to separate the frequency dependence of the transmitter from that of the receiver, since the signal during mutual coupling calibration will be affected by both the transmitter and receiver frequency dependencies.

The frequency dependence for both the transmitters and receivers were a simple

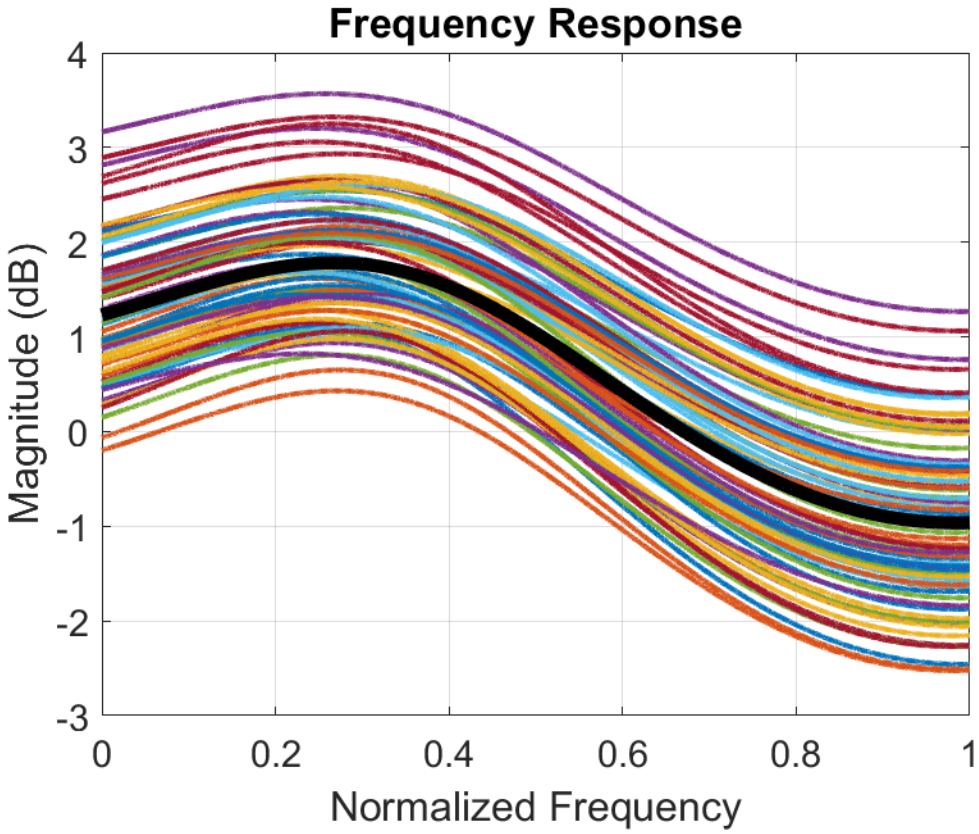

Figure 29: The frequency response of all 81 Tx channels, with the mean response shown in black. The other responses are Normally distributed.

three tap FIR filter, given by

$$h = [0.9 + j0.5, \quad -(0.1 + j0.1), \quad 0.05]. \tag{77}$$

Further, every element was given a slightly different filter in order to represent the inherent performance variation typically present between elements. Both the transmitters and receivers had the same frequency dependence with a Gaussian distribution with a standard deviation of $\sigma = 0.1$. The resulting frequency responses for all 81 transmitters is given by Figure 29, where the black line represents the nominal, mean response.

Now, after the frequency responses of the transmitters and receivers have been

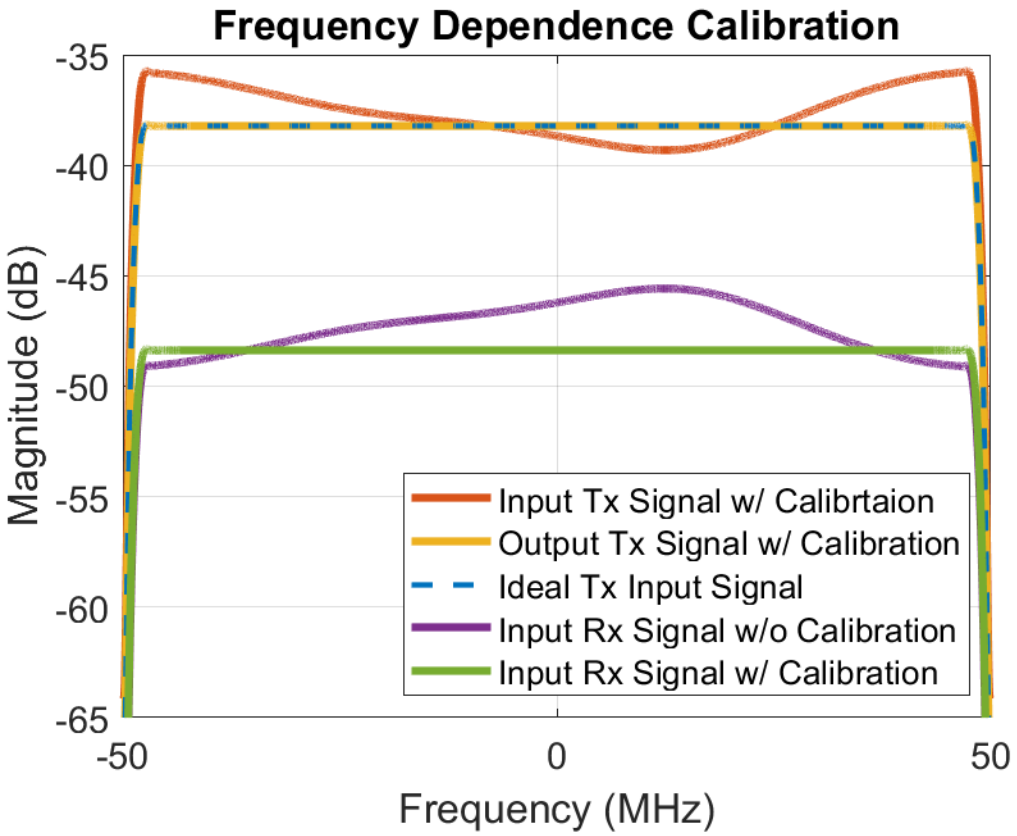

Figure 30: Showing the effectiveness of linear, frequency dependence calibration. Orange shows the digitally compensated waveform, while the ideal linear response is shown in blue. After the calibration waveform passes through the transmitter, the response, in yellow, matches the intended linear signal. Additionally, the purple response is the received waveform prior to calibration. Finally, the green waveform shows that the receiver calibration is also effective at removing the frequency dependence.

constructed, the linear mutual coupling values are determined in a similar fashion to that described in [12]. In this case, a LFM with the bandwidth of the entire system was used to gather the frequency response across the channel, as well as the magnitude response due to the coupling. Figure 30 shows the results of using the calibrated system frequency response (simply the inverse of the frequency response) in order to linearize the system across frequency, allowing the elements to be of equal phase an magnitude across the entire bandwidth. Further, Figure 31 shows

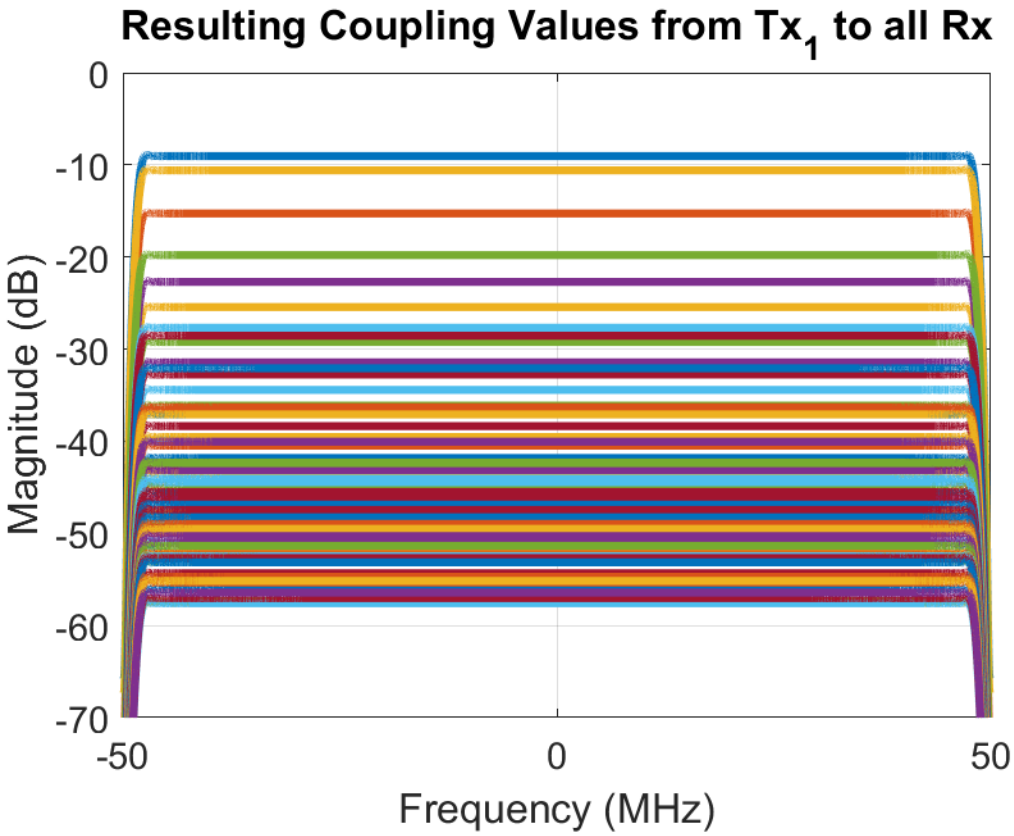

Figure 31: The resulting coupling values from the first transmitter to the 81 receivers, obtained from linear calibration.

the resulting coupling values gathered during this golden standard process, a similar concept to that which was discussed in detail in [12], [155].

5.3.2 Nonlinearities

Similarly to the methods used in [22], the nonlinear models for the transmitter and receiver were static nonlinearities. This, paired with the preceding frequency dependence yields a Wiener system, as was discussed in Chapter 2. The transmitters were made up of a seventh-order static nonlinearity with a gain of 30 dB and a 1-dB compression point of 30 dBm. This was put into an in-house MATLAB function and an odd-order polynomial was output, representing the memoryless nonlineari-

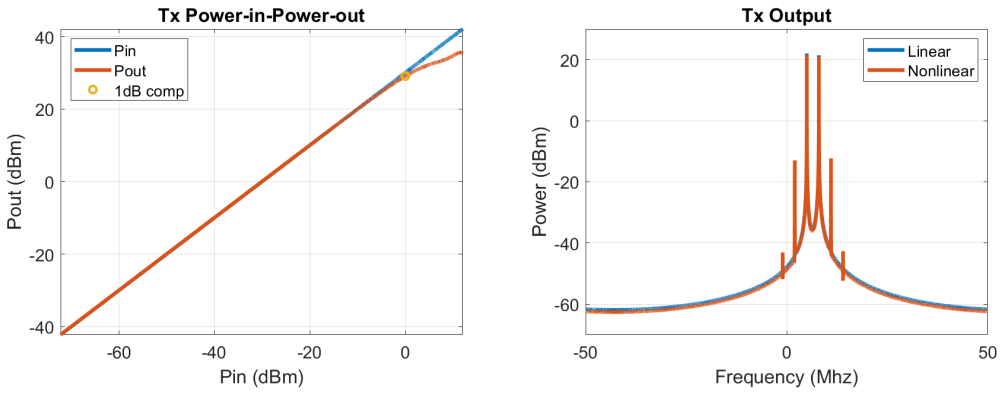

(a) (b)

Figure 32: (a) the input-power vs output-power plot for the transmitters and (b) an example of the nonlinearities produced by the transmitter's nonlinear model.

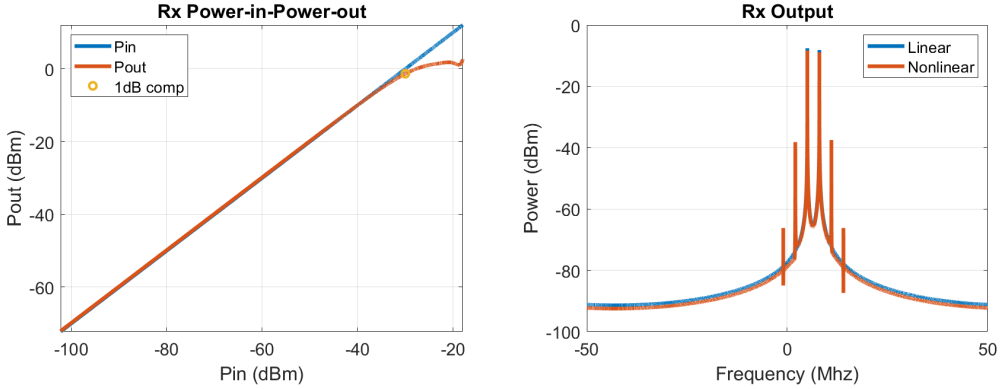

(a) (b)

Figure 33: (a) the input-power vs output-power plot for the receivers and (b) an example of the nonlinearities produced by the receiver's nonlinear model.

ties of the Tx channel. The input-output power curve of the Tx channel's nonlinear response is shown in Figure 32a. Additionally, an example of the nonlinear response from a two-tone stimulus is given in Figure 32b.

On the other hand, the receivers were modeled with a gain of 30 dB and a 1-dB compression point of 0 dBm. The static nonlinearity was produced by the same in-house MATLAB function, producing an odd-order nonlinear system represented by Figure 33a. Additionally, Figure 33b gives an example of the output of the nonlinear system with a two-tone stimulus.

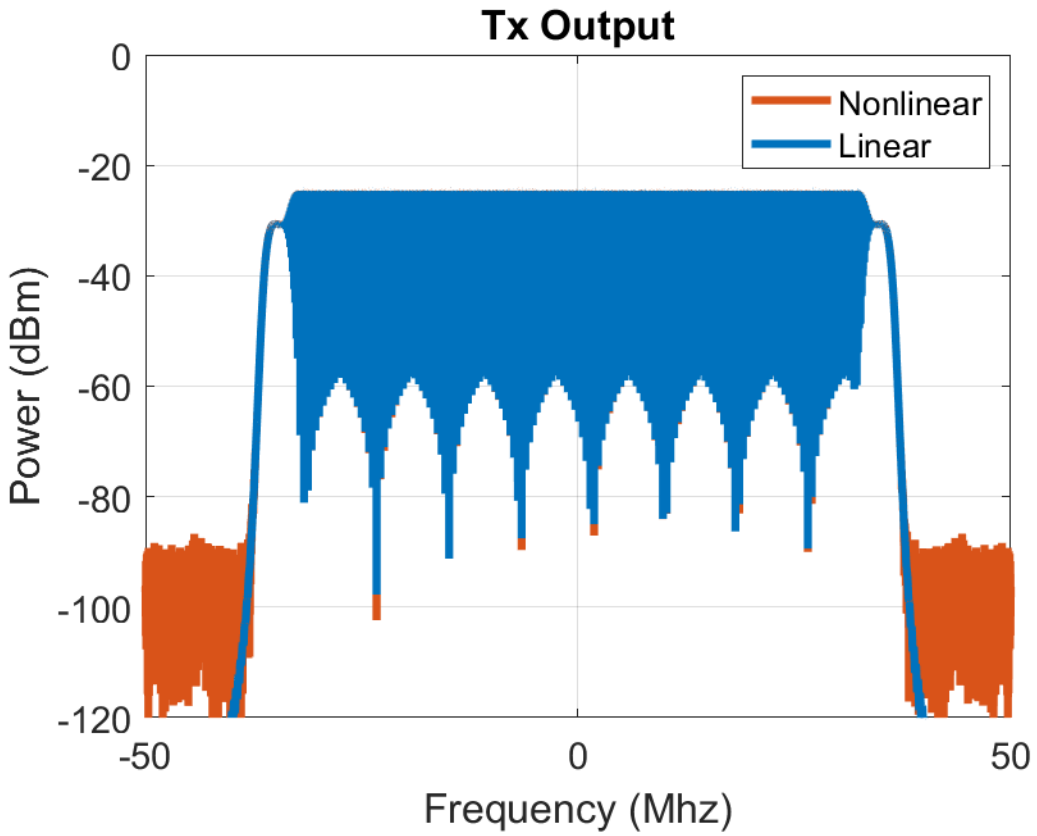

Figure 34: Offset-LFM output from the first transmitter, operating in its linear low-power region, showing an output that well matches the expedted linear output.

5.3.3 Receiver NLEQ Calibration

Now that the digital array's transmitters and receivers have been defined, the calibration simulation can be conducted. First, NLEQ for the receivers is calibrated. The reason why the receivers are calibrated prior to the transmitters is because we know that we can operate the transmitters in a low-power linear region, which will still drive the sensitive receivers into compression. Additionally, given the frequency response calibration that was previously conducted, we can transmit a signal without frequency dependence by applying the inverse of the frequency response digitally, prior to sending the waveform through the system. The waveform that was used was the offset-LFM waveform proposed in Chapter 4 in order to ef-

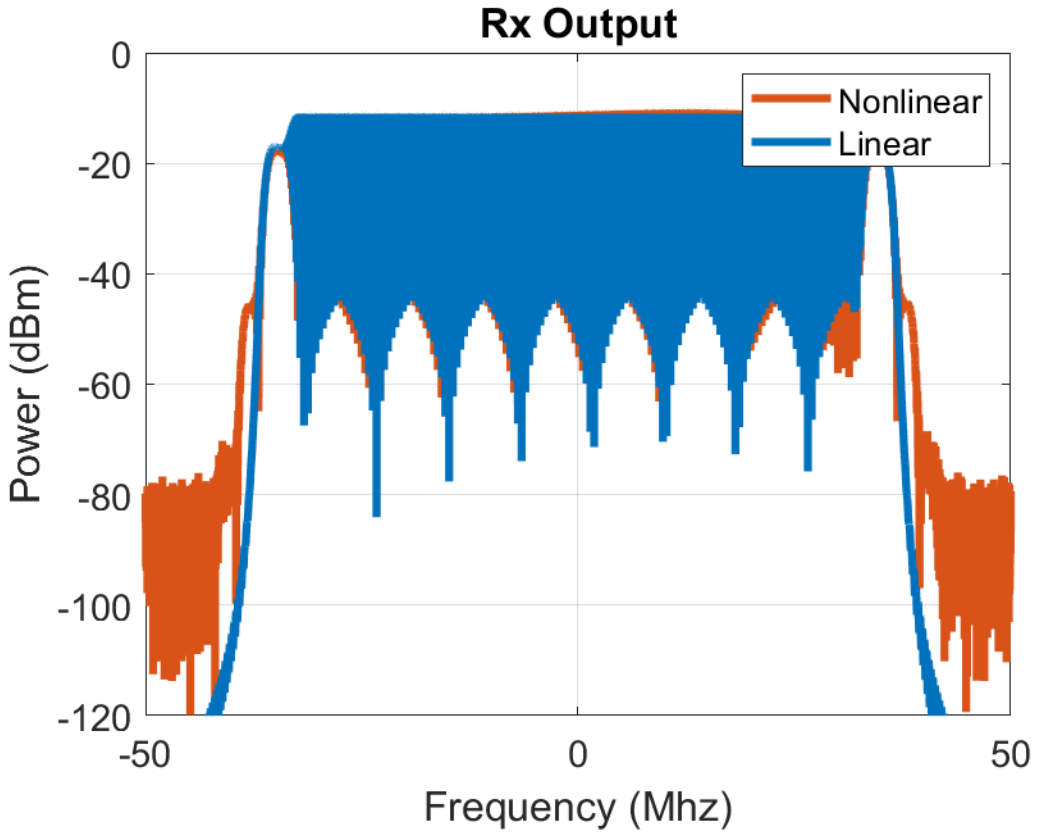

Figure 35: The received offset-LFM coupled over from the adjacent transmitter. There is noticeable effect from frequency dependence in the main band of the waveform. Additionally, third- and fifth-order spurs are showing some spectral regrowth at the edges of the waveform.

fectively calibrate the entire bandwidth and correct for the frequency dependence. The goal will be to encapsulate the nonlinearities as well as the memory effects into the NLEQ (and DPD) coefficients to minimize the equalization steps required in signal processing.

The first transmitter transmited an offset-LFM with a power of -24 dBm with a bandwidth of 74 MHz, with an offset of 3 MHz between the two LFMs. For simplicity, here we use the adjacent transmitter to calibrate the receiver. Figure 34 shows that the waveform that is being transmitted is at -24 dBm and operating linearity, as expected. Then, Figure 35 shows that the receiver is beginning to oper-

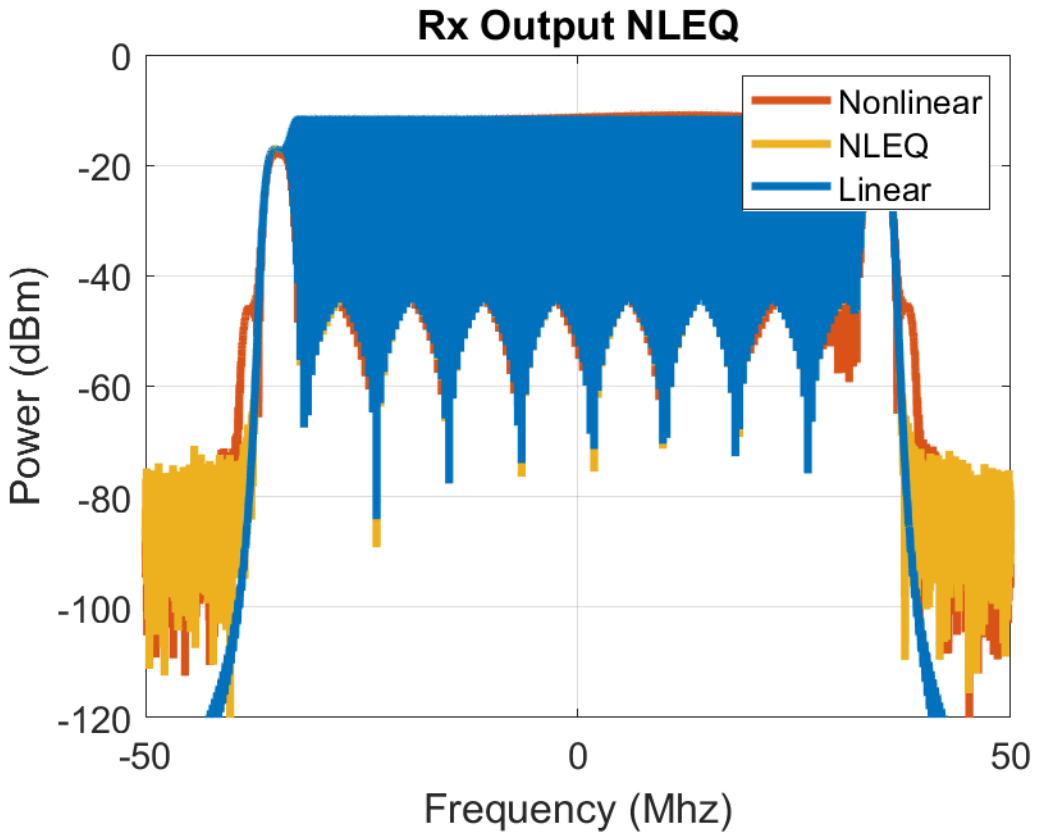

Figure 36: The NLEQ training results, in yellow, show a good reduction in the nonlinear spectral regrowth, in addition to a mitigation of the strong frequency dependence.

ate nonlinearly with IM3 more than 30 dB above the noise floor. Additionally, we can see effects from the frequency dependence with the wave/lump in the nonlinear plot.

Then, since we have the received nonlinear signal, and we know which signal we transmitted along with the coupling between the transmitter and receiver, we can train NLEQ. The NLEQ model was a memory polynomial – it is expected that this will generalize well to the system's Wiener nonlinearity. In this case, NLEQ required an order of eleven (six power terms) and a delay of fifteen. The bandwidth generalization as well as the dynamic range requirements required a large model in order to meet the performance requirements. Figure 36 shows the results, mitigating

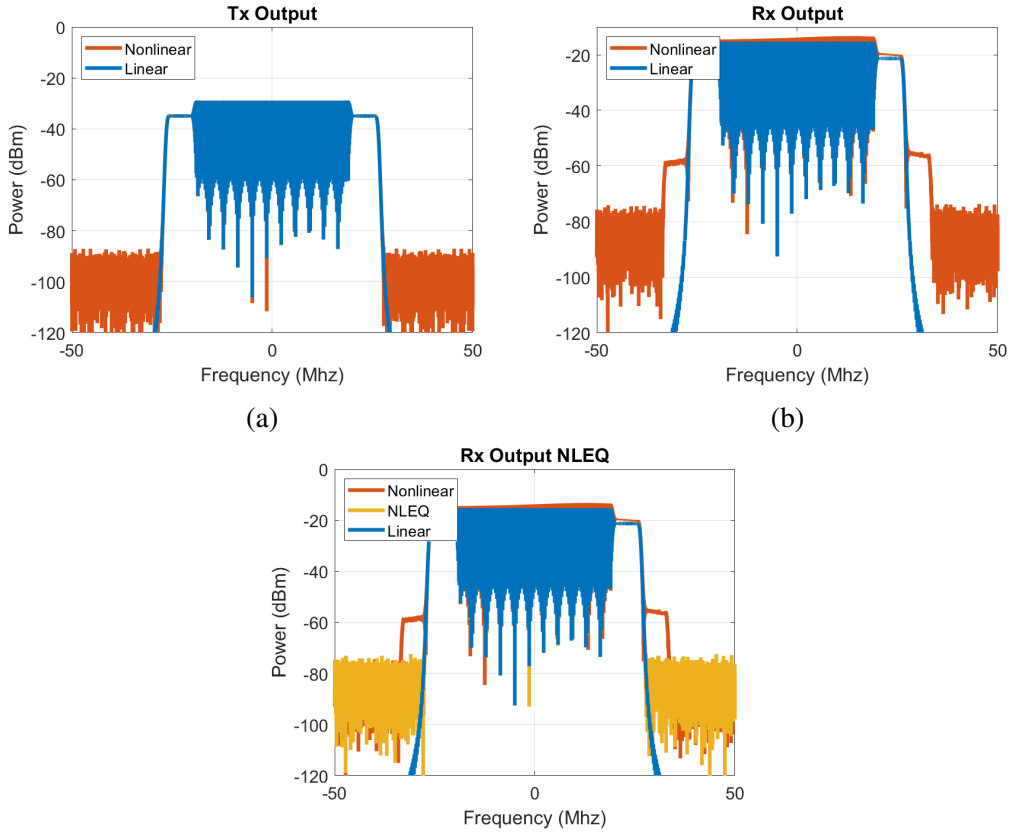

Figure 37: (a) the Tx output for NLEQ validation; shows the transmitter is operating linearly, (b) the Rx output, showing a significant amount of nonlinear spectral regrowth in addition to the strong frequency dependence evident in the main bandwidth of the waveform, and (c) the NLEQ corrected waveform (in yellow) has effectively mitigated the spectral regrowth and frequency dependence with the previously calibrated NLEQ coefficients.

the IM3 by more than 20 dB, as well as removing the strong frequency dependence.

Then, in order to confirm that the NLEQ coefficients are well generalized and functioning properly, we validate using a different waveform bandwidth, power, and frequency spacing. The power was reduced to -30 dBm and the bandwidth reduced to 54 MHz. Additionally, the LFM offset was increased to 7 MHz. Figure 37a shows that the transmitter, as expected, is operating linearly. Figure 37b shows that the receiver is operating in the nonlinear region, and suffering greatly from frequency dependence, with IM3 about 20 dB above the noise floor and a few

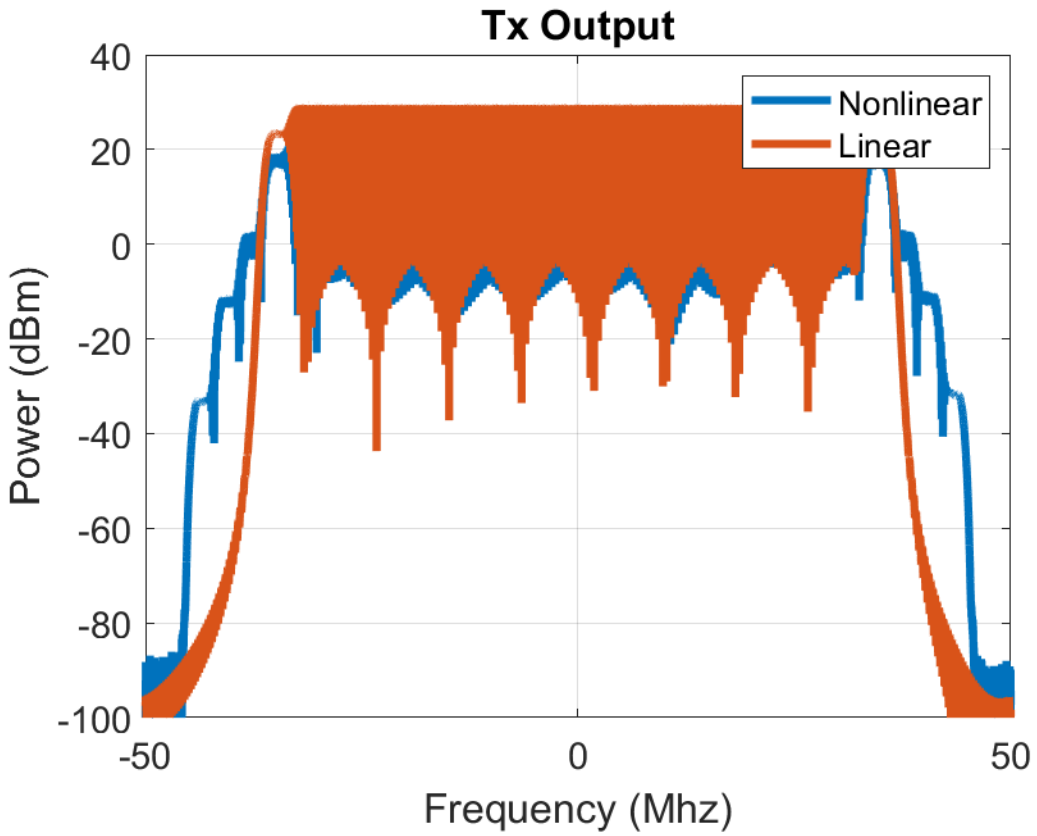

Figure 38: The Tx output for the DPD calibration. The output waveform shows a significant amount of spectral regrowth with the system being operated deep into its nonlinear region.

dB of frequency effects in the main bandwidth of the waveform. Lastly, Figure 37c shows the results from using the previously calibrated NLEQ coefficients on this new received waveform. The nonlinearities have been completely removed, both the power nonlinearities as well as the frequency dependence. This demonstrates good results for the overall generality and effectiveness of the mutual coupling calibrated NLEQ coefficients using the offset-LFM waveform.

5.3.4 Transmitter DPD Calibration

After the receivers have all be calibrated with NLEQ, the transmitters can then be calibrated with DPD. In a similar fashion to [22], a 70 dB attenuator on the Rx

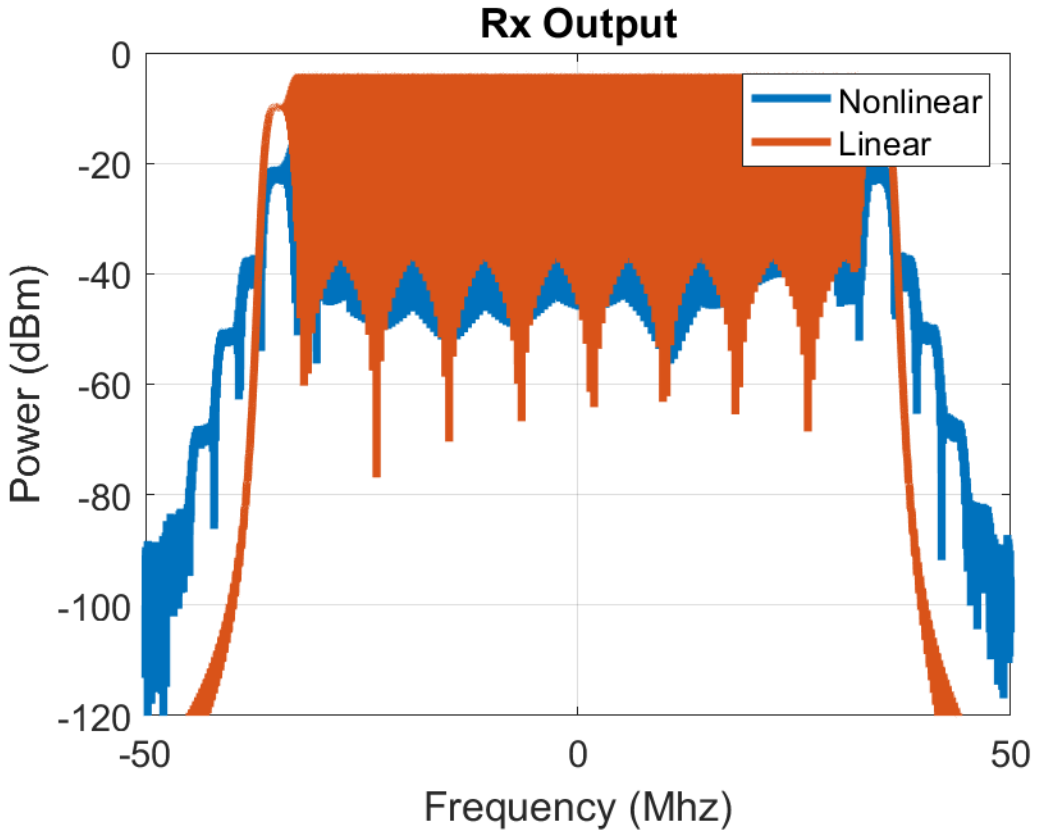

Figure 39: The received waveform, after being attenuated with the switched RF attenuator. There is further a further addition of nonlinearities by the Rx chain.

channels, placed before any active components, is switched into the RF signal path in order to not completely saturate the receivers while operating the transmitters in their high power, nonlinear region. Additionally, it should be noted that a weaker attenuator, or no attenuator at all, could be used if using receivers far away from the transmitting element; however, here we use the adjacent element. One of the reasons for doing this is to guarantee that the transmitter is not saturating any elements in the array. This is something important to note as driving active components deep into their nonlinear region (saturation) can change the input impedance, and thus, the input impedance of the antenna element and its coupling with other elements in the array. This situation could lead to an inaccurate or less effective calibration.

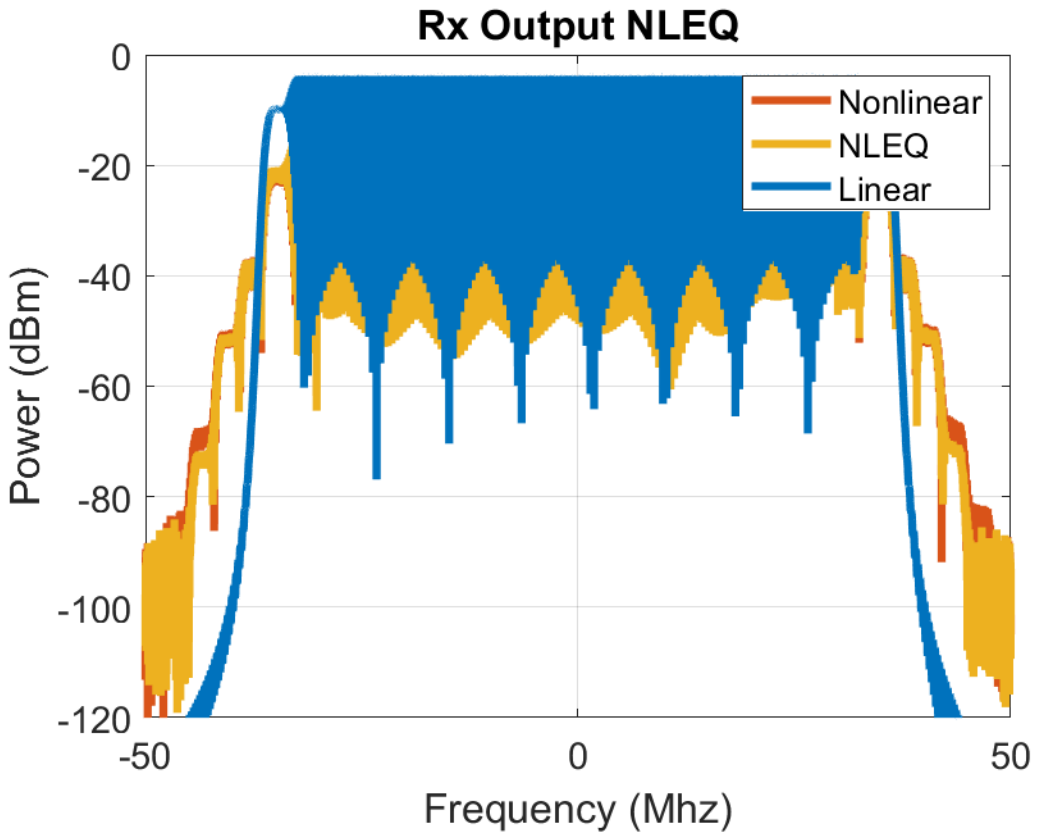

Figure 40: NLEQ, in yellow, having mitigated the Rx nonlinearities and frequency dependence, leaving only the nonlinearities and frequency dependence induced by the Tx chain.

The receivers have been calibrated for NLEQ, including their memory effects; therefore, we also want to calibrate the transmitters with DPD that includes the Tx memory effects. During the Tx DPD calibration the frequency dependence calibration is not applied – recall that it was applied during the Rx NLEQ calibration. Using the same offset-LFM waveform from the NLEQ calibration with a power of 30 dBm, the Tx elements can be calibrated. The DPD coefficients used a memory polynomial model, similar to NLEQ, with an order of 15 (eight power terms) and a delay of 13 in order to effectively capture the high-power nonlinearities. Figure 38 shows that the transmitter is operating deep into its nonlinear region.

Then, Figure 39 shows the received signal from the adjacent element, adding

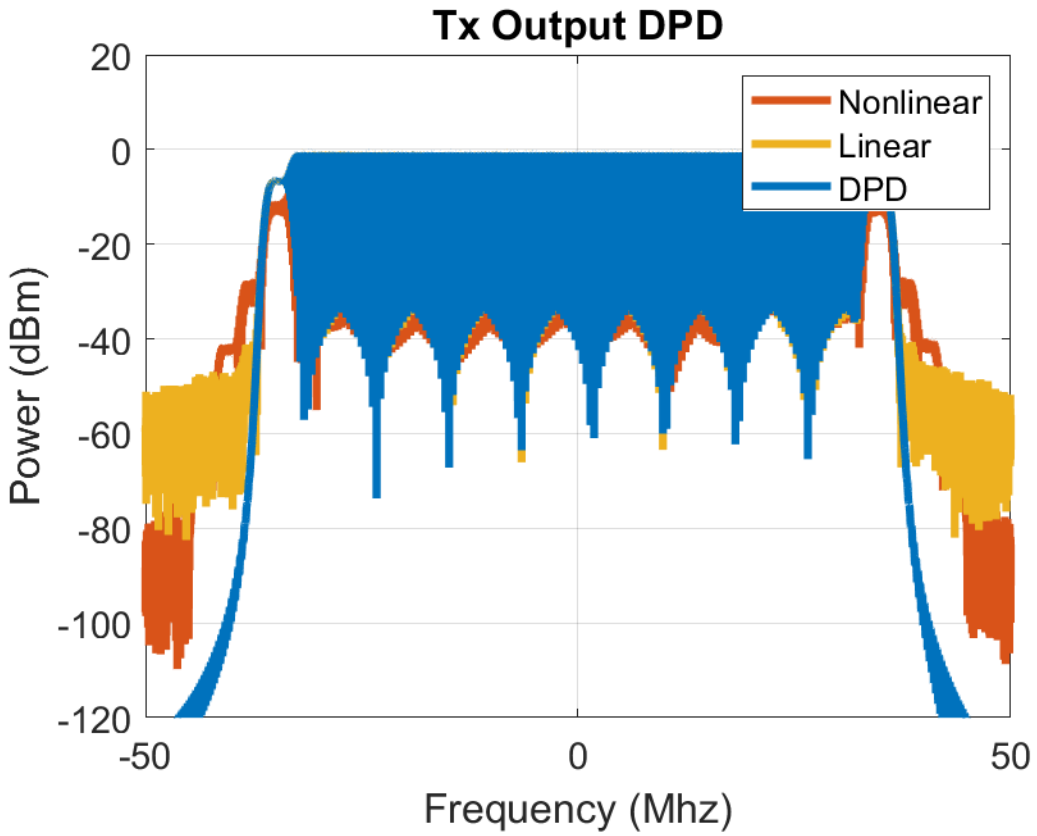

Figure 41: The DPD trained waveform, in yellow, showing good mitigation of the Tx nonlinearities.

some additional nonlinear impairments. Applying the previously calibrated NLEQ coefficients helps to remove the receiver-induced nonlinearities, leaving only the Tx nonlinearities, shown in Figure 40, that need to be removed with the DPD calibration. Recall, this ability is the reason that NLEQ is calibrated prior to DPD. Now what remains is the approximated transmitted signal, and given the linear signal that we expected to receive, we can calibrate the DPD coefficients. Lastly, Figure 41 shows the resulting receiver-side DPD calibration, mitigating the IM3 by more than 10 dB and removing the Tx frequency dependence. Note that even though the 10 dB of mitigation does not seem very effective, the Tx training waveform was operated far into compression, much further than is typically done during operation.

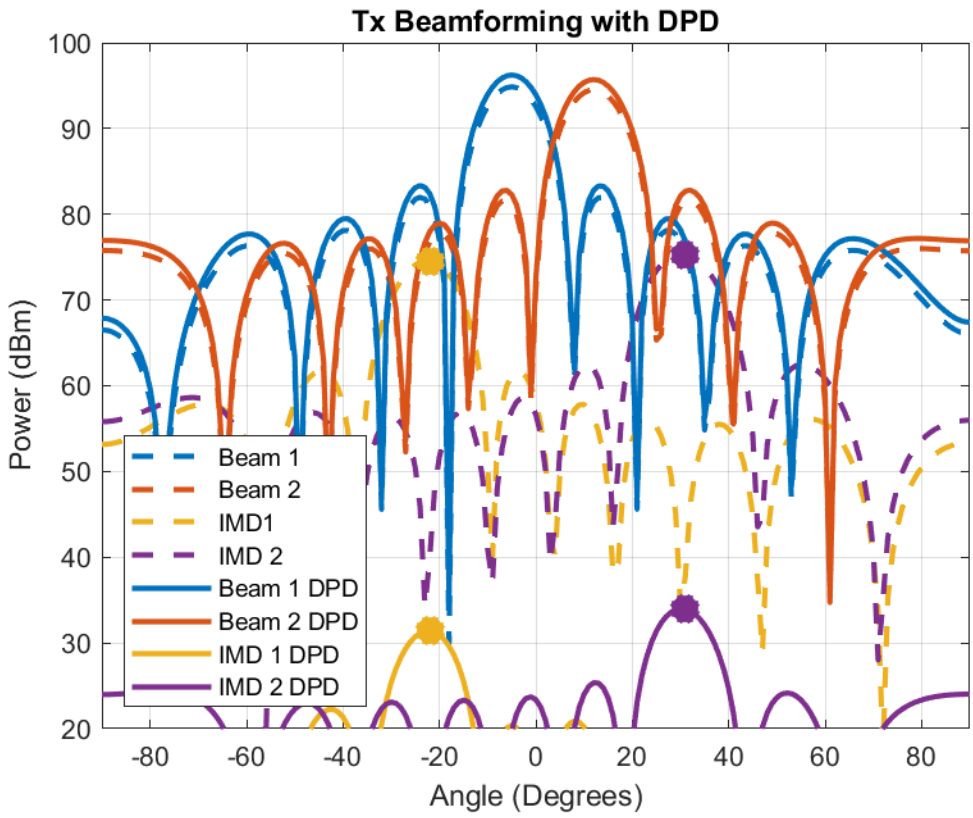

Figure 42: The Tx beamforming results from an input of two CW tones and their IM3 products. The calibrated DPD coefficients were also applied, mitigating the IM3 beams by more than 40 dB.

This was done in order to grantee that the entire dynamic range of the transmitter was calibrated.

5.3.5 Tx Beamforming with DPD

After the entire array has been calibrated for NLEQ and DPD, it is useful to look at the effect at the array-level. This is easily done through beamforming two CW signals from different directions; in this case a 5 MHz (baseband) tone coming from -5° in azimuth and a 8 MHz tone coming from 12° in azimuth. Recall that, from Hemmi [36], it is straightforward to determine the *direction* of the IM3; in this case at -22° and 31°. Without DPD this results in IM3 that are less than 20 dB below

the main signals. On the other hand, with DPD the IM3 mitigated by more than 40 dB, resulting in a much cleaner spatio-spectral output. Lastly, since the wideband, offset-LFM was used, these results are valid across the system bandwidth.

5.4 Conclusion

This Chapter demonstrated an effective wideband, *in situ* calibration technique for NLEQ and DPD for a digital array. The calibration provided one set of coefficients, for each Tx and Rx, to correct the inherent phase and amplitude errors across the array, across frequency, as well as correct the nonlinearities of the array. Simulated results showed that the proposed calibration method provides an elegant solution to maintaining a calibrated and linear digital array system while in the field. Additionally, the beamformed results showed a large increase in the spatio-spectral dynamic range of the system.

6 Conclusion and Future Work

In conclusion, digital array dynamic range, ultimately defining the system's performance, is typically limited by the correlation of unwanted spurious products. These spurs were shown to have come the nonlinearities in the system; such as amplifier or mixer nonlinearities. Additionally, methods for mitigating and decorrelating these spurs were shown. LO decorrelation techniques were shown to be effective for eliminating mixer nonlinearities as well as baseband even-order spurs and harmonics. Then, to remove the odd-order spurs, NLEQ for receive and DPD for transmit were shown to be very effective at linearizing a nonlinear system. However, one common issue is the difficulty with calibrating these linearization techniques.

The main contributions of this dissertation are the proposed offset-LFM for NLEQ and DPD calibration. The proposed waveform was shown to generalize across the entire bandwidth of the system as well as at multiple different power levels. This calibration waveform helps nonlinear systems to effectively extend their SFDR in modern spectrally-dynamic environments. The other main contribution of this dissertation lies in the mutual coupling-based calibration for NLEQ and DPD. This calibration technique, here leveraging the proposed calibration waveform, was shown to effectively calibrate the NLEQ and DPD coefficients for a fielded system; additionally taking into account the frequency dependence of the system as well as the variations between elements. Lastly, the combined mutual coupling method with the proposed calibration waveform effectively mitigated spurious beams in the array on transmit, helping the system perform in a more efficient and linear fashion.

Future work will consist of taking the measurements, using the proposed calibration waveform, in a real digital array to test the accuracy of the training waveform. Further, to test the proposed calibration waveform's resistance to changes in temperature/voltage compared to other potential calibration waveforms. Addi-

tionally, to test the proposed mutual coupling calibration for NLEQ and DPD on a modern fully-digital array. These measurements will then help to adjust for different dynamic range considerations, as well as the reality of a superfluous number of potential coupling signals to account for.

References

[1] C. Fulton, P. Clough, V. Pai, and W. Chappell, "A digital array radar with a hierarchical system architecture," in *IEEE MTT-S International Microwave Symposium Digest*, Jun. 2009.

[2] A. Hakkarainen, J. Werner, K. R. Dandekar, and M. Valkama, "Widely-linear beamforming and RF impairment suppression in massive antenna array," *Journal of Communications and Networks*, vol. 15, pp. 383–397, 4 Aug. 2013.

[3] L. Paulsen, T. Hoffmann, C. Fulton, M. Yeary, A. Saunders, D. Thompson, B. Chen, A. Guo, and B. Murmann, "Impact: A low cost, reconfigurable, digital beamforming common module building block for next generation phased arrays," *Proc. SPIE 9479, Open Architecture/Open Business Model Net-Centric Systems and Defense Transformation 2015*, vol. 9479, May 2015.

[4] B. James and C. Fulton, "Decorrelation and mitigation of spurious products in phased arrays with direct conversion transceivers," *Proc. 2015 IEEE MTT-S International Microwave Symposium*, pp. 1–3, May 2015.

[5] M. Fozooni, M. Matthaiou, E. Bjornson, and T. Q. Duong, "Performance limits of mimo systems with nonlinear power amplifiers," in *Proc. IEEE Global Communications Conference (GLOBECOM)*, Dec. 2015.

[6] E. G. Larsson, O. Edfors, F. Tufvesson, and T. L. Marzetta, "Massive MIMO for next generation wireless systems," *Proc. IEEE Communications Magazine*, vol. 52, 2 Feb. 2014.

[7] S. H. Talisa, K. W. O'Haver, T. M. Comberiate, M. D. Sharp, and O. F. Somerlock, "Benefits of digital phased array radar," *Proc. IEEE*, vol. 104, no. 3, pp. 530–543, Mar. 2016.

[8] C. Fulton, M. Yeary, D. Thompson, J. Lake, and A. Mitchell, "Digital phased arrays: Challenges and opportunities," *Proc. IEEE*, vol. 104, no. 3, pp. 487–503, Mar. 2016.

[9] A. Puglielli, A. Townley, G. LaCaille, V. Milovanovic, P. Lu, K. Trotskovsky, A. Whitecombr, N. Narevsky, G. Wright, T. Courtade, E. Alon, B. Nikolic, and A. M. Niknejad, "Design of energy- and cost-efficient massive MIMO arrays," *Proc. IEEE*, vol. 104, 3 Mar. 2016.

[10] J. S. Herd and M. D. Conway, "The evolution to modern phased array architectures," *Proc. IEEE*, vol. 104, 3 Mar. 2016.

[11] W. Chen, Q. Yin, and A. Feng, "Array calibration for compensating gain/phase mismatch and mutual coupling effects in smart antenna systems," in *2008 IEEE International Symposium on Wireless Communication Systems*, Oct. 2008.

[12] C. Fulton and W. Chappell, "Calibration techniques for digital phased arrays," in *IEEE International Conference on Microwaves, Communications, Antennas and Electronics Systems, 2009. COMCAS 2009*, Nov. 2009.

[13] Y. Vasavada and J. H. Reed, "Amplitude and phase calibration of antenna arrays," in *IEEE MTT-S International Microwave and RF Conference (IMaRF)*, Dec. 2017.

[14] N. Peccarelli, "A least mean-square approach to nonlinear equalization of digital array receivers," Master's thesis, University of Oklahoma, Norman, Oklahoma, May 2018.

[15] H. Krishnaswamy and L. Zhang, "Analog and RF interference mitigation for integrated MIMO receiver arrays," *Proc. IEEE*, vol. 104, 3 Mar. 2016.

[16] *Advanced Air Interface, Mobile WiMax*. IEEE 802.16m, 2011.

[17] S. A. Bassam, M. Helaoui, and F. M. Ghannouchi, "Crossover digital predistorter for the compensation of crosstalk and nonlinearity in MIMO transmitters," *IEEE Trans. Microwave Theory and Techniques*, vol. 57, pp. 1119–1128, 5 May 2009.

[18] *Standard for Information Technology — Local and Metropolitan Area Networks — Specific Requirements — Part 11: Wireless LAN Medium Access Control (MAC) and Physical Layer (PHY) Specifications*. IEEE 802.11n, 2009.

[19] *Standard for Information Technology — Telecommunications and Information Exchange between Systems — Local and Metropolitan Area Networks — Specific Requirements — Part 11: Wireless LAN Medium Access Control (MAC) and Physical Layer (PHY) Specifications*. IEEE 802.11ac, 2012.

[20] C. Fulton, "Digital array radar calibration and performance monitoring techniques for direct conversion and dual polarization architectures," PhD thesis, Purdue University, West Lafayette, IN, Dec. 2011.

[21] A. Mitchell, "Coupling-based wideband digital phased array calibration techniques," Master's thesis, University of Oklahoma, Norman, Oklahoma, May 2014.

[22] N. Peccarelli and C. Fulton, "A mutual coupling approach to digital predistortion and nonlinear equalization calibration for digital arrays," in *2019 IEEE International Symposium on Phased Array Systems and Technology (PAST)*, Oct. 2019.

[23] ——, "Adaptive nonlinear equalization for digital array receivers," *IEEE Trans. Microwave Theory and Technique*, vol. 67, no. 11, pp. 4493–4504, Nov. 2019.

[24] D. J. Rabideau and L. C. Howard, "Mitigation of digital array nonlinearities," in *Proc. of the 2001 IEEE Radar Conference*, May 2001.

[25] L. C. Howard and D. J. Rabideau, "Correlation of nonlinear distortion in digiatl phased arrays: Measurement and mitigation," in *2002 IEEE MTT-S International Microwave Symposium Digest*, Jun. 2002.

[26] A. V. Padaki, R. Tandon, and J. H. Reed, "On adjacent channel co-existence with receiver nonlinearity," *IEEE Trans. On Wireless Communications*, vol. 17, pp. 4922–4936, 7 Jul. 2018.

[27] R. Vansebrouck, C. Jabbour, P. Desgreys, O. Jamin, and V.-T. Nguyen, "Performance study of nonlinearities blind correction in wideband receivers," in *Proc. 21st IEEE International Conference Electronics, Circuits, and Systems (ICECS)*, Marseille, France, Dec. 2014.

[28] S. Mattisson, "Architecture and technology for multistandard transceivers," in *2001 BIPOLAR/BiCMOS Circuits and Technology Meeting*, Pctober 2001.

[29] A. Loke and F. Ali, "Direct conversion radio for digital mobile phones – design issues, status, and trends," *IEEE Trans. Microwave Theory and Techniques*, vol. 50, pp. 2422–2435, 11 Nov. 2002.

[30] M. Grimm, M. Allen, J. Marttila, M. Valkama, and R. Thoma, "Joint mitigation of nonlinear RF and baseband distortions in wideband direct-conversion

receivers," *IEEE Trans. Microwave Theory and Techniques*, vol. 62, pp. 166–182, 1 Jan. 2014.

[31] M. Allen, J. Marttila, M. Valkama, S. Singh, M. Epp, and W. Schlecker, "Digital full-band linearization of wideband direct-conversion receiver for radar and communications applications," in *2015 49th Asilomar Conference on Signals, Systems and Computers*, Nov. 2015.

[32] J. Marttila, M. Allen, M. Kosunen, K. Stadius, J. Ryynanen, and M. Valkama, "Reference receiver enhanced digital linearization of wideband direct-conversion receivers," *IEEE Trans. Microwave Theory and Techniques*, vol. 65, pp. 607–620, 2 Feb. 2017.

[33] L. Anttila, P. Handel, and M. Valkama, "Joint mitigation of power amplifier and I/Q modulator impairments in broadband direct-conversion transmitters," *IEEE Trans. Microwave Theory and Techniques*, vol. 58, pp. 730–739, 4 Apr. 2010.

[34] M. Abdelaziz, L. Anttila, and M. Valkama, "Reduced-complexity digital predistortion for massive mimo," in *2017 IEEE International Conference on Acoustics, Speech and Signal Processing (ICASSP)*, Mar. 2017.

[35] P. Jaraut, M. Rawat, and F. M. Ghannouchi, "Composite neural network digital predistortion model for joint mitigation of crosstalk, i/q imbalance, nonlinearity in mimo transmitters," *IEEE Trans. Microwave Theory and Techniques*, vol. 66, pp. 5011–5020, 11 Nov. 2018.

[36] C. Hemmi, "Pattern characteristics of harmonic intermodulation products in broadband active transmit arrays," *IEEE Trans. Antennas and Propagation*, vol. 50, pp. 858–865, 6 Aug. 2002.

[37] P. Delos, M. Jones, and M. Robertson, "RF transceivers enable forced spurious decorrelation in digital beamforming phased arrays," *Microwave Journal*, vol. 62, 4 Oct. 2018.

[38] L. C. Howard, N. K. Simon, and D. J. Rabideau, "Mitigation of correlated non-linearities in digital phased arrays using channel-dependent phase shifts," in *2003 IEEE MTT-S International Microwave Symposium Digest*, Jun. 2003.

[39] N. Peccarelli and C. Fulton, "Array-level approach to nonlinear equalziation," in *IEEE International Conference on Microwaves, Communications, Antennas and Electronics Systems, 2019. COMCAS 2019*, Nov. 2019.

[40] H. Ku, M. D. McKinley, and J. S. Kenny, "Quantifying memory effects in rf power amplifiers," *IEEE Trans. Microwave Theory and Techniques*, vol. 50, pp. 2843–2849, 12 Dec. 2002.

[41] H. Ku and J. S. Kenny, "Behavioral modeling of nonlinear rf power amplifiers considering memory effects," *IEEE Trans. Microwave Theory and Techniques*, vol. 51, pp. 2495–2504, 12 Dec. 2003.

[42] M. Yeary, G. Crain, A. Zahrai, C. D. Curtis, J. Meier, R. Kelley, I. R. Ivic, R. D. Palmer, R. J. Doviak, G. Zhang, and T.-Y. Yu, "Multichannel receiver design, instrumentation, and first results at the national weather radar testbed," *IEEE Trans. Intrumentation and Measurement*, vol. 61, pp. 2022–2033, 7 Jul. 2012.

[43] M. Yeary, R. Palmer, C. Fulton, J. Salazar, and H. Sigmarsson, "Recent advances on an s-band all-digital mobile phased array radar," in *2019 IEEE International Symposium on Phased Array Systems and Technology (PAST)*, Oct. 2019.

[44] J. Herd and S. Duffy, "Overlapped digital subarray architecture for multiple beam phased array radar," in *5th European Conference on Antennas and Propagation (EuCAP)*, Apr. 2011.

[45] C. Fulton, G. Zhang, W. Bocangel, L. Lei, R. Kelley, and M. McCord, "Cylindrical polarimetric phased array radar: A multi-function demonstrator and its calibration," in *2013 IEEE International Conference on Microwaves, Communications, Antennas and Electronic Systems (COMCAS 2013)*, Oct. 2013.

[46] W. H. Chin, Z. Fan, and R. Haines, "Emerging technologies and research challenges for 5G wireless networks," *IEEE Wireless Communications*, Apr. 2014.

[47] P. K. Agyapong, M. Iwamura, D. Staehle, W. Kiess, and A. Benjebbour, "Design considerations for a 5G network architecture," *Proc. IEEE Communications Magazine*, vol. 52, pp. 65–75, 11 Nov. 2014.

[48] M. Benisha, R. T. Prabu, and V. T. Bai, "Requirements and challenges of 5G cellular systems," in *International Conference on Advances in Electrical, Electronics, Information, Communication and Bio-Informatics (AEEICB16)*, 2016.

[49] A. V. Padaki, R. Tandon, and J. H. Reed, "Efficient spectrum access and co-existence with receiver nonlinearity: Frameworks and algorithms," *IEEE Trans. On Wireless Communications*, vol. 17, pp. 6404–6418, 10 Oct. 2018.

[50] A. Alsohaily and E. S. Sousa, "The omitted dimension: Exploiting multiuser diversity in multi-radio access technology data cellular communication systems," *IEEE Access*, vol. 4, May 2016.

[51] Y. Ye, D. Wu, Z. Shu, and Y. Qian, "Overview of LTE spectrum sharing technologies," *IEEE Access*, vol. 4, Nov. 2016.

[52] H. Shajaiah, A. Khawar, A. Abdel-Hadi, and T. C. Clancy, "Resource allocation with carrier aggregation in LTE advanced cellular system sharing spectrum with S-band radar," in *2014 IEEE International Symposium on Dynamic Spectrum Access Networks (DYSPAN)*, Apr. 2014.

[53] A. Khawar, A. Abdel-Hadi, and T. C. Clancy, "Spectrum sharing between s-band radar and LTE cellular system: A spatial approach," in *2014 IEEE International Symposium on Dynamic Spectrum Access Networks (DYSPAN)*, Apr. 2014.

[54] N. N. Krishnan, R. Kumbhkar, N. B. Mandayam, I. Seskar, and S. Kompella, "Coexistence of radar and communication systems in CBRS bands through downlink power control," in *2017 IEEE Military Communications Conference (MILCOM) - MILCOM 2017*, Oct. 2017.

[55] S. Niknam, B. Natarajan, and H. Mehrpouyan, "A spatial-spectral interference model for millimeter wave 5G applications," in *2017 IEEE 86th Vehicular Technology Conference (VTC-Fall)*, Sep. 2017.

[56] N. H. M. Adnan, I. M. Rafiqul, and A. Z. Alam, "Massive MIMO for fifth generation (5G): Opportunities and challenges," in *2016 International Conference on Computer & Communication Engineering*, 2016.

[57] D. J. Rabideau and P. Parker, "Ubiquitous mimo multifunction digital array radar," in *Thirty-Secenth Asilomar Conference on Signals, Systems & Computers*, Nov. 2003.

[58] E. Yaacoub, M. Husseini, and H. Ghaziri, "An overview of research topics and challenges for 5G massive MIMO antennas," in *2016 IEEE Middle East Conference on Antennas and Propagation (MECAP)*, Sep. 2016.

[59] P. Ferrand, M. Amara, S. Valentin, and M. Guillaud, "Trends and challenges in wireless channel modeling for evolving radio access," *Proc. IEEE Communications Magazine*, vol. 54, pp. 93–99, 7 Jul. 2016.

[60] X. Gao, L. Dai, and A. M. Sayeed, "Low RF-complexity technologies to enable millimeter-wave MIMO with large antenna array for 5G wireless communications," *IEEE Communications Magazine*, Apr. 2018.

[61] W. Roh, J.-Y. Seol, J. Park, B. Lee, J. Lee, Y. Kim, J. Cho, K. Cheun, and F. Aryanfar, "Millimeter-wave beamforming as an enabling technology for 5G cellular communications: Theoretical feasibility and prototype results," *IEEE Communications Magazine*, Feb. 2014.

[62] M. Shafi, A. F. Molisch, P. J. Smith, T. Haustein, P. Zhu, P. D. Silva, F. Tufvesson, A. Benjebbour, and G. Wunder, "5G: A tutorial overview of standards, trials, challenges, deployment, and practice," *IEEE Journal on Selected Areas in Communications*, vol. 35, pp. 1201–1221, 6 Jun. 2017.

[63] N. Bhushan, J. Li, D. Malladi, R. Gilmore, D. Brenner, A. Damnjanovic, R. T. Sukhavasi, C. Patel, and S. Geirhofer, "Network densification: The dominant theme for wireless evolution into 5G," *IEEE Communications Magazine*, vol. 52, pp. 82–89, 2 Feb. 2014.

[64] F. Boccardi, R. W. Heath Jr., A. Lozano, T. L. Marzetta, and P. Popovski, "Five disruptive technology directions for 5G," *IEEE Communications Magazine*, vol. 52, pp. 74–80, 2 Feb. 2014.

[65] C. J. Hansen, "WiGig: Multi-gigabit wireless communications in the 60 GHz band," *IEEE Wireless Communications*, vol. 18, pp. 6–7, 6 Dec. 2011.

[66] F. Al-Ogaili and R. M. Shubair, "Millimeter-wave mobile communications for 5G: Challenges and opportunities," in *IEEE International Symposium on Antennas and Propagation (APSURSI)*, Jun. 2016.

[67] B. Rapakula and G. M. Rebeiz, in *Intermodulation Effects and System Sensitivity Degradation in 5G Phased-Arrays due to Multiple Interferers*, Jun. 2018.

[68] S. Kim, Y. Jeon, G. Noh, Y. O. Park, I. Kim, and H. Shin, "A 2.59-GHz RF self-interference cancellation circuit with wide dynamic range for in-band full-duplex radio," *IEEE MTT-S International Microwave Symposium Digest*, vol. 2016-Augus, pp. 4–7, 2016, ISSN: 0149645X.

[69] B. Yang, Z. Yu, J. Lan, R. Zhang, J. Zhou, and W. Hong, "Digital beamforming-based massive MIMO transceiver for 5G millimeter-wave communications," *IEEE Transactions on Microwave Theory and Techniques*, vol. 66, 7 Jul. 2018.

[70] J. N. Murdock, E. Ben-Dor, Y. Qiao, J. I. Tamir, and T. S. Rappaport, "A 38 GHz cellular outage study for an urban outdoor campus environment," in *IEEE Wireless Communications and Networking Conference (WCNC)*, Apr. 2012.

[71] H. Zhao, R. Mayzus, S. Sun, M. Samimi, J. K. Schulz, Y. Azar, K. Wang, G. N. Wong, J. Felix Gutierrez, and T. S. Rappaport, "28 GHz millimeter wave cellular communication measurements for reflection and penetration loss in and around buildings in new york city," in *IEEE International Conference on Communications (ICC)*, Jun. 2013.

[72] T. S. Rappaport, S. Sun, R. Mayzus, H. Zhao, Y. Azar, K. Wang, G. N. Wong, J. K. Shulz, M. Sammi, and F. Gutierrez, "Millimeter wave mobile communications for 5G cellular: It will work!" *IEEE Access*, vol. 1, May 2013.

[73] S. Mondal, R. Singh, and J. Paramesh, "A reconfigurable 28/37 GHz hybrid-beamforming MIMO receiver with inter-band carrier aggregation and RF-domain LMS weigh adaptation," in *IEEE International Solid-State Circuits Conference (ISSCC)*, Feb. 2018.

[74] J. Zhang, Z. Ge, Q. Li, M. Guizani, and Y. Zhang, "5G millimeter-wave antenna array: Design and challenges," *IEEE Wireless Communications*, vol. 24, 2 Apr. 2017.

[75] R. Irazoqui and C. Fulton, "Spatial interference mitigation nulling the embedded element pattern," in *2018 IEEE/MTT-S International Microwave Symposium (IMS)*, Jun. 2018, pp. 620–623, ISBN: 9781538650677.

[76] M. Abdelaziz, L. Antilla, A. Brihuega, F. Tufvesson, and M. Valkama, "Digital predistortion for hybrid MIMO transmitters," *IEEE Journal of Selected Topics in Signal Processing*, vol. 12, pp. 445–454, 3 Jun. 2018.

[77] N. Peccarelli and C. Fulton, "Adaptive nonlinear equalization of a tunable bandpass filter," *IEEE Microwave and Wireless Components Letters*, vol. 29, no. 2, pp. 149–151, Feb. 2019.

[78] A. S. Tehrani, H. Cao, S. Afsardoost, T. Eriksson, M. Isaksson, and C. Fager, "A comparative analysis of the complexity/accuracy tradeoff in power amplifier behavioral models," *IEEE Trans. Microwave Theory and Techniques*, vol. 58, pp. 1510–1520, 6 Jun. 2010.

[79] S. Chen and B. Murmann, "An 8-bit 1.25GS/s CMOS IF-sampling ADC with background calibration for dynamic distortion," in *IEEE Asian Solid-State Circuits Conference (A-SSCC)*, Nov. 2016.

[80] Z. Dunn, M. Yeary, C. Fulton, and N. Goodman, "Wideband digital predistortion of solid-state radar amplifiers," *IEEE Transactions on Aerospace and Electronic Systems*, vol. 52, pp. 2452–2466, 5 Oct. 2016.

[81] N. Peccarelli, B. James, R. Irazoqui, J. Metcalf, C. Fulton, and M. Yeary, "Survey: Characterization and mitigation of spatial/spectral interferers and transceiver nonlinearities for 5G MIMO systems," *IEEE Trans. Microwave Theory and Technique*, vol. 67, no. 7, pp. 2829–2846, Jul. 2019.

[82] S. K. Mitra, *Digital Signal Processing: A Computer-Based Approach, 4th ed*. New York, New York: McGraw Hill, 2011.

[83] S. A. Billings, *Nonlinear System Identification NARMAX Methods in the Time, Frequency, and Spatio-Temporal Domains*. West Sussex, United Kingdom: Wiley, 2013.

[84] J. C. Pedro and S. A. Maas, "Designing multisine excitations for nonlinear model testing," *IEEE Trans. Microwave Theory and Techniques*, vol. 53, pp. 45–54, 1 Jan. 2005.

[85] A. Zhu and T. J. Brazil, "Rf power amplifier behavioral modeling using volterra expansion with laguerre functions," in *IEEE MTT-S International Microwave Symposium Digest 2005*, Jun. 2005.

[86] M. Isaksson, D. Wisell, and D. Ronnow, "A comparative analysis of behavioral models for rf power amplifiers," *IEEE Trans. Microwave Theory and Techniques*, vol. 54, pp. 348–359, 1 Jan. 2006.

[87] D. Morgan, Z. Ma, J. Kim, M. Zierdt, and J. Pastalan, "A generalized memory polynomial model for digital predistortion of RF power amplifiers," *IEEE Trans. Signal Processing*, vol. 54, no. 10, pp. 3852–3860, Oct. 2006.

[88] H. Enzinger, K. Freiberger, G. Kubin, and C. Vogel, "Baseband volterra filters with even-order terms: Theoretical foundation and practical impliactions," in *2016 50th Asilomar Conference on Signals, Systems and Computers*, Nov. 2016.

[89] S. Boyd, Y. S. Tang, and L. O. Chua, "Measuring volterra kernels," *IEEE Trans. Circuits and Systems*, vol. 30, pp. 571–577, 8 Aug. 1983.

[90] L. O. Chua and Y. Liao, "Measuring volterra kernels (ii)," *International Journal of Circuit Theory and Applications*, vol. 17, pp. 151–190, 1989.

[91] A. Zhu and T. J. Brazil, "Behavioral modeling of rf power amplifiers based on pruned volterra series," *IEEE Microwave and Wireless Components Letters*, vol. 14, no. 12, pp. 563–565, Dec. 2004.

[92] A. Zhu, M. Wren, and T. J. Brazil, "An efficient volterra-based behavioral model for wideband rf power amplifiers," in *IEEE MTT-S International Microwave Symposium Digest 2003*, Jun. 2003.

[93] A. Zhu, J. C. Pedro, and T. J. Brazil, "Dynamic deviation reduction-based volterra bahavioral modeling of rf power amplifiers," *IEEE Trans. Microwave Theory and Techniques*, vol. 54, pp. 4323–4332, 12 Dec. 2006.

[94] A. Carini, E. Mumolo, and G. L. Sicuranza, "V-vector algebra and its application to volterra-adaptive filtering," *IEEE Transactions on Circuits and Systems – II: Analog and Digital Signal Processing*, vol. 46, no. 5, pp. 585–598, May 1999.

[95] O. Hammi, "Orthogonal polynomial based hammerstein behavioral model for power amplifiers with strong memory effects," in *2010 Asia-Pacific Microwave Conference*, Dec. 2010.

[96] N. J. Bershad, P. Celka, and S. McLaughlin, "Analysis of stochastic gradient identification of wiener-hammerstein systems for nonlinearities with hermite polynomial expansions," *IEEE Trans. on Signal Processing*, vol. 49, pp. 1060–1072, 5 May 2001.

[97] M. Schoukens, G. Vandersteen, and Y. Rolain, "An identification algorithm for parallel wiener-hammerstein systems," in *52nd IEEE Conference on Decision and Control*, Dec. 2013.

[98] L. Ding, G. T. Zhou, D. R. Morgan, Z. Ma, J. S. Kenny, J. Kim, and C. R. Giardina, "A robust digital baseband predistorter constructed using memory polynomials," *IEEE Trans. on Communications*, vol. 52, pp. 159–165, 1 Jan. 2004.

[99] M. Schoukens, R. Pintelon, and Y. Rolain, "Parametric identification of parallel hammerstein systems," *IEEE Transactions on Instrumentation and Measurement*, vol. 60, pp. 3931–3938, 12 Dec. 2011.

[100] F. M. Ghannouchi and O. Hammi, "Behavioral modeling and predistortion," *IEEE Microwave Magazine*, vol. 10, 7 Dec. 2009.

[101] G. L. Cunha, S. Farsi, B. Nauwelaers, and D. Schreurs, "An FPGA-based digital predistorter for RF power amplifier linearization using cross-memory polynomial model," *International Workshop on Integrated Nonlinear Microwave and Millimeter-wave Circuits (INMMiC)*, pp. 1–3, 2014.

[102] M. Isaksson, D. Wisell, and D. Ronnow, "Wide-band dynamic modeling of power amplifiers using radial-basis function neural networks," *IEEE Trans. Microwave Theory and Techniques*, vol. 53, pp. 3422–3428, 11 Nov. 2005.

[103] J. Pedro and N. B. Carvalho, *Intermodulation Distortion in Microwave and Wireless Circuits*. Norwood, MA: Artech House, 2003.

[104] N. Peccarelli, Z. Peck, and J. Garry, "Analysis and mitigation of receiver induced nonlinearities on pulse-doppler radars," in *IEEE International Radar Conference 2020*, Apr. 2020.

[105] H. C. de Graaff and J. te Winkel, "Relationship between crossmodulation and intermodulation," *Electronics Letters*, vol. 8, pp. 33–34, 2 Jan. 1972.

[106] G. F. Earl, "The influence of receiver cross-modulation on attainable hf radar dynamic range," *IEEE Transactions on Instrumentation and Measurement*, vol. 36, pp. 776–782, 3 Sep. 1987.

[107] ——, "Receiving system linearity requirements for hf radar," *IEEE Transactions on Instrumentation and Measurement*, vol. 40, pp. 1038–1041, 6 Dec. 1991.

[108] R. G. Meyer and A. K. Wong, "Blocking and desensitization in rf amplifiers," *IEEE Journal of Solid-State Circuits*, vol. 30, pp. 944–946, 8 Aug. 1995.

[109] K. M. Harrington, "Active array radar nonlinearity requirements – spectral analysis of third order intermodulation clutter," in *Proc. of International Symposium on Phased Array Systems and Technology*, Oct. 1996.

[110] J. F. Sevic, K. L. Burger, and M. B. Steer, in *A Novel Envelope-Termination Load-Pull Method for ACPR Optimization of RF/Microwave Power Amplifiers*, Jun. 1998.

[111] D. Saffar, N. Boulejfen, F. Ghannouchi, M. M. Helaoui, and A. Gharssalah, "Compensation of I/Q impairments and nonlinear distortion in mimo wireless transmitters," in *2013 IEEE 11th International New Circuits and Systems Conference (NEWCAS)*, Sep. 2013.

[112] R. N. Braithwaite, "Digital predistortion of an RF power amplifier using a reduced volterra series model with a memory polynomial estimator," *IEEE Trans. Microwave Theory and Techniques*, vol. 65, pp. 3613–3623, 10 Oct. 2017.

[113] M. Abdelaziz, L. Anttila, A. Kiayani, and M. Valkama, "Decorrelation-based concurrent digital predistortion with a single feedback path," *IEEE Trans. Microwave Theory and Techniques*, vol. 66, pp. 280–293, 1 Jan. 2018.

[114] M. B. Yeary, "An efficient intermodulation product computing technique for broadband active transmit systems," *IEEE Trans. Intrumentation and Measurement*, vol. 57, pp. 438–443, 2 Feb. 2008.

[115] C. Fager, K. Hausmair, K. Buisman, K. Andersson, E. Sienkiewicz, and D. Gustafsson, "Analysis of nonlinear distortion in phased array transmitters," in *2017 Integrated Nonlinear Microwave and Millimetre-wave Cirsuits Workshop (INMMiC)*, Apr. 2017.

[116] Z. Dunn, M. Yeary, C. Fulton, and R. Rincon, "Impedance-dependent wideband digital predistortion of solid-state radar amplifiers," *IEEE Transactions on Aerospace and Electronic Systems*, vol. 53, pp. 2290–2303, 5 Oct. 2017.

[117] G. Montoro, P. L. Gilabert, E. Bertran, A. Cesari, and J. A. Garcia, "An LMS-based adaptive predistorter for cancelling nonlinear memory effects in RF power amplifiers," in *2007 Asia-Pacific Microwave Conference*, Dec. 2007.

[118] Y. H. Lim, Y. S. Cho, I. W. Cha, and D. H. Youn, "An adaptive nonlinear prefilter for compensation of distortion in nonlinear systems," *IEEE Trans. on Signal Processing*, vol. 46, 6 Jun. 1998.

[119] A. D. Poularikas, *Adaptive Filtering*. Boca Raton, Forida: CRC Press, 2015.

[120] A. E. Abdelrahman, O. Hammi, A. K. Kwan, A. Zerguine, and F. M. Ghannouchi, "A novel weighted memory polynomial for behavioral modeling and digital predistortion of nonlinear wireless transmitters," *IEEE Trans. on Industrial Electronics*, vol. 63, pp. 1745–1753, 3 Oct. 2015.

[121] V. N. Manyam, D.-K. G. Pham, C. Jabbour, and P. Desgreys, "An FIR memory polynomial predistorter for wideband RF power amplifiers," in *2017 15th IEEE International New Circuits and Systems Conference (NEWCAS)*, Jun. 2017.

[122] Z. A. Khan, E. Zenteno, P. Handel, and M. Isaksson, "Digital predistortion for joint mitigation of I/Q imbalance and MIMO power amplifier distortion," *IEEE Trans. Microwave Theory and Techniques*, vol. 65, pp. 322–333, 1 Jan. 2017.

[123] S. Lee, M. Kim, Y. Sirl, E.-R. Jeong, S. Hong, S. Kim, and Y. H. Lee, "Digital predistortion for power amplifiers in hybrid MIMO systems with antenna subarrays," in *2015 IEEE 81st Vehicular Technology Conference (VTC-Spring)*, May 2015.

[124] L. Liu, W. Chen, L. Ma, and H. Sun, "Single-PA-feedback digital predistortion for beamforming MIMO transmitter," in *2016 IEEE International Conference on Microwave and Millimeter Wave Technology (ICMMT)*, Jun. 2016.

[125] H. Yan and D. Cabric, "Digital predistortion for hybrid precoding architecture in millimeter-wave massive mimo systems," in *2017 IEEE International Conference on Acoustics, Speech and Signal Processing (ICASSP)*, Mar. 2017.

[126] X. Liu, Q. Zhang, W. Chen, H. Feng, L. Chen, F. M. Ghannouchi, and Z. Feng, "Beam-oriented digital predistortion for 5G massive MIMO hybrid beamforming transmitters," *IEEE Trans. Microwave Theory and Techniques*, vol. 66, pp. 3419–3432, 7 Jul. 2018.

[127] N. Tervo, M. E. Leinonen, J. Aikio, T. Rahkonen, and A. Parssinen, "Analyzing the effects of pa variations on the performance of phased array digital predistortion," in *2018 IEEE 29th Annual International Symposium on Personal, Indoor and Mobile Radio Communications (PIMRC)*, Sep. 2018.

[128] *Analog devices lays foundation for 4g to 5g migration with expanded radioverse^{TM} wireless technology and design ecosystem*, Analog Devices, Jun. 2017.

[129] M. Grimm, R. K. Sharma, M. Hein, R. S. Thoma, and R. Zemmari, "Improved BER performance in GSM by mitigating non-linear distortions in the receiver," in *Proc. European Microwave Conference*, Nuremberg, Germany, Oct. 2013.

[130] R. Gharpurey, "Linearity enhancement techniques in radio receiver front-ends," *IEEE Trans. Circuits and Systems*, vol. 59, pp. 1667–1679, 8 Aug. 2012.

[131] E. Rebeiz and D. Cabric, "How wideband receiver nonlinearities impact spectrum sensing," in *Proc. IEEE Global Conference on Signal and Information Processing (GlobalSIP)*, Dec. 2013.

[132] P. Xue, H. Yang, Z. Xu, C. Zhou, and S. Zhou, "Effect of nonlinearities in wireless communication with digital receiver," in *2013 IEEE Wireless Communications and Networking Conference (WCNC)*, Apr. 2013.

[133] Y. Li, J. M. Rabaey, and A. Sangiovanni-Vincentelli, "Analysis of interference effects in MB-OFDM UWB systems," in *Proc. IEEE Wireless Communications and Networking Conference (WCNC)*, Apr. 2008.

[134] *Standard for Information technology — Telecommunications and information Exchange between Systems — Local and metropolitan area networks — Specific requirements - Part 15.3: Wireless Medium Access Control (MAC) and Physical Layer (PHY) Specifications for High Rate Wireless Personal Area Networks (WPANs)*. IEEE 802.16m, 2003.

[135] A. Taparugssanagorn, K. Umebayashi, J. Lehtomaki, and C. Pomalaza-Raez, "Analysis of the effect of nonlinear low noise amplifier with memory

for wideband spectrum sensing," in *1st International Conference on 5G for Ubiquitous Connectivity*, Nov. 2014.

[136] D. Dupleich, M. Grimm, F. Schlembach, and R. S. Thoma, "Practical aspects of a digital feedforward approach for mitigating non-linear distortions in receivers," in *Proc. 11th International Telecommunications in Modern Satellite, Cable and Broadcast Services Conference (TELSIKS)*, Nis, Serbia, Oct. 2013.

[137] R. Gangarajaiah, M. Abdulaziz, H. Sjoland, P. Nilsson, and L. Liu, "A digitally assisted nonlinearity mitigation system for tunable channel select filters," *IEEE Trans. Circuits Systems II, Express Briefs*, vol. 63, 1 Jan. 2016.

[138] H. Chen and R. Gentile, "Phased array system simulation," in *2016 IEEE International Symposium on Phased Array Systems and Technology (PAST)*, Oct. 2016.

[139] B. James and C. Fulton, "Nonlinear array system modeler for advanced array calibration," in *Proc. GOMACTech 2017*, Mar. 2017.

[140] A. Balankutty and P. R. Kinget, "An ultra-low voltage, low-noise, high linearity 900-MHz receiver with digitally calibrated in-band feed-forward interferer cancellation in 65-nm CMOS," *IEEE Journal of Solid-State Circuits*, vol. 46, pp. 2268–2283, 10 Oct. 2011.

[141] P. Delos, "System-level lo phase noise model for phased arrays with distributed phase-locked loops," *Analog Devices Technical Article*, 2019.

[142] M. A. Richards, "Fundamentals of radar signal processing," in. New York, New York: McGraw-Hill, 2014.

[143] V. Gregers-Hansen and M. T. Ngo, "Radar dynamic range specification and measurement," in *Proc. 2009 International Radar Conference*, Oct. 2009.

[144] N. Peccarelli, B. James, C. Fulton, and N. Goodman, "Dynamic range considerations for modern digital array radars," in *IEEE International Radar Conference 2020*, Apr. 2020.

[145] J. C. Pedro and N. B. Carvalho, "Inferring nonlinear distortion performance of power amplifiers subject to telecommunications signals from two-tone measurements," in *IEEE MTT-S International Microwave Symposium Digest*, Jun. 2005.

[146] H. Ku and J. Kenny, "Estimation of error vector magnitude using two-tone intermodulation distortion measurements," in *2001 IEEE MTT-S Digest*, Jun. 2001.

[147] L. Aladren, P. Garcia-Ducar, J. de Mingo, P. L. Carro, and C. Sanches-Perez, "Digital predistortion using non-stationary windowed sequences for LTE power amplifier linearization," in *2012 IEEE/MTT-S International Microwave Symposium Digest*, Jun. 2012.

[148] L. Aladren, P. Garcia-Ducar, J. de Mingo, C. Sanches-Perez, and P. L. Carro, "Behavioral power amplifier modeling and digital predistorter design with a chirp excitation signal," in *2011 IEEE 73rd Vehicular Technology Conference (VTC Spring)*, May 2011.

[149] P. Burrascano, S. Laurenti, L. Senni, G. Silipigni, R. Tomasello, and M. Ricci, "Chirp design in a pulse compression procedure for the identification of non-linear systems," in *2017 14th International Conference on Synthesis, Modeling, Analysis and Simulation Methods and Applications to Circuits Design (SMACD)*, Jun. 2017.

[150] M. I. Skolnik, *Radar Handbook*, Third. New York, New York: McGraw-Hill, 2008.

[151] S. Mano and T. Katagi, "A method for measuring amplitude and phase of each radiating element of phased array antenna," *Transactions IECE*, vol. J65-B, pp. 555–560, 5 May 1982.

[152] J. K. Mulcahey and M. G. Sarcione, "Calibration and diagnostics of the thaad solid state phased array in a planar nearfield facility," in *IEEE International Symposium on Phased Array Systems and Technology*, Oct. 1996.

[153] D. Bekers, R. van Dijk, and F. van Vliet, "Mutual-coupling based phased-array calibration: A robust and versatile approach," in *2013 IEEE International Symposium on Phased Array Systems and Technology*, Oct. 2013.

[154] C. M. Schmid, C. Pfeffer, R. Feger, and A. Stelzer, "An fmcw mimo radar calibration and mutual coupling compensation approach," in *10th European Radar Conference*, Oct. 2013.

[155] M. Sarcione, J. Mulcahey, D. Schmidt, K. Chang, M. Russell, R. Enzmann, W. Guzak, R. Howard, and M. Mitchell, "The design, development and testing of the thaad (theater high altitude area defense) solid state phased

array (formerly ground based radar)," in *IEEE International Symposium on Phased Array Systems and Technology*, Oct. 1996.

[156] O. Inac, S. Kim, D. Shin, C. Kim, and G. Rebeiz, "Built-in self test systems for silicon-based phased arrays," in *2012 IEEE/MTT-S International Microwave Symposium Digest*, Jun. 2012.